University of South Florida

Digital Commons @ University of South Florida

USF Tampa Graduate Theses and Dissertations   USF Graduate Theses and Dissertations

2006

Spatially resolved photoluminescence spectroscopy of quantum dots

Maciej Dybiec
University of South Florida

Follow this and additional works at: https://digitalcommons.usf.edu/etd

Part of the American Studies Commons

Spatially Resolved Photoluminescence Spectroscopy of Quantum Dots

by

Maciej Dybiec

A dissertation submitted in partial fulfillment
of the requirements for the degree of
Doctor of Philosophy
Department of Electrical Engineering
College of Engineering
University of South Florida

Co-Major Professor: Sergei Ostapenko, Ph.D.
Co-Major Professor: Stephen Saddow, Ph.D.
Andrew Hoff, Ph.D.
Chris Ferekides, Ph.D.
Sarath Witanachi, Ph.D.
Tatyana Zhukov, Ph.D.

Date of Approval:
October 20, 2006

Dedication

To my wife Aleksandra, without her all this would not be possible.

Acknowledgments

I would like to thank my major professor Dr. Sergei Ostapenko for his help, guidance and patience during my research work that led to this PhD, and for all other support that I have received. I would also like to thank Dr. Stephen Saddow, who was of great help and shared his expertise with me while motivating me to work harder and obtain better study results-for this I am very grateful.

I wanted to thank the many others who have lent their support during my course work period, especially Dr. Tatyana Zhukov. Without her experience and support the biology portion of these experiments would not have been as successful.

Many fruitful discussions with Dr. Tatyana Torchynskaya and Professor Nadia Korsunkaya contributed a great deal to this work and I want to thank them in this letter as well.

And last but certainly not least, I would like to thank Igor Tarasov. He had the patience to work and aid me in many aspects of photoluminescence segment of this work.

Table of Contents

List of Tables

List of Figures

Spatially Resolved Photoluminescence Spectroscopy of Quantum Dots

Maciej Dybiec

ABSTRACT

Recent advancements in nanotechnology create a need for a better understanding of the underlying physical processes that lead to the different behavior of nanoscale structures in comparison to bulk materials. The influence of the surrounding environment on the physical and optical properties of nanoscale objects embedded inside them is of particular interest. This research is focused on the optical properties of semiconductor quantum dots which are zero-dimensional nanostructures. There are many investigation techniques for measuring the local parameters and structural characteristics of Quantum Dot structures. They include X-ray diffraction, Transmission Electron Microscopy, Wavelength Dispersive Spectroscopy, etc. However, none of these is suitable for the study of large areas of quantum dots matrices and substrates.

The existence of spatial inhomogeneity in the quantum dots allows for a deeper and better understanding of underlying physical processes responsible in particular for the observed changes in photoluminescence (PL) characteristics. Spectroscopic PL mapping can reveal areas of improved laser performance of InAs – InGaAs quantum dots

structures. Establishing physical mechanisms responsible for two different types of spatial PL inhomogeneity in InAs/InGaAs quantum dots structures for laser applications was the first objective of this research.

Most of the bio-applications of semiconductor quantum dots utilize their superior optical properties over organic fluorophores. Therefore, optimization of QD labeling performance with biomolecule attachment was another focus of this research. Semiconductor quantum dots suspended in liquids were investigated, especially the influence of surrounding molecules that may be attached or bio-conjugated to the quantum dots for specific use in biological reactions on the photoluminescence spectrum. Provision of underlying physical mechanisms of optical property instability of CdSe/ZnS quantum dots used for biological applications was in the scope of this research. Bio-conjugation and functionalization are the fundamental issues for bio-marker tagging application of semiconductor quantum dots. It was discovered that spatially resolved photoluminescence spectroscopy and PL photo-degradation kinetics can confirm the bio-conjugation. Development of a methodology that will allow the spectroscopic confirmation of bio-conjugation of quantum dot fluorescent tags and optimization of their performance was the final goal for this research project.

1. Introduction

> "The principles of physics, as far as I can see, do not speak against the possibility of maneuvering things atom by atom."
>
> Richard Feynman, 1959 [1]

1.1. Scope and motivation

Nanotechnology since its beginnings connected many areas of research. Nowadays its an already establish field of science that interconnects mechanics, electronics, optics and other fields of science with one thing in common - the nanometer sizes of final structures [1, 2]. Today we are able to control material processes that allow us to create particles and structures on the nanometer scale, even allowing the manipulation of single atoms. In nanotechnology not only size matters but the shape, chemical and bio surface properties and physical properties of these small structures determine their use and applications. Since nanoparticles have large volume to surface area ratio most of their properties are determined by the physical and chemical reactions that take place at the surface. The possibility of using these surface properties and a virtually inexhaustible way to modify it has drawn the attention of scientists and

1

engineers. Study of the physical chemistry of materials of a size in between the bulk and isolated molecules is a major trend nowadays even though the discovery of semiconductor nanocrystallites was made in 1932 [3]. The focus is on nanometer size fragments of semiconducting inorganic solids which contain from a handful to thousands of atoms. Fragments of matter of these sizes are often large enough to exhibit a crystalline core but too small to have developed solid state electronic and vibrational band structure. One may say that for matter on this scale they are neither bulk nor molecular in structure. In this range of sizes properties of solid state bulk begin to form from the molecular level but the clear band structure has yet to form. In addition to being interesting from a fundamental science viewpoint, materials in this size range may have a number of technological applications. For example, semiconductor nanocrystallites may have large optical nonlinearities which could be useful in optical devices. Organized arrays of little crystallites may have mechanical, optical, electrical, and thermal properties quite different from the bulk. In this work Quantum Dot (QD) matrices were investigated that are used for laser applications and the spatial inhomogeneity of their optical parameters was studied. In the majority of cases the observed spatial non-uniformity is contributed to non uniform size distribution of the QD's, but there are other factors that come into play apart from this, such as the capping layer inhomogeneity, different electron hole wave function overlapping for different QD shapes, different shape/strain conditions in real samples, just to list few examples. A deeper photoluminescence study of such structures is still needed and is a major part of this research.

Quantum Dot lasers are of particular interest for their advantages over the quantum well laser such as: narrower gain spectra, lower threshold currents and weaker

temperature dependence. All of these spring from the very narrow δ-function-like density of states for the carriers confined in the QD's [4]. Strong quantum confinement in all three dimensions creates discrete carrier energy spectra. Transitions between the electron and hole levels in the QD are analogous to those between the discrete levels of individual atoms. For this reason, QD's have generated much interest as a new class of artificially structured materials with tunable (through varying composition and sizes) energies of discrete atomic-like states that are ideal for use in laser [5, 6].

One of the most common applications of QD's apart from lasers is in fluorescence tagging, where they are being developed to replace molecular dyes. These range from biological to environmental applications. In these applications when the tagging substance is irradiated with light it absorbs the light and then re-emits at a different wavelength. The presence of the tagging substance can then be easily identified by detection of the characteristic emission spectrum. For example, injecting a tagging substance into a particular biological cell makes it possible to identify that cell amid other cells from its fluorescence signature.

There are several reasons why QD's have advantages over organic fluorophores [2, 7, 8]. The first of these is that QD's can absorb a wide band of light for their excitation, but they emit in a very narrow band. In contrast, most molecular dyes can absorb only a very narrow band of wavelength, so most of the illuminating light is not used. This is illustrated in Figure 1.1.
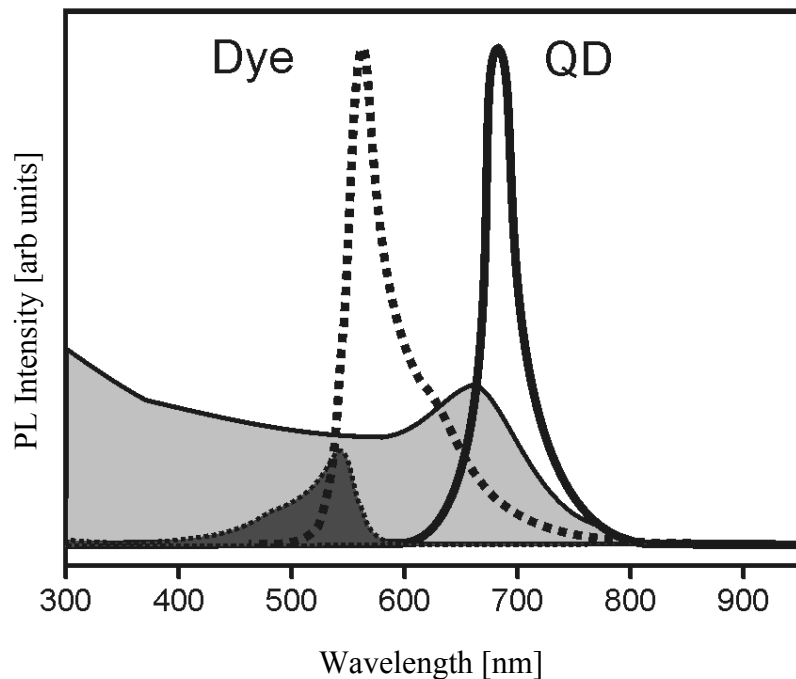
Figure 1.1   Comparison of the emission and absorption spectra of QD (continuous line) and organic dye (dotted line) (curves with the shaded area are the absorption spectra)

Also, these molecules emit in a much wider band of wavelengths compared to QD's. As a result, to distinguish separate features one needs to use very different molecular dyes, each with its own required excitation wavelengths. In the case of QD's the emission wavelength depends on the size. So, QD's made of the same semiconductor material, but of different sizes, can all be excited by the same light source (provided above band-gap energy is used), but then they emit distinctly different wavelengths.

Emission is very efficient in Quantum Dots and doesn't decrease so rapidly with time under UV illumination as in organic tags [9]. Quantum dots have large molar extinction coefficient value[10], typically on the order of 0.5-5 x 10^{-6} $M^{-1}cm^{-1}$ [11] which

means that quantum dots are capable of absorbing excitation photons very efficiently; the absorption rate of QD's is approximately 10-50 times faster than organic dyes [12]. The higher rate of absorption is directly correlated to the quantum dot brightness and it has been found that QD's are 10-20 times brighter than organic dyes [9, 10, 13], allowing highly sensitive fluorescence imaging.

Their photo stability over long periods of time is one of the key factors that put them as the best fluorophores so far. In comparison to organic dyes that bleach after a couple of minutes under a standard confocal microscope, QD's can last for several hours under same illumination conditions [14].

Another feature of QD's that makes them a good candidate for tagging purposes is that their tagging property is controllable. With proper chemistry these objects can be attached to specific biomolecules that perform specific tasks, such as anti-gene and anti-body recognition, for example. This is in contrast to traditionally used molecular tags that have well defined binding characteristics. As a result a particular fluorophore tag may or may not bind with a given molecule or surface of interest. QD's have a surface that can bind with a variety of molecules, they can be prepared (functionalized) so as to attach to well defined targets.

A fourth feature of QD's that makes them desirable for tagging is their nonlinear optical behavior. Through frequency-doubling nonlinear optical materials can absorb two photons of a longer wavelength and create a single photon of shorter wavelength. But most optical materials have a small non-linearity. QD's are made with large nonlinear properties that have allowed researchers to employ them for deep noninvasive imaging. Although the quantum efficiency is many times lower than without frequency up

conversion, it is still possible to detect QD's due their high extinction coefficients. One example of this principle is that this "fluorescence" allows the imaging of the blood vessels/tumors without opening the tissue [15].

Though these features make QD's a better choice over organic fluorophores there is not much known about the interaction of quantum dots with surrounding molecules in terms of photoluminescence properties. Bio-conjugation is nothing other than attaching proteins to the surface of a quantum dot either covalently, electrostatically, or with the use of a linker molecule, (through ionic interaction for example). In fact all these interactions come down to electrostatic forces at some level. This has an effect on the interaction of a particular quantum dot with the electromagnetic radiation, either with absorption or emission and some signs of that are suspected to appear in photoluminescence spectra.

1.2.   QD photoluminescence

Photoluminescence is a process in which a chemical compound absorbs a photon with a wavelength in the range of visible or UV electromagnetic radiation, thus transitioning to a higher electronic energy state, and then radiates a photon back out, returning to a lower energy state. The period between absorption and emission is typically extremely short, on the order of 10 nanoseconds. Under special circumstances, however, this period can be extended into minutes or hours [16].

Ultimately, available chemical energy states and allowed transitions between states (and therefore wavelengths of light preferentially absorbed and emitted) are

determined by the rules of quantum mechanics. A basic understanding of the principles involved can be gained by studying the electron configurations and molecular orbitals of simple atoms and molecules. More complicated molecules and advanced subtleties are treated in the field of computational chemistry.

The simplest photoluminescent processes are resonant radiations, in which a photon of a particular wavelength is absorbed and an equivalent photon is immediately emitted. This process involves no significant internal energy transitions of the chemical substrate between absorption and emission and is extremely fast, on the order of 10 nanoseconds.

More interesting processes occur when the chemical substrate undergoes internal energy transitions before re-emitting the energy from the absorption event. The most familiar such effect is fluorescence, which is also typically a fast process, but in which some of the original energy is dissipated so that the emitted light is of lower energy than that absorbed.
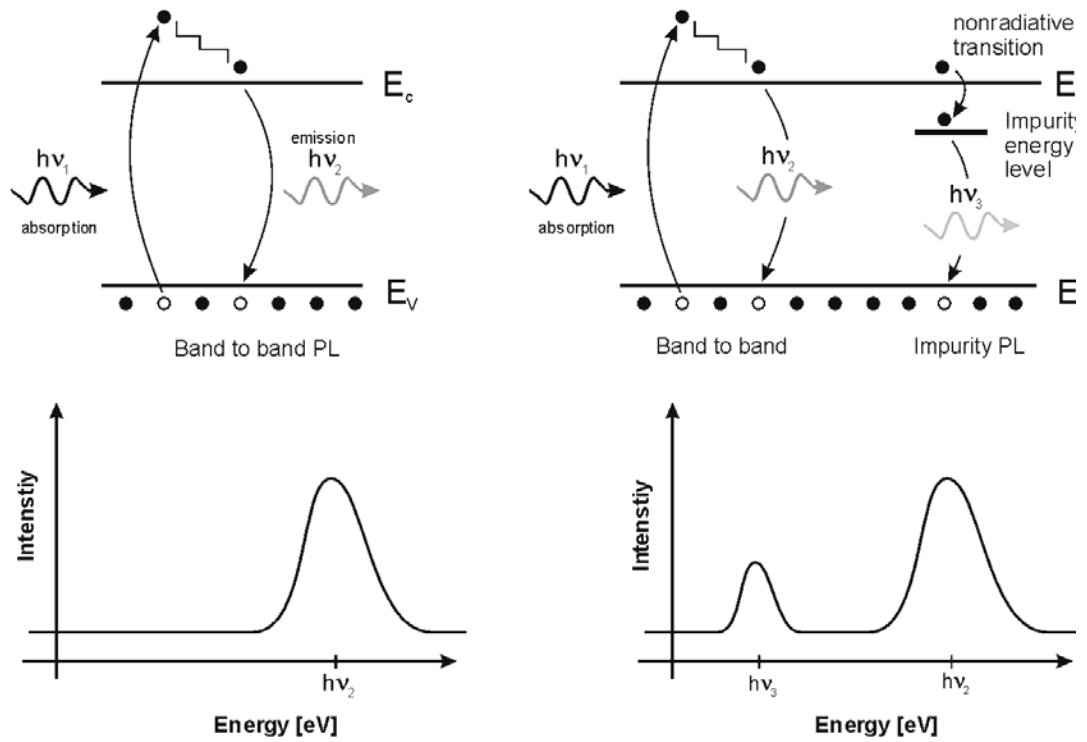
$$h\nu_1 > h\nu_2 > h\nu_3$$

Figure 1.2   Schematic representation of the basic photoluminescence mechanisms for bulk materials

Photoluminescence in QD is governed by the same mechanisms as in the bulk material, major difference is that all the energy levels inside the quantum dots are strongly quantized due to small dimensions of QD. Direct consequences of this quantization are very sharp emission spectral lines (δ function – like for a single QD), that are in general broadened only by the QD size distribution.

1.3.   Research plan

This research is divided into two major parts. In the first part InAs self assembled QD's embedded in InGaAs matrices are being investigated. Spatial photoluminescence (PL) scanning of the 5x10 mm samples is performed followed with the full 50mm in diameter wafers investigations of the same structures. All samples contain InAs quantum dots stacked in "sandwich" like structures placed in between capping and wetting layers respectively, apart from the spatial distribution of PL intensity, In composition of capping layers is investigated as well as the influence of the growth temperature for the In islands creation phase.

The second part is focused on the photoluminescence investigations of CdSe/ZnS core/shell quantum dots dispersed in liquids and conjugated to different biomolecules for biomedical applications. The influence of bioconjugation on the PL features of these QD is of major interest. Four major sizes of quantum dots were studied with the major peak emissions around: 525, 605, 655 and 705 nm. For the conjugation experiments four different biomolecules were chosen with further aim to be applied in early cancer detection. These were: interleukin 10 (IL10), cancer antigen 125 (CA125), prostate specific antigen (PSA) and Osteopontin. All of these biomolecules are being widely used as ovarian cancer biomarkers. Initial experiments were done to show PL intensity dependence vs. pure QD concentration; these were followed with wet enzyme-linked immunosorbent assays (ELISA) measurements of conjugated QD and finally with PL measurements of dried QD-conjugate spots printed with the micro array technique. Time dependent and maxima spectral position studies were performed in order to detect

bioconjugation. The sample preparation was done in two ways, the initial samples for wet ELISA experiments involved QD's preconjugated by the supplier (Invitrogen) [11], while in the micro array part the conjugation was done at Moffitt Cancer Center at the University of South Florida.

1.4. Summary

Photoluminescent features of quantum dots in III-V (InAs) and II-VI (CdSe) element groups are the main focus of this research. The spatial PL intensity distribution with connection to quantum dot parameters, capping layer composition and growth temperature influence for 50mm wafers is studied. InAs QD are of great importance for optoelectronic applications in the infrared (1.3 μm) part of the electromagnetic spectrum.

Unique optical properties of quantum dots structures in colloidal solutions make them suitable for medical applications as fluorescent markers. CdSe/ZnS QDs have been studied for photoluminescent signatures of possible biomolecules attachment (bioconjugation). The practical implications of any PL feature that is not relaying on the averaged intensity as a measure of bioconjugation would be of great importance for bio applications. Increased sensitivity of any nowadays applicable cancer tests is very desirable and motivation for this type research is clear. In the short term the ability to detect bioconjugation with some characteristic spectral features would prove another advantage of QD's over organic fluorophores and save time and money before any further bio experiments would have to be done.

The objectives of the research were:

- Establish mechanisms responsible for spatial photoluminescence inhomogeneity of InAs/InGaAs quantum dot structures for laser applications.

- Establish mechanisms of optical properties instability of CdSe/ZnS quantum dots used for biological applications.

- Develop a methodology that will allow spectroscopic confirmation of the bio-conjugation of quantum dots fluorescent tags to bio-molecules and optimize their performance in different working environments including substrates and solutions.

2. Electronic Structure of Quantum Confined Systems

2.1. Introduction

Semiconductor quantum dots have emerged as one of the first applications of nanotechnology [17-19]. Quantum dot applications have been primarily in nonlinear optics and in the Q-switching of lasers [4-6, 20, 21]. Though, the quantum dot laser has yet to enter the mainstream, it is recognized as a key application of QD's materials. Their specific optical properties made them very good fluorescence particles used for tagging in the biomedical field which so far is the second most popular application. Among possible applications being discussed is quantum computing, [22] which is a very promising field and their use in photovoltaic's technology [23] is another one. However, the full impact of quantum dot technology is still to come.

Discovery of the yellow or red color made in the early 1930's [3] of some silicate glasses was attributed to nanometer size crystal inclusions of CdSe and CdS, but it took almost fifty years to link colored glasses to the energy states determined by the quantum confinement in embedded CdS or CdSe nanoparticles [24]. The idea to use quantum confinement in thin layers of materials was discussed since the early 1960's and the theory of electron motion in a crystal with superimposed periodic potential's was developed at that time [25]. The first quantum structures to appear were quantum wells

(QWs) that were formed as a sandwich of very thin 5-7 nm [26] thin layers of narrow band gap semiconductors located between wider band gap semiconductor material. Quantum wires and quantum dots (QDs) are, respectively, low dimensional structures that follow this trend of development – from one dimensional (QW) down to "zero dimensional" (QD) structures.

2.2.   Electronic structure of quantum dots as zero dimensional systems

The band structure of a bulk semiconductor material is a result of the superposition of the wave functions and energy states of all the atoms that constitute the crystal. In the case of a quantum dot the 3D structure is comprised only of a couple of hundred to a couple of thousand atoms; their specific properties are due to the fact that the size of the QD is smaller or comparable to the bulk Bohr exciton radius. The very strong quantum confinement effects come into play to form the band structure of a single QD with very discrete energy states. QD's confine carriers (electron – hole pairs) in all three dimensions, accordingly they are called "zero dimensional structures" while they are effectively 3D structures. The band structure of a single quantum dot has very distinct allowed energy levels, and due to this property, quantum dots are sometimes called artificial atoms since they are very similar to atomic states. Figure 2.1 shows the density of electron states function vs. energy for all possible quantum confinement arrangements.
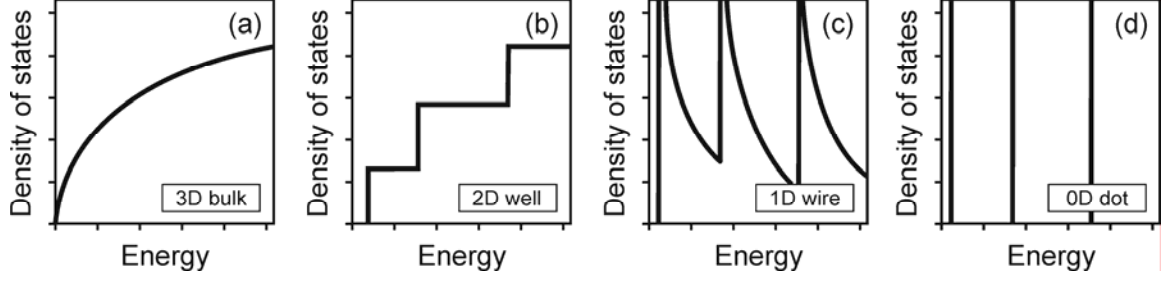
Figure 2.1 Densities of states versus energy for bulk, 2D, 1D and 0 dimensional

structures

The density of states for the three-dimensional system (bulk semiconductor) has the form:

$$\frac{dN}{dE} \propto \frac{d}{dE} E^{3/2} = E^{1/2} \tag{1}$$

for a two-dimensional system (quantum well) is a step function,

$$\frac{dN}{dE} \propto \frac{d}{dE} \sum_{\varepsilon_i < E} (E - \varepsilon_i) = \sum_{\varepsilon_i < E} 1 \tag{2}$$

for a one-dimensional system (quantum wire) has a peculiarity,

$$\frac{dN}{dE} \propto \frac{d}{dE} \sum_{\varepsilon_i < E} (E - \varepsilon_i)^{1/2} = \sum_{\varepsilon_i < E} (E - \varepsilon_i)^{-1/2} \tag{3}$$

and for a zero-dimensional system (quantum dot) has the shape of δ-peaks

$$\frac{dN}{dE} \propto \frac{d}{dE} \sum_{\varepsilon_i < E} \Theta(E - \varepsilon_i) = \sum_{\varepsilon_i} \delta(E - \varepsilon_i) \tag{4}$$

Above, ε_i are i-[th] discrete energy levels inside well, wire and QD respectively, Θ is a

Heaviside step function, and δ is the Dirac-delta function.

When considering the energy spectrum of a zero-dimensional system, we have to study the time-independent Schrödinger equation (5) with the confining potential, which is a function of all three spatial coordinates and confines the electron in all three directions:

$$\left[-\frac{\hbar^2\nabla^2}{2m}+V(x,y,z)\right]\psi(x,y,z)=E\psi(x,y,z) \tag{5}$$

Where ħ is Planck's constant divided by 2π, ∇ is the Laplacian operator, m is mass of the particle, V(x,y,z) is the potential and ψ(x,y,z) is the wavefunction. The simplest potential V(x, y, z) of this type is:

$$V(x,y,z)=\begin{cases} 0 & inside \quad the \quad box \\ +\infty & outside \quad the \quad box \end{cases}$$
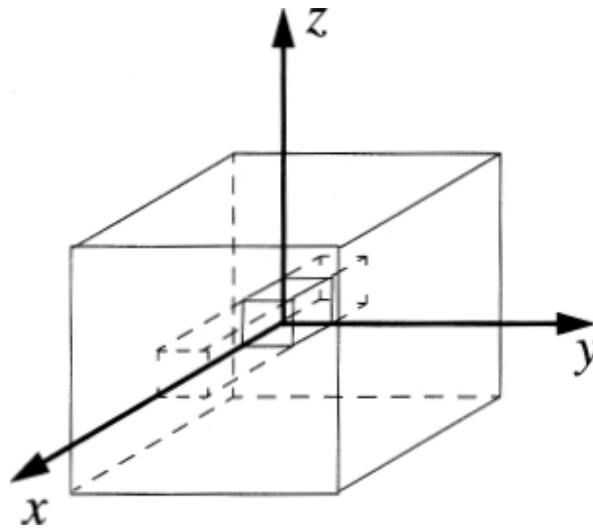
Figure 2.2 Sketch of a quantum box embedded in a matrix

Where boundary conditions on the box walls are $0 < x < L_x$, $0 < y < L_y$, $0 < z < L_z$; (see Fig. 2.2) For this case, one can write down the solutions to the Schrodinger equation (5) immediately:

$$\psi_{n_1,n_2,n_3}(x, y, z) = \sqrt{\frac{8}{L_x L_y L_z}} \sin\frac{\pi x n_1}{L_x} \sin\frac{\pi x n_2}{L_y} \sin\frac{\pi x n_3}{L_z} \qquad (6)$$

$$E_{n_1,n_2,n_3} = \frac{\hbar^2 \pi^2}{2m^*}\left(\frac{n_1^2}{L_x^2} + \frac{n_2^2}{L_y^2} + \frac{n_3^2}{L_z^2}\right) \qquad (7)$$

where n_1, n_2, n_3 =1, 2, 3... . Of fundamental importance is the fact that $E_{n1,n2,n3}$ is the total electron energy, in contrast with quantum wells and wires, in which the solution for the bound state in a quantum well and wire (shaded areas in Fig 2.3 (a)) yields only the energy spectrum associated with transverse confinement. Another unique feature is the presence of three discrete quantum numbers resulting directly from the existence of the three directions of quantization. Thus we obtain threefold discrete-energy levels and wave functions localized in all three dimensions of the quantum box. Generally, all energies are different, i.e., the levels are not degenerate. However, if two or all dimensions of the box are equal or their ratios are integers, some levels with different quantum numbers coincide. Such a situation results in degeneracy: twofold degeneracy if two dimensions are equal and sixfold degeneracy for a cube. This discrete spectrum in a quantum box and the lack of free-electron propagation are the main features distinguishing quantum boxes from quantum wells and wires. As is well known, these features are typical for atomic systems.

The quantum dot itself doesn't constitute an object that has the quantum confinement ability of an electron. Quantum dots may exist as small crystal inclusions but in order to confine the electron or (hole) in all three dimensions its potential depth must exceed the minimum energy state of the lowest - order particle, U_{0min}, where:

$$U_{0\min} = \frac{\pi^2 \hbar^2}{8ml^2} \tag{8}$$

According to equation (7), the size of the quantum dot plays a fundamental role in the emission and absorption spectra originating from electron transitions between discrete photonic energy levels, E_n, which are system levels. With decreasing quantum dot size the discrete energy states become more separated in energy resulting in a blue shift of the emission spectrum.
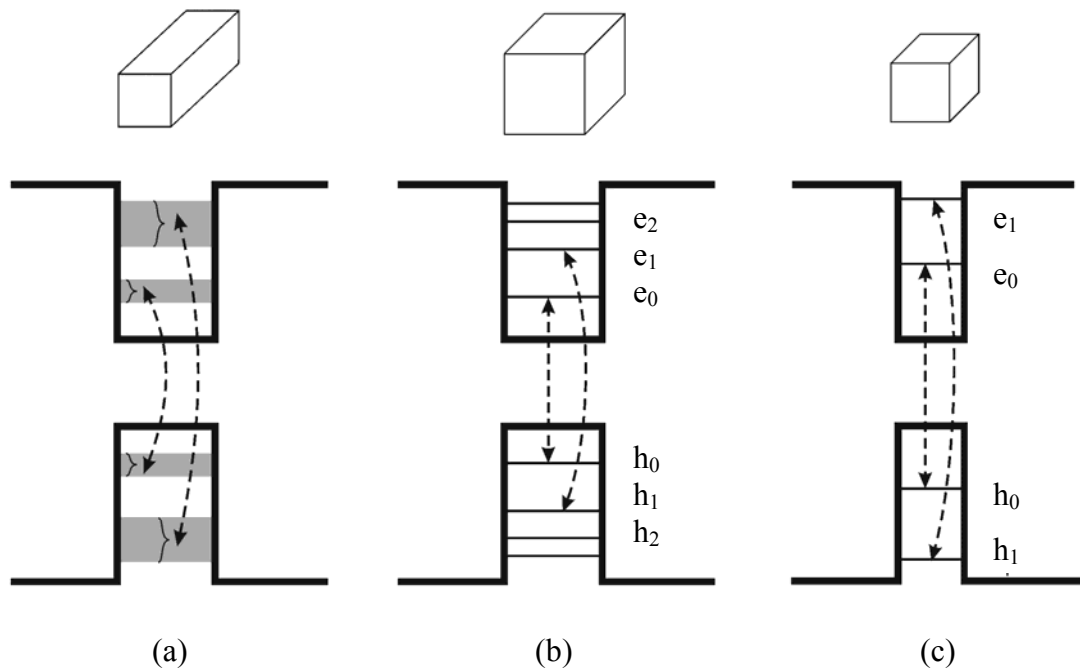
Figure 2.3   Two dimensional schematic band diagrams of (a) quantum wire with non discrete energy levels and two different size QD's with (b) large and (c) small characteristic dimension showing the origin of different photon energies resulting from the size of the QD

For this simple approach not all of the physical properties of the quantum dot are fully accounted for. In some materials the space dependence of the effective mass in heterostructures might lead to a strong interdependence of the longitudinal and transverse motion in systems with heterointerfaces such as quantum wells [27], quantum wires [28] and quantum dots [29]. The actual shape of the quantum dot plays also an important role since the electron and hole wave functions have different spatial distributions and they overlap differently in QD's of different shapes (see Figure 2.5). In most cases quantum dots have pyramidal or lens – like shapes, especially in the systems grown on substrates and nearly spherical shape in a liquid suspension form.

One of the long standing problems that has held back the development of accurate models for the energy states in semiconductor quantum dot heterostructures is the need to accurately determine the size, shape and composition of quantum dot samples. This problem is further compounded by the fact that while it is possible to determine the shape of dots using atomic force microscopy (AFM) before they have been capped with a GaAs "barrier", it is believed that the capping process itself induces the diffusion of gallium into the dots and diffusion of indium from the dots into the surrounding matrix [26]. Hence, AFM data for the size and shape of uncapped dots is of only limited use in evaluating the quality of theoretical models for capped dots. The earliest quantum dot samples were believed to contain pure InAs, pyramidal structures, with facets (see Fig. 2.4) forming 45° angles between the facets and the base. Following this interpretation of the structure, early calculations were also performed assuming a pyramidal geometry. More recent characterization using cross sectional TEM and STM measurements of capped dots, has predicted that a more realistic dot geometry and composition is a lens

18

shaped $In_xGa_{1-x}As$ quantum dot [30]. Williamson presented results of calculations for the

resulting energy states, excitonic band gaps and Coulomb matrix elements in lens shaped

$In_xGa_{1-x}As$ quantum dots embedded in GaAs matrices in a similar configuration to the

samples investigated during this dissertation research.
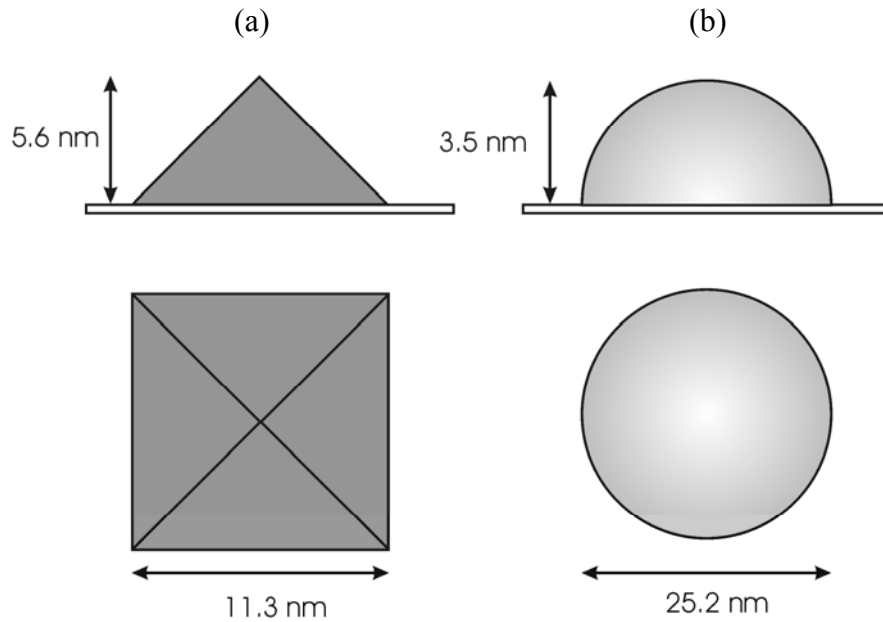
Figure 2.4 Assumed geometry of the (a) pyramidal and (b) lens shaped dots for which

wave functions were calculated by Williamson [30] as shown in Figure 2.5
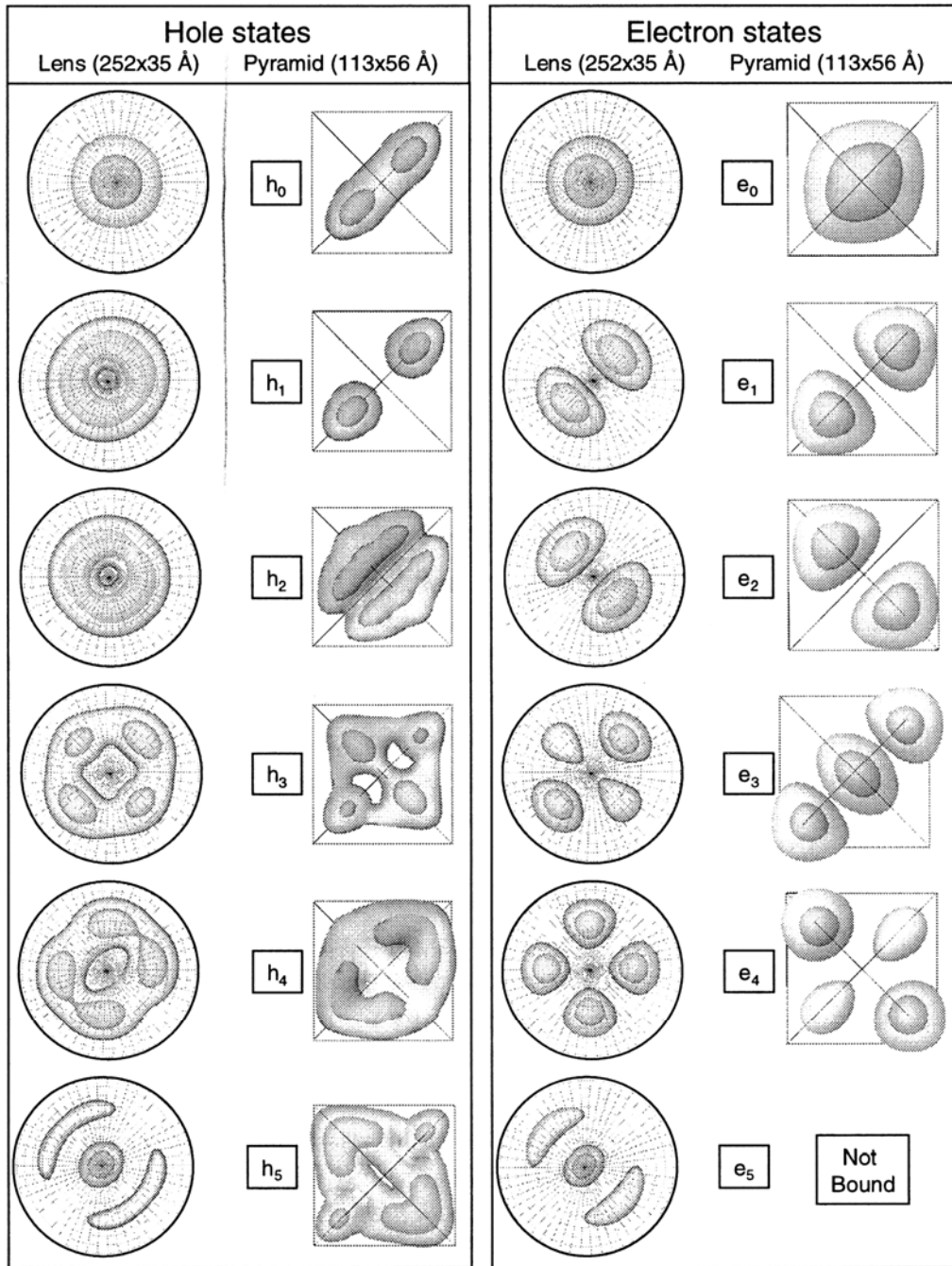
Figure 2.5 Top view of the calculated electron and hole wave functions squared (space occupation probability) for the InAs QD geometries shown in Figure 2.4 after Williamson [30]. The light and dark areas represent 20% and 60% charge density

In the case of quantum boxes or dots the electron energies are discrete and the density of states function is simply a set of delta-shaped peaks:

$$\rho(E) = \sum_v \delta(E - E_v) \qquad (9)$$

where $v = (n_1, n_2, n_3)$, $\rho(E)$ the density of states. For an idealized system, the peaks are very narrow and infinitely high, as illustrated in Figure 2.1 (d). In fact, interactions between electrons and impurities as well as collisions with phonons bring about a broadening of the discrete levels and, as a result, the peaks for physically realizable systems have finite amplitudes and widths. Nevertheless, the major trend of sharpening the spectral density dependences as a result of lowering the system dimensionality is a dominant effect for near-perfect structures at low temperatures.

There are many other reported works in the literature [19, 30-35] devoted to the theoretical considerations of the quantum dot band structure for many different QD material compositions and shapes. For the particle in a spherical potential well there are theoretical models in the literature proposed by Efros [31, 35]. For lens-like and pyramidal shapes the electronic structure was calculated by Williamson [30] and Grundmann et al [36].

Elastic strain/stress at the hetero-structure interface also contributes to the optical properties of QD's. More stressed interfaces are prone to have more defects that directly influence the optical output [37]. Impurity atoms and native crystal structural defects also cannot be neglected. For quantum dot ensembles the size distribution is responsible for the inhomogeneous broadening of the emission spectra, creating additional factors that must be taken into account during the PL study of quantum dots.

2.3. Quantum dots in compound semiconductors

2.3.1. Quantum dots in group III-V element systems

Semiconductor quantum dots in III – V systems have been reported in the literature for over two decades. Their first discovery was made by the failure to grow thin layers of InAs over GaAs substrates attempted by Goldstein, et al. [38]. It was observed that after some critical thickness the planar growth mode jumps to 3D nucleation growth forming small InAs islands over the surface. Since then, quantum dots have been continuously reported in variety of III-V ternary and binary systems [20, 39-43].

2.3.1.1. Growth modes and methods

The classification of the well known three growth modes dates from 1958, when Ernst Bauer wrote a much quoted review papers in Zeitschrift fur Kristallographie [44, 45].

The Layer-by-Layer, or Frank- van der Merwe, growth mode arises because the atoms of the deposit material are more strongly attracted to the substrate compared to each other.

In the opposite case, where the deposit atoms are more strongly attached to each other than they are to the substrate, the Island, or Volmer-Weber mode, results.

An intermediate case, the Layer-plus-Island, or Stranski-Krastanov [46] ("S-K") growth mode is when the initial layer formation is followed by 3D island nucleation after

the initial layer thickness reaches some critical value. In this case, layers form at first and then it is more favorable for the whole system (from the thermodynamical point of energy conservation) to switch into 3D island creation mode.

Bauer was the first to systematize these growth modes in terms of surface energies. If we deposit material A on B, we get layer growth if $\gamma_A < \gamma_B + \gamma^*$, where γ^* is the interface energy, and vice-versa for island growth. The S-K mode arises because the interface energy increases as the layer thickness increases; typically this layer is strained to fit the inter-atomic distance to the substrate. Pseudomorphic growth is the term used when it fits exactly. In the island growth mode, the adatom concentration on the surface is small at the equilibrium vapor pressure of the deposit; no deposit would occur at all unless one has a large supersaturation. In layer growth, the equilibrium vapor pressure is approached from below, so that all the processes occur at undersaturation. In the S-K mode, there are a finite number of layers on the surface in equilibrium. The new element here is the idea of a *nucleation barrier*. The existence of such a barrier means that a finite supersaturation is required to nucleate the deposit. For Quantum Dots the creation of the S-K mode is the predominant one.
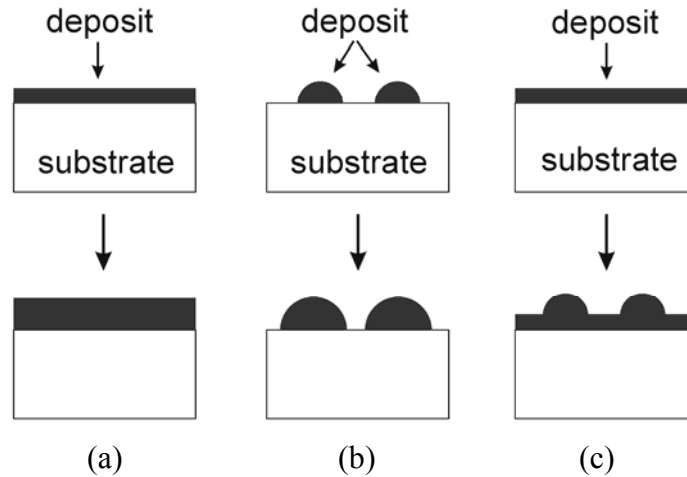
Figure 2.6   Schematic diagram of three possible growth modes after [Bauer]: (a) – Frank-van der Merwe, (b) – Volmer-Weber, (c) – Stranski-Krastanov, which is the mode responsible for QD growth

There is also a fourth growth mode called the Turing mode [47], it was found in 1993 by Temmyo [48] and occurs in a strained InGaAs/AlGaAs semiconductor heterostructure system on a GaAs substrate as a novel phenomenon leading to the formation of well-ordered arrays of nanocrystals with built-in InGaAs strained quantum disks with diameters ranging between 30 and 150 nm. The built-in quantum disks within the nanocrystals can exhibit a strong, narrow line photoluminescence emission at room temperature. Turing instability is responsible for their rearrangement phenomenon and selforganization. It also suggests the existence of a novel fourth growth mode on the high Miller index faces of III–V semiconductors.
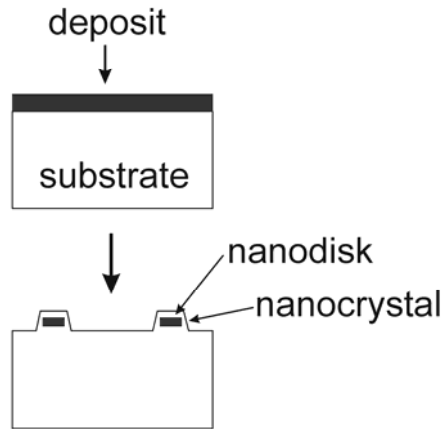
Figure 2.7 Schematic of the Turing growth mode (after Temmyo) [48]. Note the formation of "nanodisk" inside the nanocrystals

Among the possible deposition techniques Molecular Beam Epitaxy (MBE) and metalorganic chemical vapor deposition (MOCVD) are the most widely employed. The MBE method utilizes solid phase sources for Ga, Al and In, as well as Ga and As and Sb. For the N source a nitrogen plasma or ammonia serve as major sources [40, 49, 50].

The first reported MOCVD grown QD were performed by Dimitriev et al. [51] who grew GaN QD's directly on 6H-SiC. This work was followed by Tanaka and others [52-54] and eventually led to a new method called the anti-surfactant growth mode.

There are a few other techniques reported in the literature for III-V QD creation. Goowin et al. [55] used reactive laser ablation of pure Ga in a high purity N_2 atmosphere. Nanocrystalline films were created by a sputtering technique of GaAs material on quartz substrates [56] and by the means of pyrolysis (chemical decomposition of organic materials by heating in the absence of oxygen or any other reagents) reported by Wells et al. [57, 58].

2.3.1.2.   Properties of III – V quantum dots

In the InGaAs/GaAs systems the 2D to 3D growth mode transition was used during the initial stages of growth of highly strained InGaAs on GaAs to obtain quantum-sized 3D (i.e. QD) structures. These dislocation-free islands (dots) of InGaAs had a size of 30 nm in diameter and 10% size dispersion. Photoluminescence spectra displayed a maximum emission at 1.2 eV [59] which is why this type of QD is widely used in optoelectronics for the IR part of the spectrum.

For the InGaAs/AlGaAs system arrays of vertically aligned quantum dots in a matrix have been investigated. In this system it was shown that increasing the band gap of the matrix material makes it possible to increase the localization energy of quantum dots relative to the edge of the matrix band [20], as well as the states of the wetting layer. The wetting layer is the residue after coating a surface with layers of atoms under high temperature during MBE creation of quantum dots, which can interfere with the stimulation of the dot growth influencing the final size and shape. QD's of this type reported in literature have PL maxima around 1.3 eV for 5-7 nm QD sizes [60].

The InAlAs/AlGaAs system has a visible luminescence obtained from ensembles of defect-free, $In_xAl_{(1-x)}As$ islands of ultra small dimensions embedded in $Al_yGa_{(1-y)}As$ cladding layers grown by the MBE technique [17]. Structural and optical properties of InAlAs quantum dots (QD) were studied as a function of the InAs mole fraction (x). Decreasing of x resulted in a sequential disappearance of the bound electron and hole states in these QDs [61].

In the InP/InGaP system the transition towards three-dimensional Stranski–Krastanow (SK) island growth occurs before the second monolayer of InP is formed and vertical alignment of grown QD's also occurs improving the overall photoluminescence properties [62]. The width of the emission peak at half maxima value is 41 meV for a single layer of QD's while for triple layers it is reduced to 26 meV [42]. Reported PL maximum is 1.757 eV for InP QD used for laser applications, which are 5-7 nm in lateral dimension [41].

InAs/InAlAs displays a room temperature photoluminescence (PL) emission at 0.7 up to 0.8 eV [63]. Molecular beam epitaxy was used to grow InAs self-assembled quantum dots in InAlAs on an InP substrate [64].

For InAs/InGaAs the InAs dot size has been found to be 3–4 times larger than in an InAlAs matrix for the SK growth mode, but the lateral QD's density is about an order of magnitude smaller [64]. Low-temperature photoluminescence (PL) of the InAs/InGaAs quantum dots is characterized by a narrow (35 meV) PL line as compared to that of InAs/InAlAs quantum dots (170 meV). Quantum dot formation increases the carrier localization energy as compared to quantum well structures with the same InAs thickness in a similar manner for both InAs/InGaAs and InAs/InAlAs structures [64].

In the InAs/InP: in III-V element binary combination two different modes of island size and spatial distribution have been identified. For a deposit of 1.5 and 1.8 monolayers, the islands are about 7 nm high and randomly distributed. Above 2 monolayers, they are about five times smaller in volume and locally self-organized, with a typical distance of 40 nm independent of the island density [65]. The peak wavelength

from the InAs QDs can be continuously tuned from above 0.77 down to 0.73 eV at room temperature [66].

InP grows pseudomorphically on GaP for 3 ML before island crystallization is observed by reflection high-energy electron diffraction (RHEED), following a typical Stranski–Krastanov growth mode [67]. Photoluminescence and cathodoluminescence spectroscopy reveal large inhomogeneous broadening with the emission peak centered at 1.7 eV for room temp PL [68].

Finally there is the InAs/GaP system. For the growth of InAs on GaP, three-dimensional diffraction peaks are observed after 0.9 ML of InAs have been deposited, indicating a Volmer–Weber growth mode [67]. A maxima of the PL emission is in infrared range around 1.6 eV [68].

2.3.1.3. III – V QD applications

The major use for III-V quantum dots is in the solid state lasers for the next generation of high-speed optical communication devices[20, 69]. The atomic-like density of states improves optical performance of semiconductor lasers resulting in low-threshold lasing, high-temperature operation, low chirp (frequency change due to dispersion) [4], and improved high-speed modulation. In particular, recent development of well controlled high-quality self-assembled QDs contributes to the development of new optical devices such as QD semiconductor optical amplifiers [70] (SOA) and Quantum Dot laser LED's [21] for the infrared region.

Apart from obvious optical applications there have been attempts made in quantum computing based on these specific optical properties [22]. Quantum computing is based mostly on dot to dot interaction that can be easily controlled via their separation distance. For example in the simplest case of two quantum dots that exhibit weak coupling there are two interband resonances at frequencies ω_1 and ω_2 if the system is singly excited. It is thus possible by using ultra fast two color laser pulses (centered at ω_1 and $\omega_2 + \delta\omega$) to create a photon absorption at $\omega_2 + \delta\omega$ conditional to the occupancy of the QD-pair by an electron-hole created by the absorption of a photon at ω_1; hence the possible use of the QD pair for simple optical logic operations.

Quantum dots have been also applied in the 3rd generation (low cost, high efficiency) of solar cells in the photovoltaic industry [23]. The first advantage derived from the use of quantum dots stems from their tunable bandgap. High currents and voltages are desired for efficient solar-electric conversion. Thus, there exists an optimum bandgap that corresponds to the highest possible solar-electric energy conversion. Quantum dots provide a much more exact method of matching the bandgap of the solar cell material to the optimum bandgap than traditional semiconductor materials for energy conversion, resulting in greater efficiencies. Secondly, in contrast to traditional semiconductor materials which are often rigid in form, quantum dots can be molded into a variety of different forms. This formation processes may allow for the creation of ordered 3-D arrays with inter-quantum dot spacing sufficiently small such that strong electronic coupling occurs and minibands are formed to allow for long-range electron transport for better electron extraction [23].

2.3.2. Quantum dots in group II – VI element systems

Semiconductor QD's in II-VI systems were first discovered as nanosize crystal inclusions in glass matrices [3]. The properties of bulk II-VI materials have been investigated for over 40 years [71, 72], while nanosize II-VI structures have received much attention as synthesis methods have been recently developed for CdSe that leads to an unprecedented degree of monodispersity (the state of uniformity in molecular weight/size of all molecules of a substance) and crystalline order [73], allowing detailed investigations of the size-dependent optical absorption and emission.

For these systems the most common nanocrystallites are cadmium binary compounds such as CdO, CdS, CdSe and CdTe along with zinc compounds ZnO, ZnSe, ZnS (used only as the shell material) and ZnTe and mercury compounds HgS and HgTe.

2.3.2.1. Growth modes and creation techniques

The majority of nanocrystallites of II-VI semiconductors are embedded into glass or oxide matrices [74] apart from colloidal solutions where the QD's are suspended in liquids. The same techniques for III-V quantum dots also apply to II-VI nanostructures especially MBE epitaxy [37, 40, 52, 63-65, 75, 76], though the majority of commercially available QD products are created using colloidal particle growth in a solvent media. These include: creation from supersaturated glass solution [77], an arrested precipitation technique [78], pyrolisis [79], and aqueous colloidal growth [80, 81].

Compared to self-organized dots, nanocrystallites suffer from poor interfaces as far as their optical properties are concerned. They are usually smaller (hence display larger size quantization) and easier to produce, but their surface problems have detrimental consequences on their emission properties such as the "blinking effect" [82, 83].

For biological tagging applications CdSe/CdTe (core) nanocrystals are the most popular. They are covered with a wide-gap ZnS or CdS (shell) capping layer providing a barrier for quantum confinement and also improved quantum yield and photo stability.
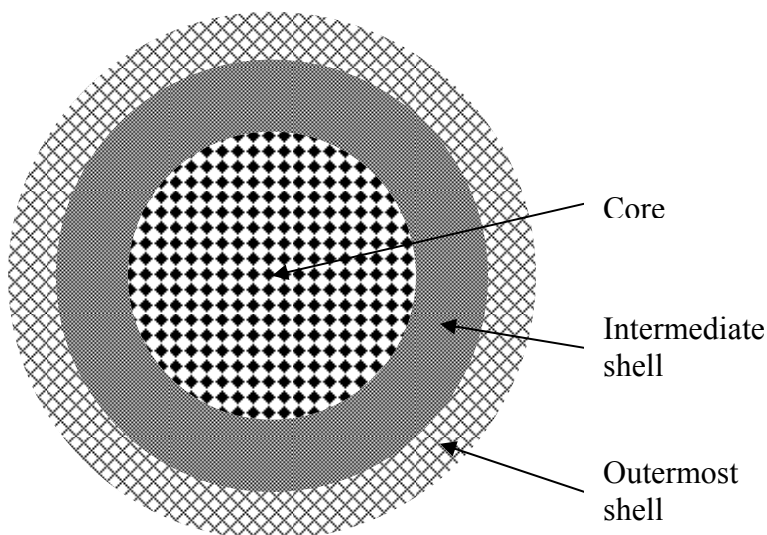
Figure 2.8 Schematic diagram of a typical core-shell nanoparticle used for bio-tagging. This figure represents the scheme with the highest quantum efficiency design, in some cases the core is protected only by single-layer shell [7]

Most of the quantum dots for fluorescent imaging typically possess a core-shell structure where the core is fluorescent. The nanoparticle shell is to protect the core from photobleaching and to improve the dispersibility in aqueous media. The shell structure

can also be designed to obtain appropriate surface functional groups for attaching biomolecules. In some cases the core is encapsulated by multiple shell structures for improved detection capabilities with fluorescent and magnetic detection done simultaneously [80].

2.3.2.2.   Properties of II – VI quantum dots

Although CdO is often used to produce CdS and CdTe quantum dots as the cadmium source, there are very few reports of the QD's created from CdO itself. Radi et al [81] reports CdO quantum dots incorporated in polyacrylamide that were synthesized by adding an aqueous suspension of cadmium oxide in acrylamide of bisacrylamide copolymer. The size ranges between 2 and 3 nm [84, 85].

For MBE growth of CdS coherently strained layers on ZnS or ZnSe substrates of the SK formation type of QD is observed [79]. It was found recently that CdS QDs could be grown with either circular or rectangular shapes depending on the growth conditions forming a 3D spherical lens as well as tetrahedral shapes [72]. These CdS quantum structures show efficient photoluminescence and optical gain in the deep blue to ultraviolet spectral range [71]. It has been found that in wide-gap II-VI systems (CdS and CdSe mostly) quantum structures with small monolayer fluctuations result in such a strong localization of excitons that the exciton binding energy reaches energies around 100 meV. CdS QD's usually range in size between 2 and 10 nm [74]. For colloidal methods of creation the size dispersion can be as small as 5% for these type QD's [80].

CdSe QD's were the first to become highly luminescent at room temperature with quantum yields of 30-50% when grown as core/shell structures [13]. CdSe/ZnS composite quantum dots with CdSe usually have cores ranging in diameter from 23 to 55 Å [86]. The narrow photoluminescence (FWHM 40 nm) from these composite dots spans most of the visible spectrum from the blue through the red. For CdSe as well as for CdTe the photoluminescence intermittency effect is observed [35, 72, 87].

Self-assembled CdTe quantum dots form when grown by molecular beam epitaxy on ZnTe substrates [75]. They also form QD structures in glass matrices. Formation of QDs usually starts after deposition of 1.5–2.5 monolayers of CdTe for the MBE method. The resulting dots have a typical diameter of 2 nm and a planar density of 10^{12} cm^{-2} [75]. The photoluminescence spectra consist of two emission lines. The high-energy line originates from excitonic recombination in a wetting layer which is required for their formation while the low-energy emission PL band is assigned to recombination in CdTe quantum dots [88]. The activation energy of the thermal quenching of QD - related PL emission was found to be equal to 47 meV [75].

ZnSe quantum dots have been reported as colloidal synthesized nanoparticles with an arrested precipitation technique [77], or more recently they are prepared from a supersaturated glass solution [78]. Coating ZnSe quantum dots with a ZnS monolayer yields a remarkable enhancement in the PL quantum efficiency at room temperature without affecting the spectral distribution. The result suggest that passivation of surface states, along with an increased localization of the holes in the core ZnSe layer, gives rise to a high luminescence quantum yield [18]. The controlled growth process affords tunable sample sizes with band-edge fluorescence size-tunable between 2.8 and 3.4 eV is

obtainable at room temperature with quantum yields between 20% and 50% relative to Stilbene 420 [77].

Nanocrystals of ZnTe in colloidal form were reported by Jun et al [89] though this material is mostly used as a host matrix for other telluride QD's. The resulting nanocrystals are relatively large (length 500–1200 nm, width 30–100 nm). Their optical properties were investigated without isolation or characterization of the nanocrystals. In fact, there have not been any reports on isolated ZnTe nanocrystals below 10 nm in size.

There are not too many reports about HgS type of QD as they are mostly mentioned in theoretical works. Though colloidal mercury sulfide QDs synthesized at room temperature have been reported [90]. HgS material also serves as a host material for epitaxial growth in a CdS/HgS heterostructure of nanometer dimensions, prepared by wet chemistry methods [90].

Kershaw et al. [88] reports an aqueous colloidal growth technique of HgTe QD's to form quantum dots with a broad, strong fluorescence in the infrared (~1.0–1.5 eV) region. The reported quantum efficiency was high, around 44%, when pumped in the visible (~2.54 eV), and the excited state lifetime was around 130 ns, making the material interesting as an optical amplifier medium.

2.3.2.3.   II – VI QD applications

II-VI semiconductor QD'd have found application in optoelectronics where their optical properties are widely employed in light-emitting diodes [91] and solid-state lasers [4]. For laser applications ZnSe is very promising QD material, with a room temperature

bulk band gap of 2.7 eV (460nm), and has long been a material of choice for blue diode lasers [77]. Creating ZnSe QD's will allow emission even further into the ultra-violet region.

More recently developed colloidal nanostructures including core-shell QD's. Elongated rods [92] and mixed semiconductor quantum dots [93] have been used in biosensing [94] and bio-labeling [12] where they are used as fluorophore substitutes. Their role is to provide a fluorescent signal that allows the detection and tracking of specific bio-molecules that QD's are attached to.

More advanced bio-labeling techniques involve mixing semiconductor QD's allowing for multicolor optical coding for biological assays (so called multiplexing) [93]. This has been achieved by embedding different-sized quantum dots into polymeric microbeads at precisely controlled ratios, which makes them ideal fluorophores for wavelength-and-intensity multiplexing. The use of 10 intensity levels and 6 colors could theoretically code one million nucleic acid or protein sequences. Imaging and spectroscopic measurements indicate that the QD-tagged beads are highly uniform and reproducible, yielding bead identification accuracies as high as 99.99% under favorable conditions [93].

One of the interesting applications of II-VI QD's is their use as temperature sensors [95]. The steady-state photoluminescence properties of cadmium selenide QD's are strongly dependent on temperature in the range from 100 to 315 K. The PL intensity from these QD's matrices increases by a factor of ~5 when the temperature is decreased from 315 to 100 K, and the peak of the emission band was blueshifted by 20 nm over the same range. This dependence is linear and reversible (−1.3% per °C) for temperatures

close to ambient conditions. The significant temperature dependence of the luminescence, combined with its insensitivity to oxygen quenching, establishes these QD's as optical temperature indicators for temperature-sensitive coatings making an another possible application.

2.4.   Biomarkers

A biomarker is a biological parameter/material (gene, metabolite or protein) that is indicative of a physiological or pathological state. For this being an overall definition of a biomarker in ex-vivo as well in in-vivo cancer detection techniques the biomarker is a substance used as an indicator of a biologic state. It can be any kind of molecule indicating the existence (past or present) of living cells, proteins, etc [96].

In biology and medicine, a biomarker can be a substance whose detection indicates a particular disease state (for example, the presence of an antibody may indicate an infection or cancer). Such a biomarker can be native to the body. A biomarker can also be used to indicate exposure to various environmental substances in epidemiology and toxicology. In genetics, a biomarker (identified as a genetic marker) is a fragment of a DNA sequence that is associated with, changes susceptibility to disease, or causes disease [96].
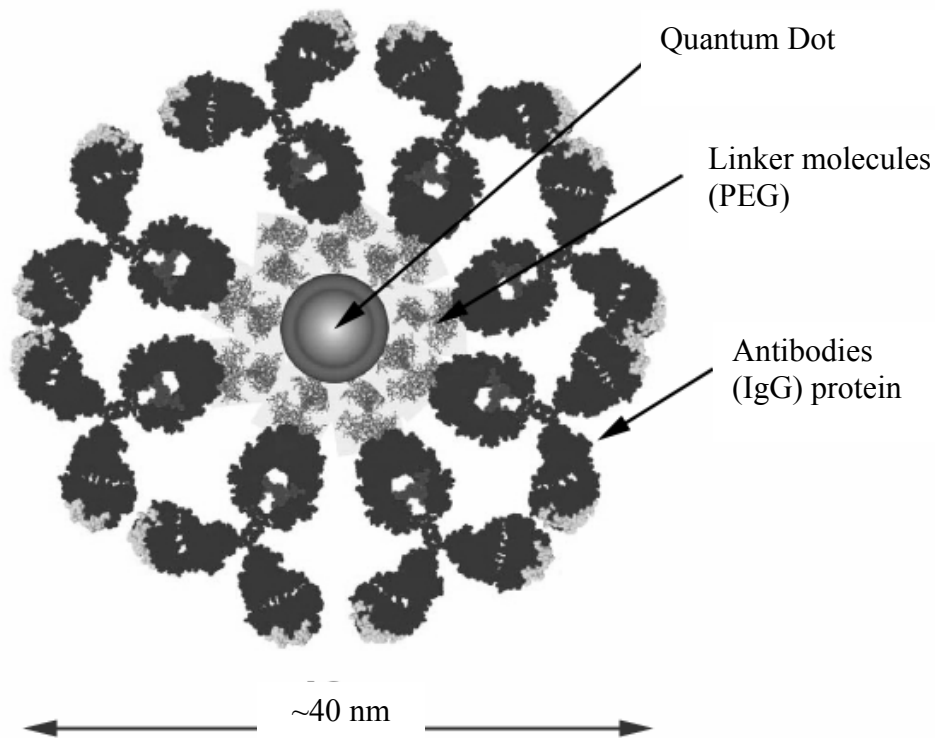
Figure 2.9 Schematic representation of the QD bound to a biomarker (molecules are drawn to scale) – after Jaiswal [97]. Single QD in the center is attached to the detector antibodies (IgG proteins) via linker molecules (PEG). Note that not all linker molecules are utilized

For the purpose of this research four anti-bodies, anti-gene biomarker groups were selected: IL-10, CA125, PSA (Prostate Specific Antigen) and Osteopontin. These anti-bodies target their specific anti-genes and serve the purpose of early stage ovarian, prostate and other cancer detection. The overall conjugate scheme is presented in Fig 2.9 with the QD and antibodies drawn approximately to scale. Ovarian cancer causes more deaths each year among women than any other gynecologic cancer. For this type of cancer survival rates are 30% for patients that are diagnosed with advanced (past stage

III) disease. However, 5-year survival rates are less than 20%. In contrast 80-90% 5-year survival rates are associated with patients diagnosed with Stage I or II ovarian cancer. These statistics provide the primary rationale to improve ovarian cancer screening and early detection [98].

Stages in cancer development are as follows:

- Stage I - the cancer has not spread past the tissue or organ where it started.

- Stage II - there is some local and regional spread of the cancer, sometimes to lymph nodes.

- Stage III - there is extensive local and regional spread of the cancer, usually to draining lymph nodes.

- Stage IV - the cancer has spread (metastasized) beyond the regional lymph nodes to distant parts of the body.

Interleukins (ILs, IL10) are a large group of cytokines (proteins) that are produced mainly by leukocytes, although some are produced by certain phagocytes and auxiliary cells. ILs have a variety of functions, but most of their function is to direct other immune cells to divide and differentiate [99, 100]. Each IL acts on a specific, limited group of cells through a receptor (protein on the cell membrane or within the cytoplasm or cell nucleus that binds to a specific molecule [101]) specific for that IL. Human IL10 (which is used in this research) is a non glycosylated polypeptide consisting of 160 amino acids. There is 73% homology between the human and mouse IL10 proteins that we have used in our conjugation experiments, however, the human IL10 acts on both human and mouse target cells, while the mouse IL10 has species-specific activity.

Cancer antigen 125 (CA125) is a protein found on the surface of many ovarian cancer cells and it also has been chosen for bioconjugation is our experiments. It can be found in other cancers and in small amounts within normal tissue. CA125 is used as a tumor marker as indicator of some types of cancer, especially ovarian cancer [102]. Studies are being done to determine whether CA125 can be used as a screening test for ovarian cancer. Most often, the CA125 test is used to help determine the effectiveness of treatment for ovarian cancer or to help diagnose the recurrence of ovarian cancer [103]. CA125 is a high-molecular-weight glycoprotein that is recognized by the monoclonal antibody OC125 and is elevated in most women with ovarian cancer. CA125 is the most extensively studied biomarker for possible use in the early detection of the disease [103]. This antibody stains the membranes of epithelial cells in most non-mucinous epithelial ovarian carcinomas. Normal ovarian epithelium, breast, gastroinetestinal tract, liver and skin tissue are negative when exposed to this antibody [104].

Prostate Specific Antigen (PSA) is a molecule produced by the normal prostate and secreted in large amounts in the male semen and is also normally present in minute quantities in the male bloodstream. It is now well known and accepted that PSA levels in the blood are elevated by several disease processes in the prostate, most importantly by prostate cancers. This molecule belongs to a group of kallikreins (class of peptidases/enzymes that cleave peptide bonds in proteins [105]) that are a subgroup of serine proteases having diverse physiological functions. This is another biomarker which is used in our bioconjugation experiments. Growing evidence suggests that many kallikreins are implicated in carcinogenesis and some have potential as novel cancer and other disease biomarkers [106]. This gene is one of the fifteen kallikrein subfamily

members located in a cluster on chromosome 19 [107]. Serum level of this protein, called PSA in the clinical setting, is useful in the diagnosis and monitoring of prostatic carcinoma. Alternate splicing of this gene generates two transcript variants encoding different isoforms (version of a protein with some small differences in amino acid sequences, folding etc.). Additional transcript variants have been described, but it is unclear if these transcripts are normally expressed or if they are specific to benign or malignant tumors [108].

Osteopontin is the last biomarker employed and bioconjugated by us. It is a glycoprotein identified in osteoblasts (cells that build and reshape bones). The prefix of the word "osteo" indicates that the protein is expressed in bone, where it is one of the extra cellular structural proteins that constitute the organic part of bone. This protein is composed of ~300 amino acids and is rich in acidic residues: 30-36% is either aspartic or glutamic acid [109]. Osteopontin is synthesized by a variety of tissue types including preosteoblasts, osteoblasts, osteocytes, extraosseous cells in the inner ear, brain, kidney, placenta, odontoblasts, some bone marrow cells, macrophages, smooth muscle, and endothelial cells [109]. Osteopontin is over expressed in a variety of cancers, including lung cancer, breast cancer, colorectal cancer, stomach cancer, ovarian cancer, melanoma and mesothelioma [110].

2.5.   Summary

Size-tunable optical properties have become a hallmark of quantum dots and related nanostructures. These properties are currently under intensive study for potential

use in optoelectronics, high density memory, quantum-dot lasers, and lately for biosensing [12] and biolabeling [95]. Recent advances have led to the development of colloidal nanostructures including core-shell quantum dots and other non-spherical nanoparticles, as well as quantum-dot quantum-well (QDQW) heterostructures, and mixed semiconductor dots [93]. Sometimes tuning of electronic, optical, and magnetic properties by changing the particle size could cause problems in many applications such as nanoelectronics, superlattice structures, and biological labeling and there are first reports about adjusting emission wavelength without changing the particle size but its composition [111]. There are still not many reports about the influence of the surrounding molecules on their photoluminescence properties, along with the spatial large area investigations of these parameters fluctuations.

This research is focused on the non uniformity of the QD optical parameters across the QD matrices to investigate and explain possible mechanism of it. This is an important piece of information for the manufactures of self assembled QD samples since most of the sample properties come from the growth condition fluctuations, like capping layer composition, temperature of growth, annealing etc.

The other part is devoted to the influence of the surrounding molecules on the optical properties of the II-VI QD systems for bio medical applications as fluorescent tags. The spectral features induced by biomolecules proximity may have the large influence on the use of QD's as the labels for given biomarker detection. The specific sample details along with the experimental setups are described in the next chapter.

3.   Quantum Dots Experiments

3.1.   InAs/InGaAs QD samples

This set of samples contains InAs/InGaAs self-assembled quantum dots on GaAs substrates grown in the Stranski–Krastanow (S-K) growth mode. These samples were prepared by Dr. Andreas Stintz from Center of High Technology Materials at the University of New Mexico. Structures were created on GaAs at different growth temperatures from 470 to 535°C. Solid-source molecular beam epitaxy (MBE) in a V80H model reactor was used for growth of three InAs self organized QDs layers inserted into $In_{0.15}Ga_{0.85}As$/GaAs Multi Quantum Wells – there are three QD/QW structures placed on top of each other (Fig 3.1). The Stranski-Krastanov [46] (S-K) growth mode is responsible for the self assembled creation of QD's in this case. In the growth process the initial layer formation is followed by the 3D island nucleation after the initial layer thickness reaches some critical value (2.4 ML for InAs). The InGaAs/GaAs structures were grown under As-stabilized conditions at different substrate temperatures: 470 °C (#684), 490 °C (#685), 510 °C (#687), 525 °C (#689) and 535 °C (#698), during the deposition of the InAs active regions and InGaAs wells and 590-610°C for the remaining layers of the structure [112, 113]. The dot density (2.5-5.3) $\times 10^{10}$/cm^2 was determined by

AFM measurement of surface roughness on a parallel wafer with open QDs that have not been overgrown by the QW and cladding layers.
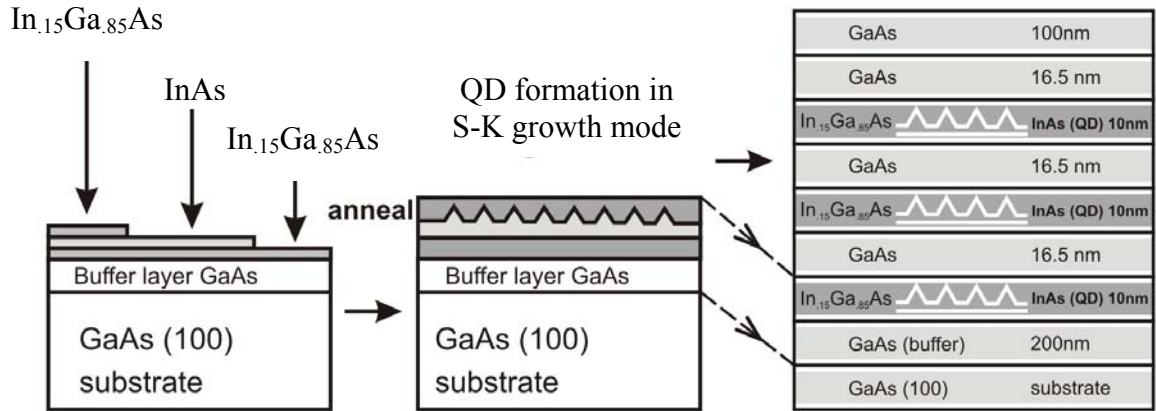
Figure 3.1   Schematic structure of multi quantum well and quantum dot "sandwich" of InAs/InGaAs samples. These samples were prepared by Dr. Andreas Stintz from Center of High Technology Materials at the University of New Mexico

In addition to growth temperature changes, the effect of cladding layer composition was also studied. A set of similar samples grown at 590-610°C with varied InGaAs cladding layer was measured. These samples had an $In_xGa_{1-x}As$ layer composed of x=0.1 (10%) (#1361), 15% (#1360) to 20% (#1363), respectively. They were created using the molecular beam epitaxy technique. Each sample was composed of three InAs self-organized QD arrays embedded into external $In_{0.15}Ga_{0.85}As$/GaAs strained multi quantum wells. AFM studies of sister samples without overgrown capping layers showed that individual QD's were of 15 nm in base diameter and approximately 7 nm in height. The in-plane density was 7-10 x 10^{10} cm^{-2}. Physical dimensions of this set of samples was 1 x 2 cm approximately and they were cutouts from larger 2 inch wafers cut in the way that each sample contained the wafer periphery and some inner area portion.

For the spatially resolved PL studies of InAs QD's the whole 50mm wafer was used. The experimental set of samples was created in a similar way to the previous 13XX sample series. All investigated QD structures had a $In_{0.15}Ga_{0.85}As$ buffer layer under the wetting layer. A variable parameter similar to the 13XX series was the In-composition of the $In_xGa_{1-x}As$ capping layer, which covers the InAs QDs. Four different compositions of the cap layer were studied with x = 0.10 (#1718), 0.15 (#1719), 0.20 (#1720) and 0.25 (#1721). Sister samples with exposed QD layers showed that the individual dots were of 15 nm in base diameter and approximately 7 nm in height. The measured in-plane dot density was 3–5 x 10^{10} cm^{-2}.

3.2.   CdSe/ZnS QD samples

QD nanocrystal samples used in this part of the research are fluorophores — substances that absorb photons of excitation light, and re-emit photons at a different wavelength. All samples used in this part of the experiments were purchased from the Quantum Dot Corp. (now Invitrogen, Inc.) All quantum dots had a CdSe core of different diameter and ZnS shell as illustrated in Fig 3.2. This core/shell material is further coated with a polymer shell that allows the material to be conjugated to biological molecules and to retain their optical properties.

10 -15 nm
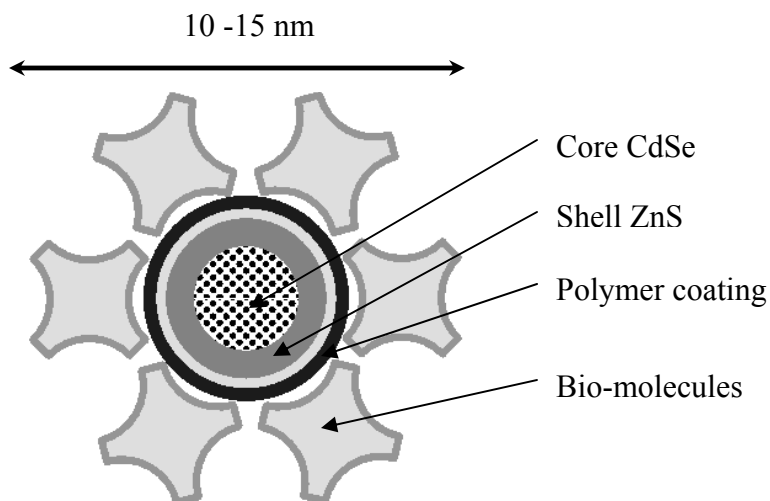
Figure 3.2   Schematic   representation   of   the   bioconjugated   quantum   dot   (after
          Invitrogen, Inc) [11]

Some of the samples were purchased already conjugated to linker molecules
(Table 3.1). The number in the product label represents the peak position of the photo-
luminescence spectrum in nanometers (e.g, QD525 has a peak wavelength of 525 nm,
etc.).

Table 3.1 QDot.com samples description

Qdot.com product	Conjugation	Volume / Concentration
QD 525	F(ab')$_2$ fragment conjugate	50 µl at 10 mM
QD 655	Streptavidin conjugate	50 µl at 10 mM
QD 525 (conjugation kit)	Pure non conjugated	250 µl at 10 mM
QD 565 (conjugation kit)	Pure non conjugated	250 µl at 10 mM
QD 605 (conjugation kit)	Pure non conjugated	250 µl at 10 mM
QD 655 (conjugation kit)	Pure non conjugated	250 µl at 10 mM
QD 705 (conjugation kit)	Pure non conjugated	250 µl at 10 mM

These QD nanocrystals are nanometer-scale (roughly protein-sized) atom clusters as illustrated in Fig 3.2 which is approximately drawn to scale. For the non conjugated quantum dots, conjugation was performed according to supplied conjugation protocols [114] with the following bio-molecules:

Table 3.2 Biomarkers molecules chosen for bio-conjugation experiments

Biomolecule type	Supplier	Additional info
OC 125 (mouse anti-human OC125, mouse IgG)	DakoCytomation (Carpinteria, CA)	stock concentration -679 mg/L, code M3519
CA 125 (cancer antigen 125)	Fitzgerald Industries (Concord, MA)	stock concentration - 1000000 U/ml
Interleukin 10 (anti human IL10, rat IgG2a)	Serotec (Raleigh, NC)	stock concentration 1 mg/ml, clone JES3-12G8, code MCA2250
Recombinant human IL10	Serotec (Raleigh, NC)	stock concentration 1mg/ml, code (PHP047A)
PSA (anti prostate specific antigen, mouse IgG1),	Chemicon International (Temecula, CA),	stock concentration - 5.14 mg/ml, code MAB4082
Osteopontin (anti human Osteopontin, mouse IgG)	Assay Designs (Ann Arbor, MI),	stock concentration 1mg/ml, code 905-078

3.2.1. Bio-conjugation substrates

For the bioconjugation experiments different substrates were used. Surface chemistry for ELISA plates is basically the same i.e. binding of the capture antibodies is

done via biotin-streptavidin bridge or direct protein immobilization on the aldehyde surface. However the substrate material of the plate can be optimized to reduce the intensity of the background photoluminescence signal, which superimpose with the PL from the QD's. For the photoluminescence measurements background signal elimination is a critical step allowing low PL intensity study to be performed. These are the ELISA substrates that have been tested and used in the experiments:

Table 3.3 ELISA plate types

ELISA plate type	Manufacturer
FluoroNunc Flat Bottom Maxi Sorp	NUNC
Black Bio-Bind Assembly streptavidin coated	Thermo electron
White microtiter plate	Thermo Labsystems
Flat bottom immuno plate	VWR international
Transparent bottom immuno plate	VWR international

ELISA Background comparison
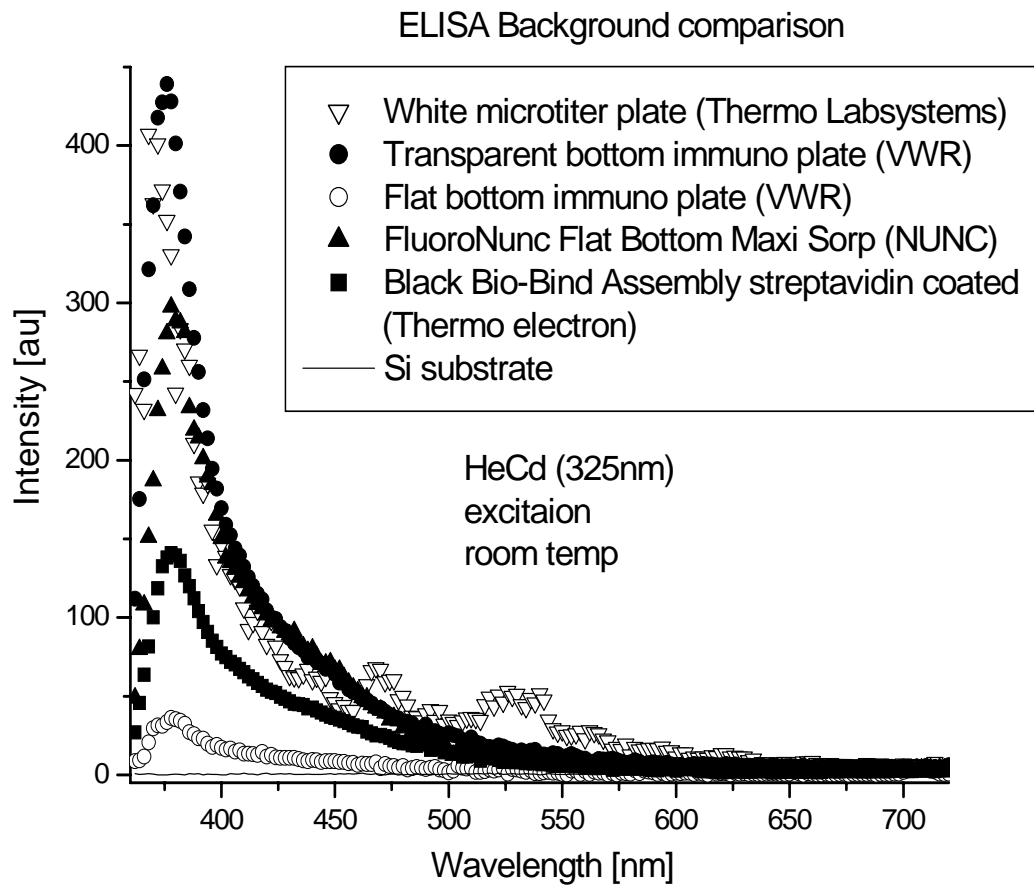
Figure 3.3 Background signal from different ELISA plates as a function of wavelength

The best substrates for PL measurements should not have any signal in the spectral range of interest; in our case this is almost all of the visible part of the spectrum from 400-750 nm. A bulk single crystal Si wafer with the band gap of 1.1 eV at room (1100 nm) is a suitable material for a substrate.

3.3. Spatially resolved PL spectroscopy experimental details

3.3.1. Hardware description

Various lasers were used as the excitation sources in the PL experiments. In Table 3.4 their specifications is presented:

Table 3.4 Lasers used in the PL experiments

Laser type	Emission wavelength	Output power	Manufacturer/Model
HeCd (cw)	325 nm	50 mW	Coherent Inc. HeCd series 74
Ar^+ (cw)	488 nm / 514 nm	50 - 100 mW / 50 - 100 mW	Coherent Inc. Innova 70
AlGaAs laser diode (pulsed)	804 nm (10 nm FWHM)	150 mW (in pulse)	Spectra Diode Labs SDL 800

The photoluminescence signal was dispersed with a 0.5 m SPEX-500M grating spectrometer possessing a reciprocal dispersion of 3.2 nm/mm (2nd order) with a 600 lines/mm diffraction grating. The dispersed signal was registered with either an air-cooled photomultiplier (Electron Tubes) in the spectral range of 400 - 800 nm or a liquid nitrogen cooled Ge detector (North Coast Scientific Corp.) in the range of 700 – 1700 nm. A mechanical chopper modulated the excitation light of the CW laser with 82 Hz frequency. AC signal from the detectors was fed to Lock-in amplifier EG&G Model 5209 and collected by a computer. A schematic of the PL setup for InAs QD measurement is shown on Figure 3.4
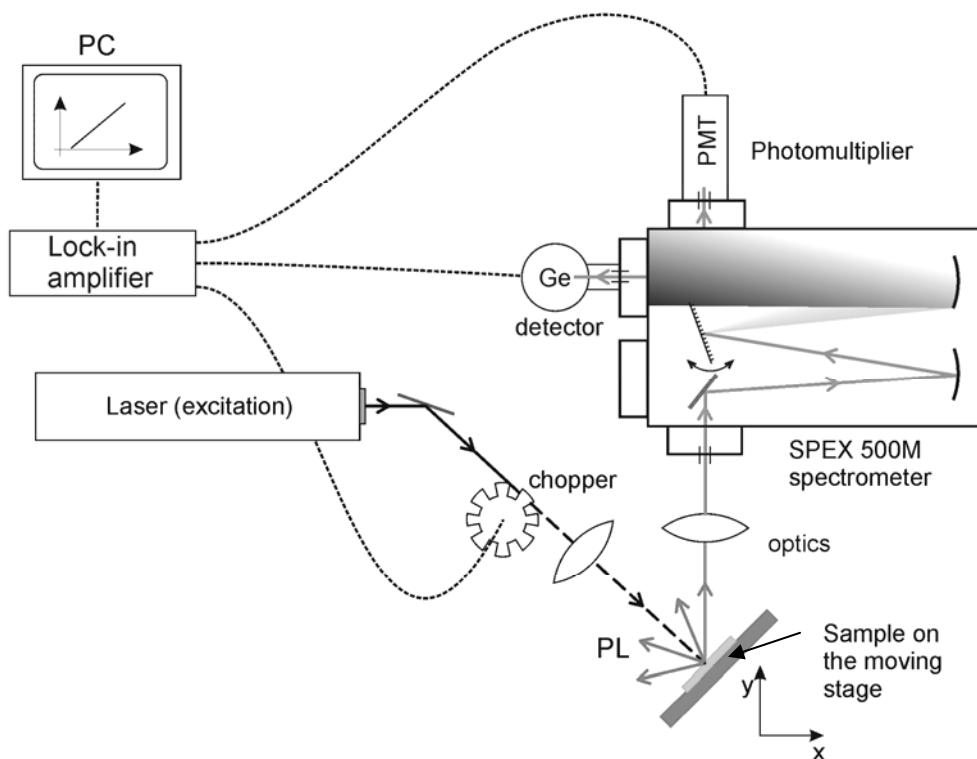
Figure 3.4 Photoluminescence setup for room temp measurements of InAs QD's

3.3.2. PL mapping measurements

The PL mapping experiment was done with the use of an X-Y computer controlled moving stage (Velmex 8300) with 10 μm step precision and (Klinger CC 1.2) for 1 μm resolution maps.

Liquid phase ELISA measurements were performed with the modified optics scheme as shown in figure 3.5. In this scheme the vertical optics alignment had to be used in order to keep the liquid in place. An additional mirror with a hole in the center for the excitation laser beam allowed for PL signal collection from horizontally placed ELISA plates.
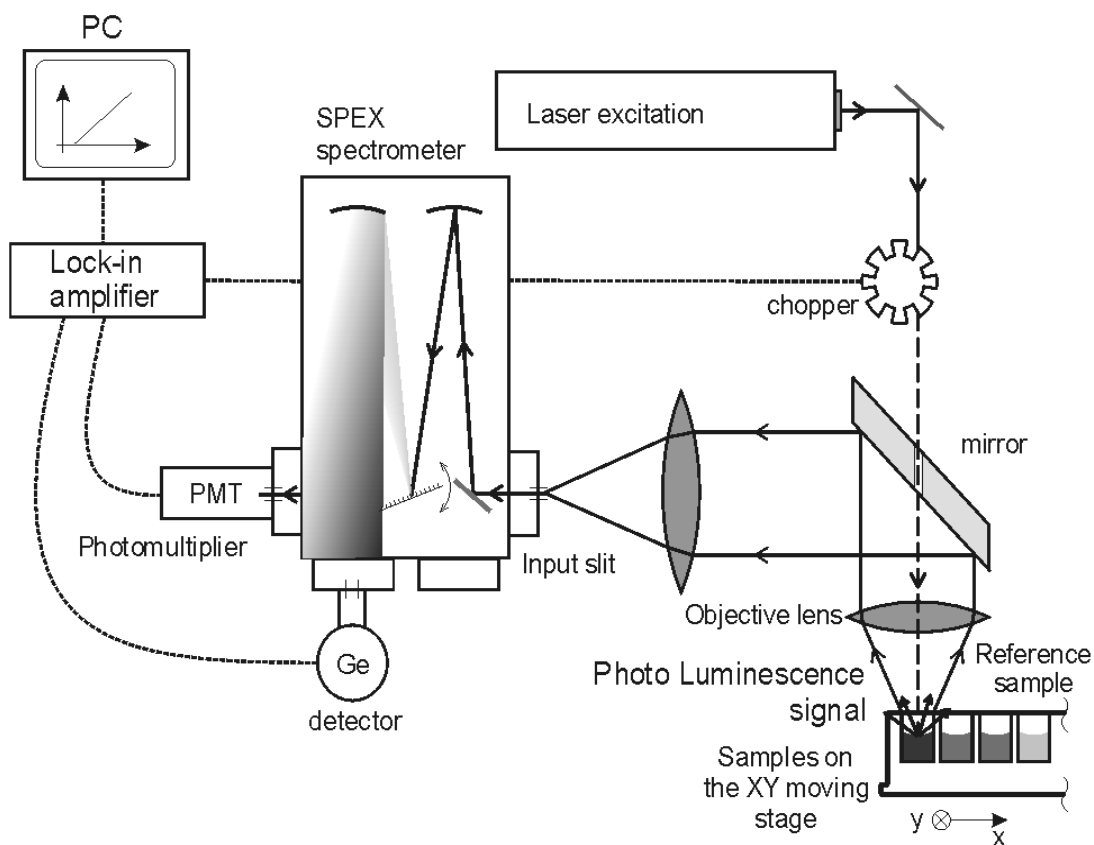
Figure 3.5 Photoluminescence setup for liquid ELISA experiments

Low temperature measurements were carried out in a closed cycle He cryostat (RMC cryosystems 22CB Cryogenics Inc.) allowing temperature variation from 10 to 350 K. The small dimensions of the cryostat head allowed for the low temperature mapping measurements with the experimental setup shown on Figure 3.6.
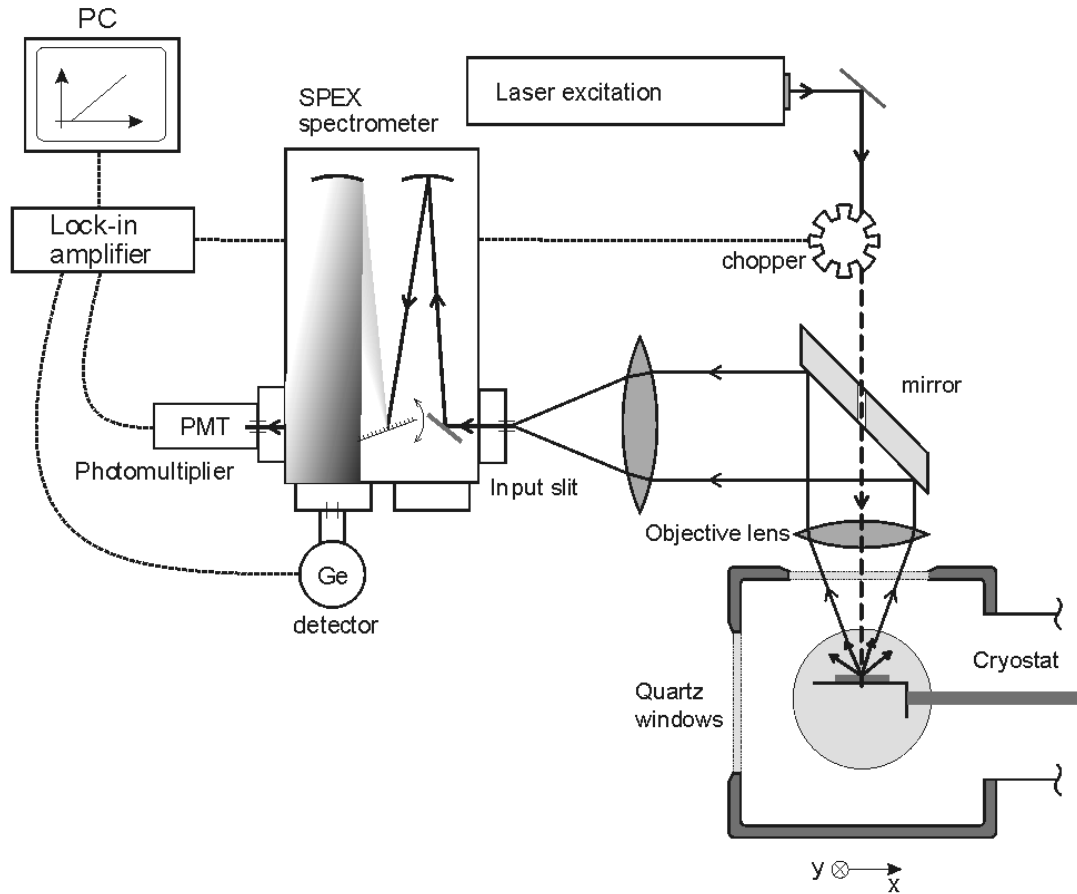
Figure 3.6 Photoluminescence setup for low temperature PL mapping

Mapping of the glass slides prepared with micro array technique was done with the use of our experimental setup and with the use of the optical confocal microscope (Nikon Eclipse 800) in parallel. Micro array spots were printed with a BioRobotics MicroGrid microarrayer from Genomic Solutions (Ann Arbor, MI).

3.4. Bio-conjugation confirmation techniques

To ensure that our quantum dots have been conjugated to biomolecules we employed two different techniques to detect bioconjugation occurrence. Use of these techniques allows us to detect the amount of a given biomarker via integrated PL intensity measurements. The well known intensity vs. concentration dependence for ELISA and micro array approach is shown in Fig 3.7. We utilized it in order to confirm that bioconjugation to QD's has taken place, if the overall QD PL signal follows it we may assume the bioconjugation was successful.
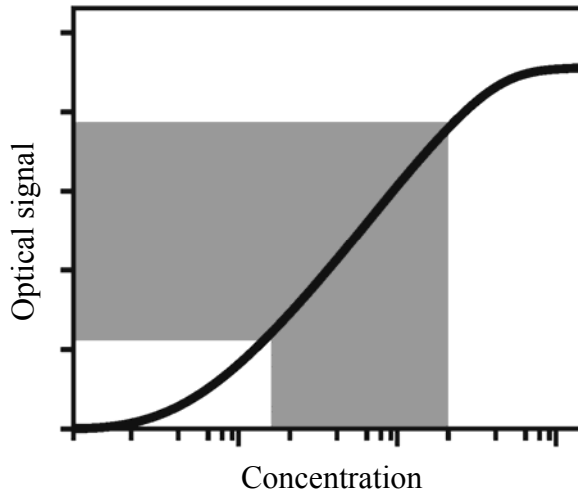
Figure 3.7 ELISA concentration curve vs. optical signal. Linear part (shaded area) constitutes the limits of detection for given biomarker concentration range

3.4.1. Enzyme Linked ImmunoSorbent Assay (ELISA) technique

The ELISA technique is used for the detection of a given biomolecule (antigen in our case) by means of the attachment of a specifically recognizing molecule that has been labeled with a fluorescent label. ELISA combines the specificity of antibodies with the sensitivity of simple enzyme assays, by using antibodies or antigens coupled to an enzyme or directly labeled secondary antibody.

Sandwich ELISA assays are one of the most useful immunoassays, this is a two-antibody "sandwich" (Fig 3.8) This assay is used to determine the antigen concentration in unknown samples [115]. The ELISA is a fast and accurate technique, and if the purified antigen standard is available, the assay can determine the absolute amount of antigen in an unknown sample. What we have utilized here is the Elisa method to validate our bioconjugation procedure.
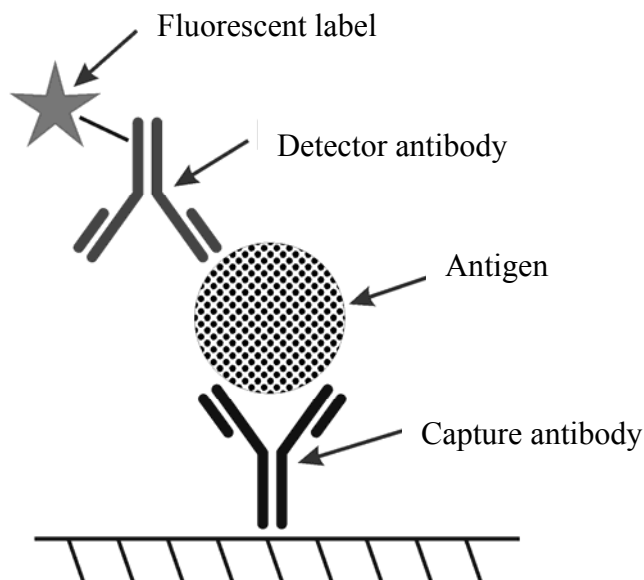
Figure 3.8 "Sandwich" immunoreaction scheme for the direct ELISA approach

The sandwich requires two antibodies that bind to epitopes (conjugation sites on the protein surface) that do not overlap on the antigen. This can be achieved with either two monoclonal antibodies (mAb antibodies are produced by one type of immune cell or it's clones) that recognize discrete sites or one batch of affinity-purified (different antibodies that recognize this specific antigen with 100% specificity) polyclonal antibodies [115].

To utilize this assay, one antibody (the "capture" antibody) is purified and bound to a solid phase typically attached to the bottom of the plate. Antigen is then added and allowed to complex with the bound antibody. Unbound products are then removed with a wash, and a labeled secondary antibody (the detection antibody) is allowed to bind to the antigen, completing the sandwich. The assay is then quantized by measuring the amount of the labeled secondary antibody bound to the matrix, either via optical density change or the fluorescence intensity of the attached label. Major advantages of this technique are that the antigen does not need to be purified prior to use, and that these assays are very specific. However, one disadvantage is that not all antibodies can be used. Monoclonal antibody combinations must be qualified as "matched pairs" meaning that they can recognize separate epitopes on the antigen so they do not hinder each other's binding.

Sandwich ELISA
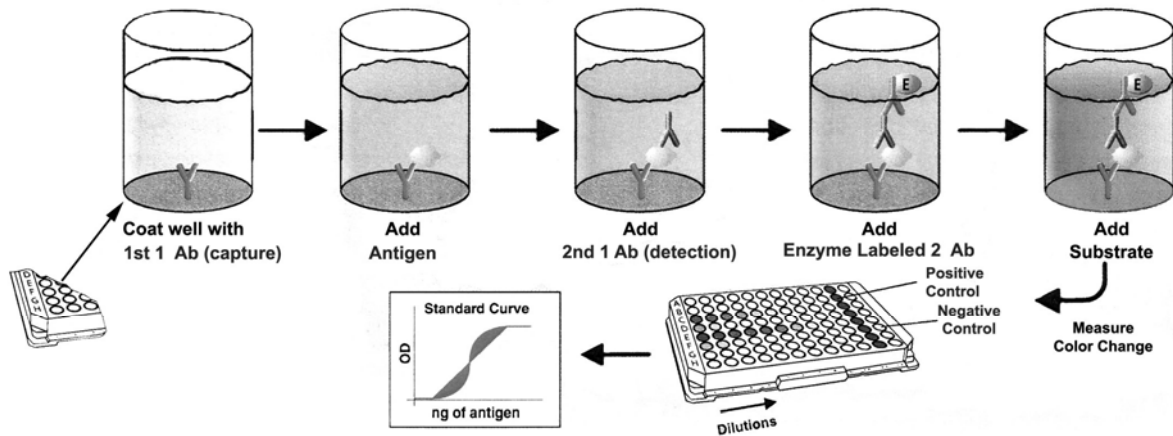
Figure 3.9 Direct sandwich ELISA procedure (after Chemicon.com) [116]

3.4.2. Protein microarray technique

Protein Microarray is the methodology to detect the existence of a given biomolecule with the use of the immunoreactions technique. In it's basic assumption it is similar to the ELISA technique although it is more advanced in this aspect with use of much less sample volume. The major difference is that the proteins are printed by a needle on the substrate surface instead of being deposited from the solution (Fig 3.10). The printed spots are usually 100 to 200 microns in diameter what utilizes very small amounts of sample and allows the printing of large spot numbers on relatively small areas. The reaction speed for smaller volumes is also faster and allows one to measure relatively smaller quantities of antibody than ELISA, though it requires much better scanning techniques. The following processing and wash steps are similar to the ELISA procedure shown in Fig. 3.9.
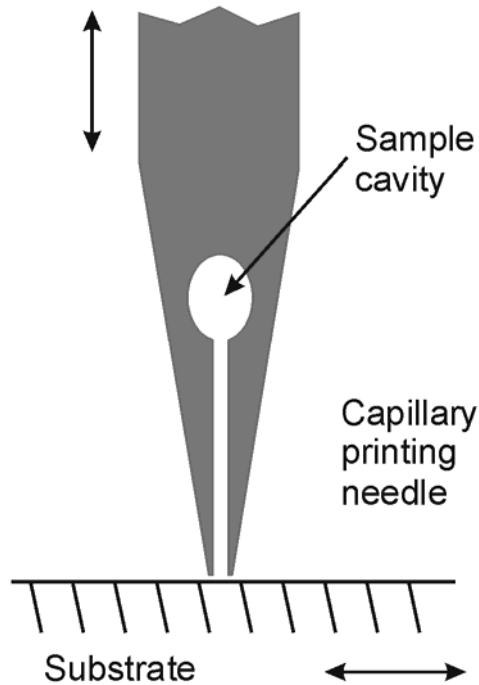
Figure 3.10 Printing scheme in the micro array technique

Mark Schena [117] - author of the first paper demonstrating the usefulness of protein microarrays, describes them as analytical devices that possess four distinct characteristics: (a) microscopic target elements or spots, (b) planar substrates, (c) rows and columns of elements and (d) specific binding between microarray target elements on the substrate and probe molecules in the solution [117]. It is a miniaturized assay (spots are usually in the range 0.1 – 0.5 mm in diameter) [117] where each spot contains "bait" molecules (antibody in protein / antibody microarrays), which are probed with an unknown biological sample containing analytes of interest [118]. By processing the microarrays with a detector antibody tagged with a fluorescent label, each spot produces a fluorescent signal proportional to the analyte of interest present in the solution and the captured/bound to the "bait" molecule [118].

Applications of functional protein microarrays include: expression profiling for identification and quantitation of proteins present in the solution; protein-protein interactions for examination of the binding activity and binding partners of proteins across the entire proteome; drugs for identification of drug activity, targets, cross-reactivity, and diagnostics to measure proteins expressed in serum samples [117].
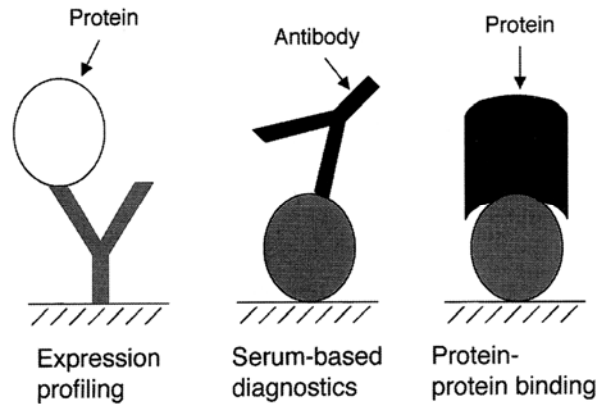
Figure 3.11   Basic microarrays immuno reactions after Schena [117]

Production and use of microarrays consists of the following steps: printing and immobilization of capture antibodies on a functionalized surface (usually glass slide covered with poly-L-lysine, aldehyde, epoxy or nictrocellulose) [119]; incubation with the sample, detection with fluorescent probe – QD in our case, image capture and analysis. The most sensitive method for protein microarrays processing is the "sandwich assay" (Figure 3.8) based on the Elisa technique. It utilizes two antibodies that simultaneously bind to the same antigen. One of them called "capture antibody" is responsible for immobilization of antigen onto the slide surface. The other one called "detector antibody" which is fluorescently labeled, is attaching to already immobilized

antigen from the other side producing a fluorescent signal. Averaged intensity of the fluorescent signal is the representation of biomarker concentration in the solution.

Protein expression profiling, protein-protein binding, drug interactions, protein folding, substrate specificity, enzymatic activity, and the interactions between proteins and nucleic acids are among the many applications of protein microarrays.

For bio conjugation confirmation the protein-protein interaction was of our interest. Having quantum dots conjugated to a detector antibody we are able to check this linkage by their immobilization through a "sandwich" reaction on the substrate surface and scanning for a luminescence signal.

3.5.   Summary

Samples of InAs quantum dots were prepared using MBE technique. Measurements mostly reflect a non uniformity of this process. This allowed us to investigate hard to control growth parameters such as a planar QD size distribution. Study of QD size influence on the optical properties was done along with other growth parameters that were changed on purpose like growth temperature. All of these samples represent multi-quantum well structures with very strong carrier confinement in the QD layer itself – there are no signs of the surrounding quantum wells even for very high excitation intensities. Indirectly this may suggest that our samples are of very high QD quality with deep enough QD potential for room temp laser applications.

CdSe quantum dots for biological applications were purchased from commercially available sources; hence in depth details of their creation parameters are

not known, manufacturers assure the 5% distribution size among one QD species but not all of the purchased QD material actually showed repeatable PL results, especially for different batches of the same product. Bio – conjugation techniques allowed for indirect determination of bio-molecule attachment and further spectroscopic investigations of conjugated vs. non-conjugated QD's. For repeatability reasons we decided to perform bioconjugation ourselves without purchasing already pre-conjugated QD's for which we did not have a pure reference QD sample. All wet samples experienced substantial scattering, and as a direct consequence, we started to work with the dried residues of the ELISA procedures. Since ELISA is very dependent on the washing procedures and initial well functionalization, the human factor played a huge role in sample preparation. Use of the microarray printer with the automated printing procedure was the next step in order to increase the sample quality. For the characteristic spectral features of biomolecule attachment we used drops of dried conjugate samples on a Si substrate for better background separation. The "strength" of the conjugation was investigated with the use of all the fractions from conjugation experiments and appropriate sample collection during each step of this procedure.

4. Results and Discussion

4.1. PL spectroscopy of InAs/InGaAs quantum dots for laser applications

PL spectroscopy of InAs Quantum dots was carried out on two sets of samples. The initial one that contained small pieces of full size wafers approximately 1x2 cm in size that showed already some spatial inhomogeneity and the full set of whole 50mm diameter wafers for larger area scans. Spectroscopic mapping was carried out to investigate the influence of growth temperature as well the cladding layer composition for the two subsets of samples respectively.

4.1.1. Growth temperature investigations - PL spectroscopy

The temperature of the substrate during QD growth was varied in the range of 470 up to 535ºC. For QD's grown at 470ºC only one PL band was observed with a higher value of full width at half maximum (FWHM) of 50-60 meV at 80 K (Fig. 4.1 b) with respect to higher temp samples. With an increase of the QD growth temperature the integrated PL intensity of the investigated structures increased and the PL spectrum changed (Fig. 4.1 to 4.5).
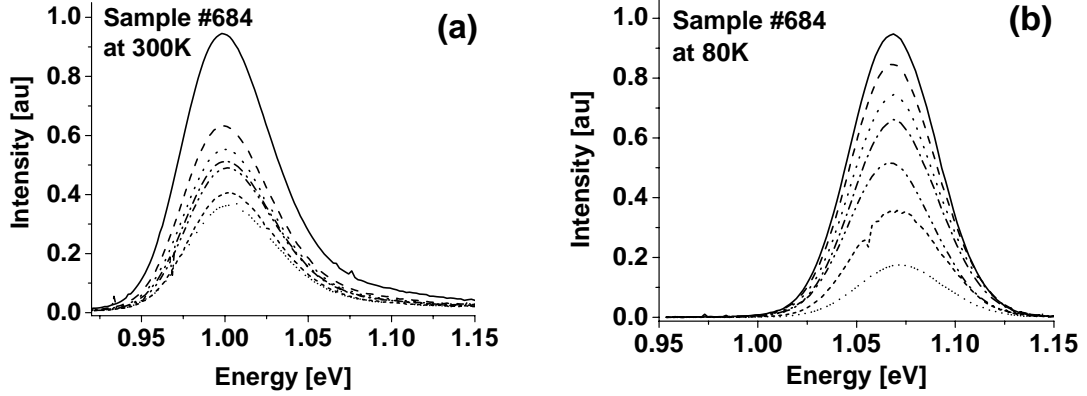
Figure 4.1   PL spectra of QD structure #684 (grown at 470°C) at various intensity

points (from lowest to highest) measured at 300 K (a) and 80 K (b)
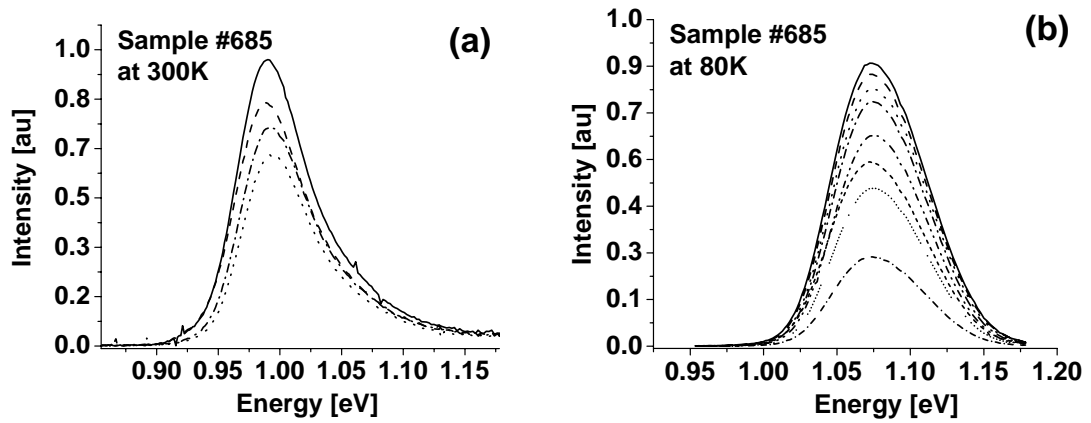
Figure 4.2   PL spectra of QD structure #685 (grown at 490°C) at various intensity

points measured at 300 K (a) and 80 K (b)
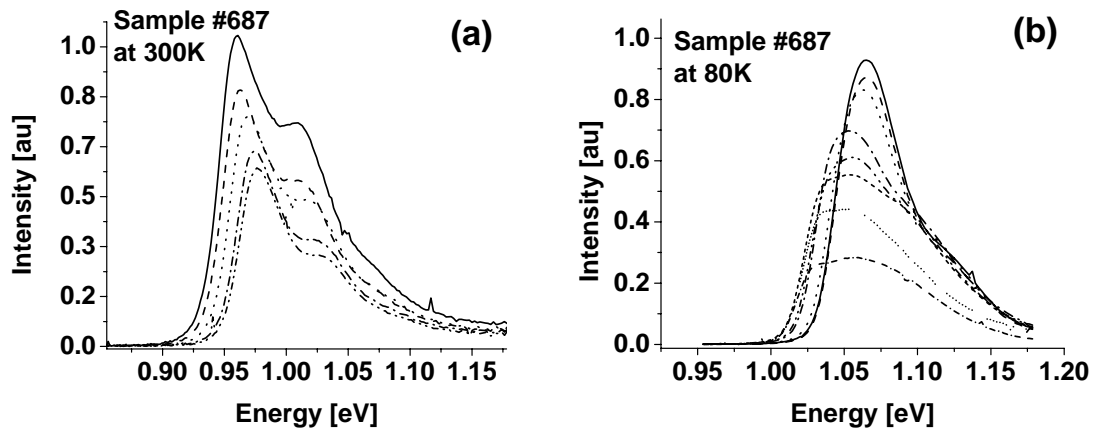
Figure 4.3 PL spectra of QD structure #687 (grown at 510°C) at various intensity points

measured at 300 K (a) and 80 K (b)
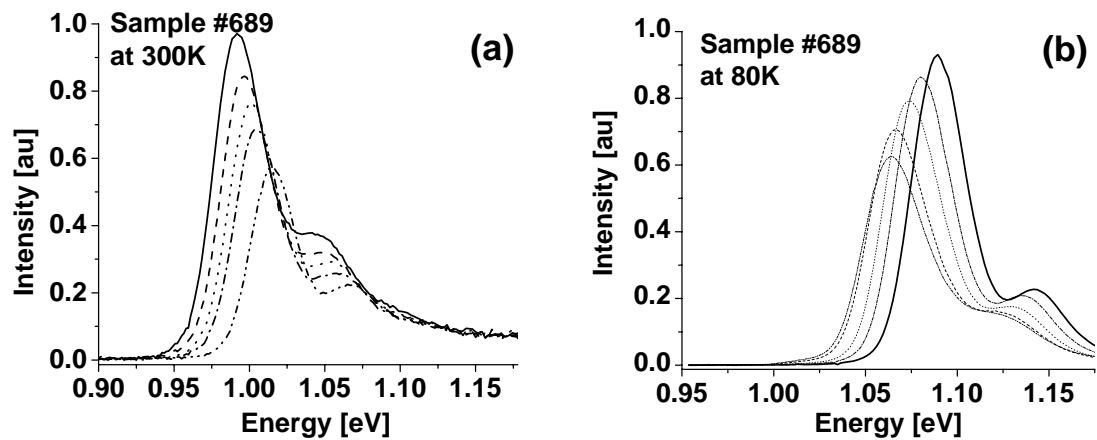
Figure 4.4 PL spectra of QD structure #689 (grown at 525°C) at various intensity points

measured at 300 K (a) and 80 K (b)
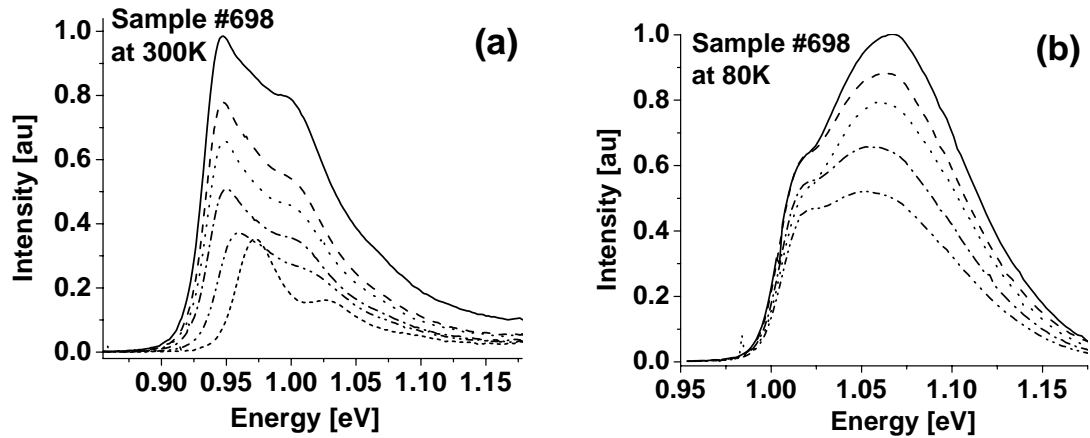
Figure 4.5 PL spectra of QD structure #698 (grown at 535°C) at various intensity points

measured at 300 K (a) and 80 K (b)

The variation of PL band intensities versus excitation laser power density presented in Figure 4.6 indicates that the low energy PL band can be attributed to the carrier recombination between ground states (GS) and the higher energy PL band and appears at an excitation density > 50 W/cm^2, indicating that it is an optical transition via the first-excited state (1ES) in the QDs. The FWHM of the GS band for the two band PL spectra is 35-38 meV at 80 K that is typical for high quality InAs QD structures [36]. PL spectra measured at different excitation power densities at 77 K are presented in Fig. 4.6 for the QD structure #689 with the QD layer grown at 525 °C. Up to 3 consecutive excited state PL transitions are observed at the highest excitation laser power density.
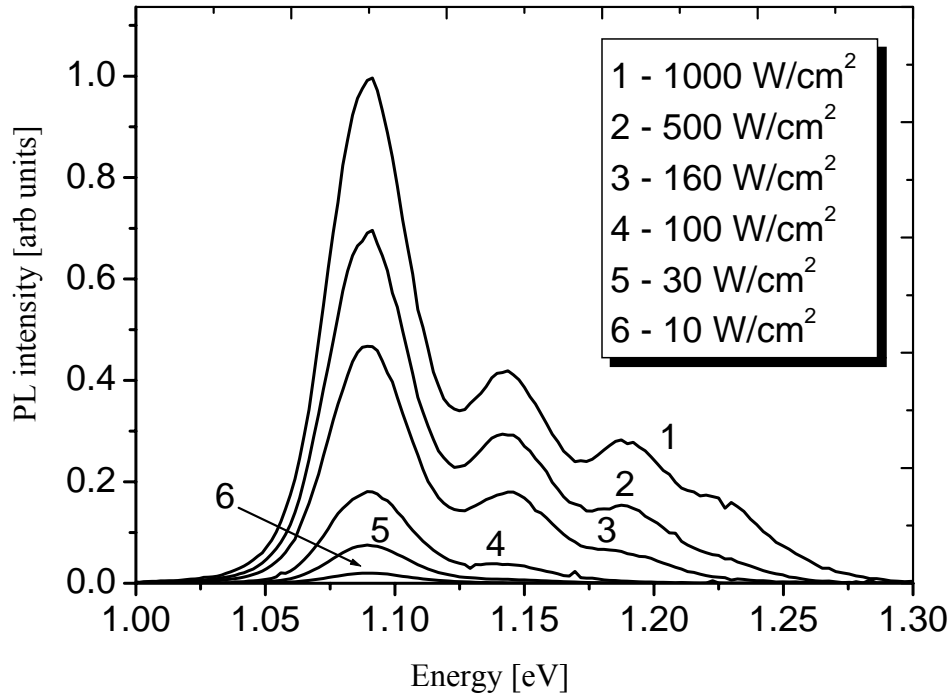
Figure 4.6 PL spectra of the QD ensemble measured at different excitation powers with
the highest power density of 1.0 kW/cm^2 (Structure #689 measured at 77K)

This structure exhibited the highest PL intensity at 12 K temperature and an excellent resolution of the ground and excited PL bands. The spectra reveal a set of PL bands with peak energies of 1.110, 1.160, 1.207, 1.249, and 1.281 eV as can be typically observed on a QD ensemble having a good homogeneity [39, 120]. Three former PL bands are well resolved and are close to Gaussian in shape. The variation of PL band intensities versus excitation power indicates that the low-energy PL band can be attributed to the ground state (GS) of the QD's. The higher-energy PL bands appear at an excitation power density exceeding 100 W/cm^2, indicating the optical transitions are via the excited states (1ES-4ES). The deconvolution procedure using Gaussian bands was

applied to these spectra, which has shown that the half width of the three lowest energy

PL bands (GS, 1ES, and 2ES) are equal to 39, 31, and 28 meV, respectively. The energy

separation between GS and ES bands is not equidistant and equal to 50, 47, 42, and 32

meV, which indicate that the studied QDs could not be characterized by a harmonic

oscillator potential [121]. Ground state PL intensity dependence versus temperature for

the QD ensemble presented in Fig. 4.7 has been measured for an excitation power density

of 650 W/cm^2 for the structure #689 as well.
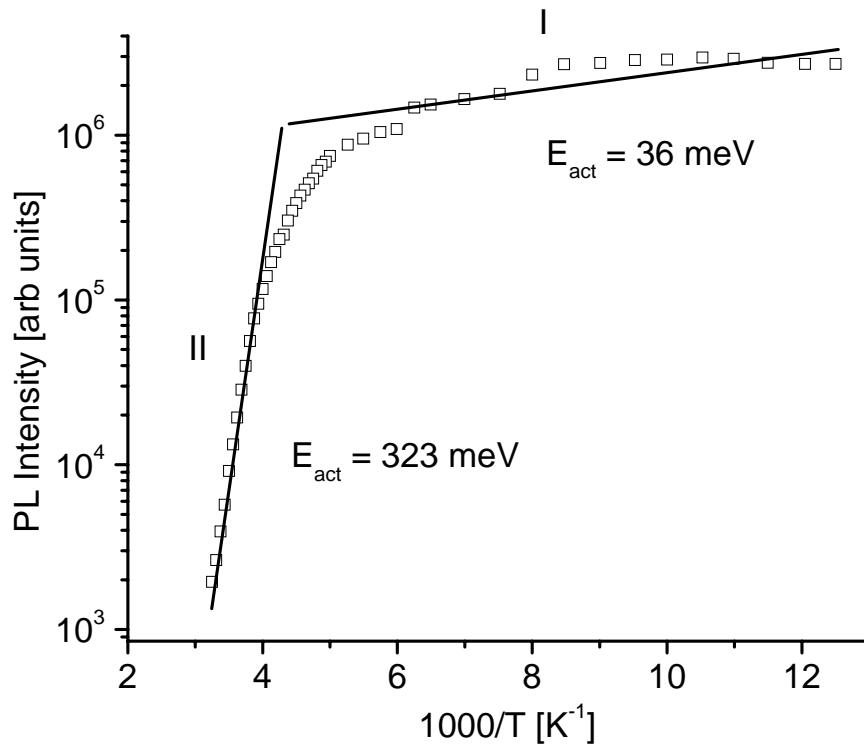
Figure 4.7 Ground state PL band intensity dependence vs. temperature (Excitation power
density 650 W/cm^2) (Structure #689). Two distinct regions were observed,
labeled I and II, indicating two different activation energies

Two different slopes (labeled as I and II in Fig 4.7) of PL intensity dependence are clearly seen on the temperature curve: (I) the first slope is in the low-temperature range 80–250 K before the main thermal quenching process (II) starts. The activation energies of these processes were estimated by analyzing the temperature dependence of the PL intensity using the Arrhenius plot (Fig. 4.7). The estimated activation energies are 36 (I) and 323 (II) meV. In this case, we can interpret the PL intensity thermal quenching of the first (I) slope as the carrier thermal escape processes from the QD levels. Taking into account that QDs in this experiment are excited by the light with energy quanta of 2.41 eV, which are effectively absorbed in GaAs and wetting layers, the small activation energy of 36 meV can also be associated with thermal carrier escape from wetting layers to the GaAs layer where it is possible for them to recombine via nonradiative channels. The second 323 meV thermal activation energy is larger than the electron-hole binding energy in this type of QD, which typically ranges from 100 to 150 meV [112, 113]. Thus, we attribute this high thermal activation energy of 323 meV to the activation of nonradiative recombination centers.

4.1.2. Growth temperature investigations - PL mapping

PL mapping at the GS state energy was also performed for this sample. The PL intensity in the QD samples was measured at 80 and 300 K and shows long-range inhomogeneity across the wafer area, which is accompanied by a spectral shift of the PL maximum. We explored this effect in more detail using the spectroscopic PL mapping technique where the PL spectrum is recorded and analyzed at each sample point.
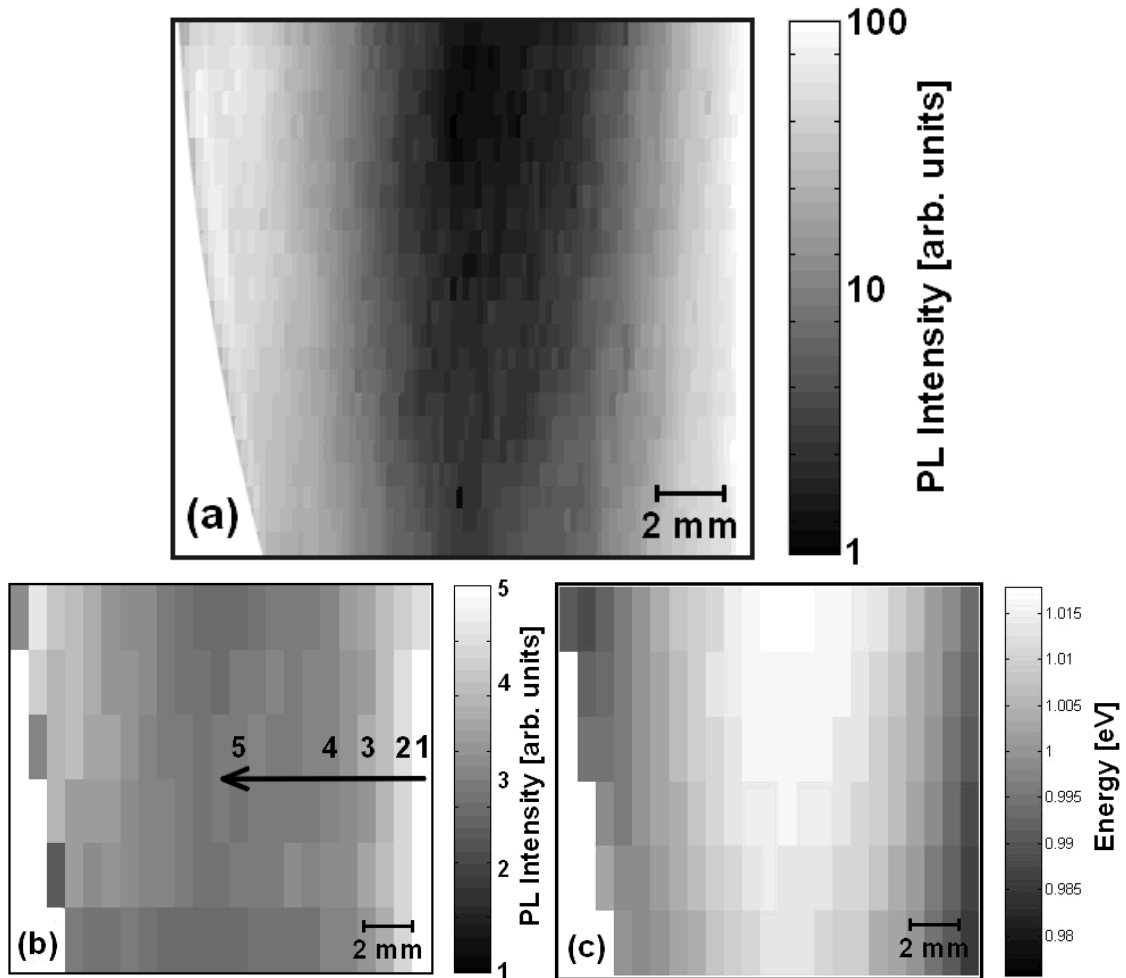
Figure 4.8 (a) Map of PL intensity at 0.99 eV (0.25 mm step size, 200 μm excitation spot
diameter), (b) map PL intensity at GS max position, and (c) map of peak
energy positions (0.5 mm step size) at ~90 W/cm^2 power density. Arrow in (b)
corresponds to spectroscopic line scans presented in Figure 4.9

In Figure 4.8 (a) the room-temperature PL map measured on QD structure #689 at

energy of 0.99 eV close to the principal PL maximum is shown. Notice the logarithmic

scale specified in the contrast bar of Fig. 4.8(a). Two orders of magnitude variation in the

PL intensity signal was observed. This can be seen from the low PL intensity in the

central part of the structure to the high PL intensity at the sample periphery area. To

establish the origin of such a strong PL inhomogeneity, spectroscopic PL mapping

measurements were performed. At first the ground state PL scanning spectra were measured at 300 K in high- and low-intensity areas of the QD structure. Low-intensity regions at 300 K are characterized by the "blue" shift of the PL spectrum compared to high intensity areas, as shown in Figure 4.9(b).
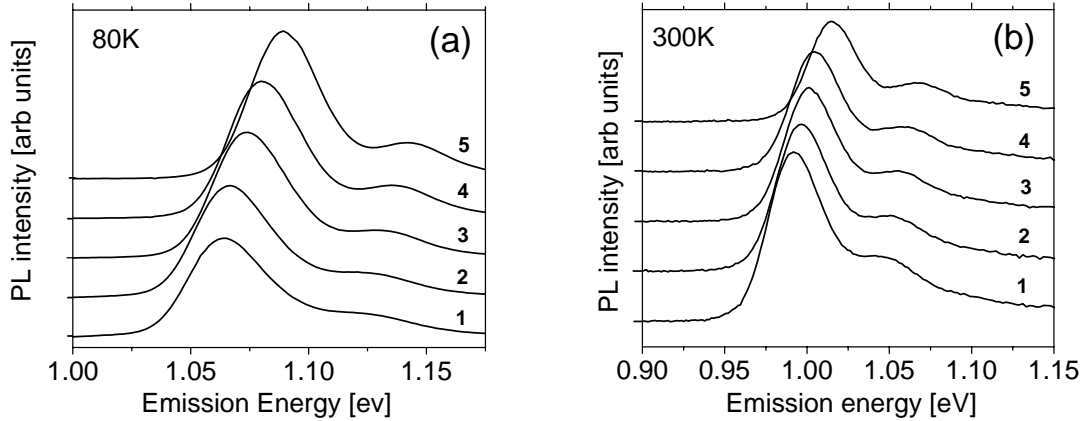
Figure 4.9   PL spectra measured at 80K (a) and 300K (b) at various PL intensity points on the QD structure #689, (see Fig. 4.8(b)). (~90 W/cm^2 power intensity)

The PL peak position shifted from 0.98 up to 1.02 eV with a threefold decrease in PL intensity. Maps of the maximum positions and PL intensities at these maxima were plotted from measured spectra in Figs. 4.8(b) and 4.8(c). In correlation with previously described spectral behavior, low-intensity points (dark areas in Fig. 4.8(b)) are characterized by a higher energy position of the principal maximum (white areas in Fig. 4.8(c)). We observe a clear correlation between PL intensity and PL maximum measured across entire sample areas on four different QD structures #685, #687, #689 and #698 (Fig. 4.10).
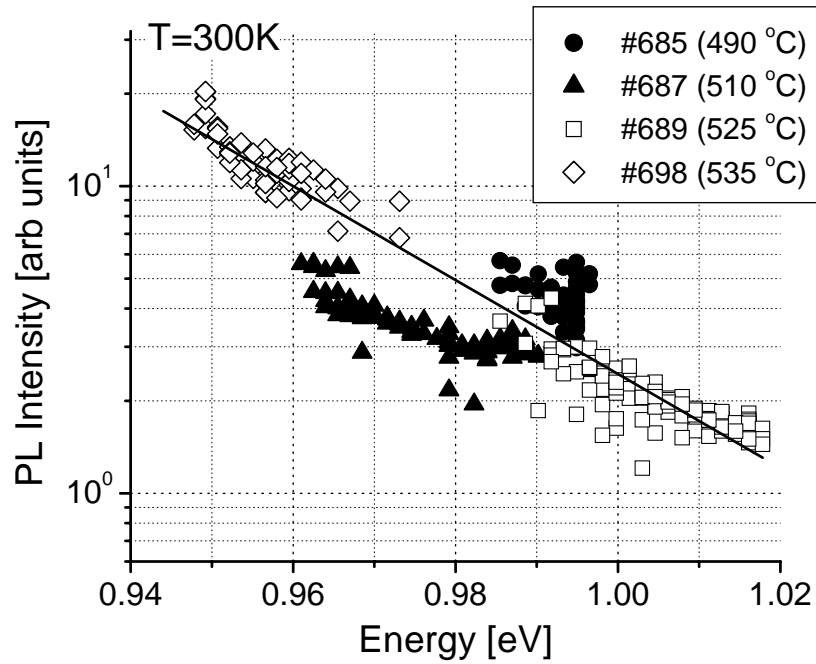
Figure 4.10 Ground state PL intensity vs. GS maximum position measured at room temperature and 90 W/cm^2 power intensity on QD structures grown at different temperatures

Spectroscopic PL mapping was performed across the entire sample's area. In the semi-logarithmic plot of the ground state PL intensity versus GS energy position, this trend can be fitted with a linear dependence as presented in Fig. 4.10 Scanning PL study at 80K was performed and compared with room-temperature data along the same line scans. The GS PL peak position shifts at 80K to the higher energy by 100 meV due to a band-gap energy increase. Concurrently, a trend of the PL maximum versus PL intensity at 80 K is inverted compared to the room-temperature data, i.e., higher intensities correspond to higher PL energy peaks (Fig. 4.9(a)).

PL mapping of the ground state and multiple excited states was performed at 80 K at the excitation power density of 650 W/cm^2. For PL spectra measured at high excitation, the three lowest energy PL bands (GS, 1ES, 2ES) were well resolved, which allows us to perform spatially resolved mapping of their peak positions across the sample. Figure 4.11 presents the variation of GS, 1ES, and 2ES energies versus corresponding GS maximum.
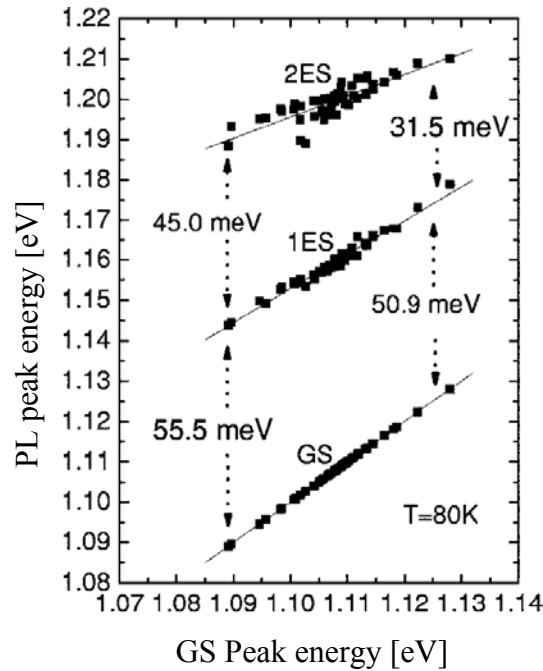
Figure 4.11 Experimental peak positions for the GS, first, and second ES vs. GS peak energy measured at 80 K and excitation power intensity of 650 W/cm^2

The energy separations vary across the sample. These separations are 55.5 (GS-1ES) and 45.0 (2ES-1ES) meV for the low energy GS optical transition at 1.090 eV and it decreases monotonically to 50.9 (GS-1ES) and 31.5 (2ES-1ES) meV for the high-energy GS optical transition at 1.129 eV.

The long-range GS PL intensity variation across the QD structure, which is accompanied by the PL peak shift at 300K (Figs. 4.8, 4.9(b), and 4.10), is presented. In our cladding layer investigations (see Section 4.1.2) it's shown that there are two mechanisms exhibiting PL intensity spatial variation in the InAs QD structures. The first is attributed to inhomogeneous distribution of non radiative (NR) defects across the QD structures. In this case, scanning PL intensity variation was not accompanied by a PL spectral shift. The second mechanism is related to QD parameter changes along the area of high quality QDs. In the last case, the PL intensity variation is accompanied by a shift of the PL maximum. Our results show that in the investigated InAs QD structures the second mechanism of PL inhomogeneity along the structure area is present.

The ground state PL intensity (I_{PL}) is directly proportional to the excitation light power density and the internal quantum efficiency, η, which can be presented as $\eta = \varpi_R / (\varpi_R + \varpi_{NR})$, where ϖ_R and ϖ_{NR} are radiative recombination (R) and non-radiative recombination (NR) rates, respectively. From the GS PL temperature dependence (Fig. 4.7) it follows that $\varpi_R \ll \varpi_{NR}$ at 300 K due to thermal quenching of the GS radiative recombination. In this case, the value η can be substituted by the following: $\eta = \varpi_R / \varpi_{NR}$. For a QD ensemble the emission rate is given as:

$$\varpi_R = \sum_{i=1}^{N_D} \left(\frac{f_i^e f_i^p}{\tau_R} \right) \tag{10}$$

where f_i^e and f_i^p are the occupation probabilities for electrons and holes at ground state levels given by the Fermi-Dirac distribution functions:

$$f^e, f^p = \left\{ \exp\left[\left(E_{n,p} - \mu_{n,p} \right) / kT \right] + 1 \right\}^{-1} \tag{11}$$

where $\mu_{n,p}$ are the quasi-Fermi-levels for the conduction and valence bands, respectively, measured from the QD band edges, $E_{n,p}$ are the quantized energy levels of an electron and a hole in the conduction and valence bands of the QD, measured from the QD band edges, N_D is QD density, and τ_R is the electron-hole radiative recombination time [122]. At low excitation light intensity (90 W/cm^2), used during GS PL scanning, which is well below the GS saturation intensity, we can present the occupation probabilities using Maxwell-Boltzmann distribution functions

$$f^e, f^p = \exp\left[\left(- E_{n,p} + \mu_{n,p}\right)/ kT\right] \tag{12}$$

Taking into account that excitation light power is not changed during the GS PL scanning experiment, we can assume that $\mu_{n,p}$ are constant along the scanning line and the PL intensity variation occurs due to parameters the $E_{n,p}$ only. In this case, $f_e \approx \exp(-E_n/kT)$ and $f_p \approx \exp(-E_p/kT)$. The energy levels $E_{n,p}$ can be presented as $E_n = \Delta E_c - E_{loc}^e$ and $E_p = \Delta E_v - E_{loc}^p$, where $\Delta E_{c,v}$ are the conduction and valence-band offsets at the QD-narrow-gap region heteroboundary, measured from the QD band edges, and E_{loc}^e and E_{loc}^p are the binding energies of the electron and hole located at the GS levels. We assumed that the values of $\Delta E_{c,v}$ and the QD density, N_D, do not change significantly along the PL scanning line and as a result the variation of $f_{e,p}$ in the PL scanning experiment can be presented as $f_e \approx \exp(-E_{loc}^e/kT)$ and $f_p \approx \exp(-E_{loc}^p/kT)$. In this case, the GS radiative emission rate is changing along the PL scanning line at room temperature as follows:

$$\varpi_R \approx \exp\left(\frac{E_{loc}^e + E_{loc}^p}{kT}\right) \approx \exp\left(\frac{E_{GS}^{InGaAs} - E_{GS}^{QD}}{kT}\right) \approx \exp\frac{- E_{GS}^{QD}}{kT} \approx \exp\frac{-\left(h\nu_{max}^{GS} + E_{bin}^{ex}\right)}{kT} \tag{13}$$

where E_{GS}^{InGaAs} is the energy gap between the GS electron-hole levels in the narrow-gap In$_{0.15}$Ga$_{0.85}$As layer and E_{GS}^{QD} is the energy gap for the GS electron-hole levels in the QD. Here we are taking into account that the GS optical transition energy ($h\nu_{max}^{GS}$) is the difference between E_{GS}^{QD} and the exciton binding energy E_{bin}^{ex} in the QDs. Exciton binding energies were computed as a function of QD size using the eight-band k·p approach and are estimated as 19.5 and 22.5 meV for QDs with a base size of 16 and 13.4 nm, respectively [123]. Thus E_{bin}^{ex} value changes ($\Delta E_{bin}^{ex} \approx 2$ meV) versus QD parameters are small in comparison with GS optical transition energy variation ($h\nu_{max}^{GS} \approx 1.09$–1.25 eV) (Fig. 4.11). Finally, we could obtain scanning PL intensity variation at room temperature very close to the dependence I$_{PL} \approx \exp(-h\nu_{max}^{GS}/kT)$, as is demonstrated by the fitting line in Fig. 4.10.

The long-range variation of QD electron and hole localization (binding) energies across the sample area in general can be attributed to the following:

- QD size changes as a result of inhomogeneous temperature fields across the wafer or InAs layer thickness inhomogeneity during QD growth,

- elastic stress variation across the sample due to layer composition variation

We suppose that the decrease of GS electron-hole binding energies across the scanning area is the result of the long-range variation of an average dot size in the QD ensemble from the periphery toward the sample center. This is exhibited as the "blue" shift of the PL maximum at 300 K (Fig. 4.9(b)). This effect leads, at the sample center, to shallower QD localized states (i.e., smallest electron and hole binding energies) and a

higher probability of the carrier thermal escape, which reduces their room-temperature PL intensity. To confirm our assumption and to study this effect in more detail, we performed scanning luminescence at 80 K along the same line scans as for 300 K. For the low temperature PL scanning measurement, we avoid carrier thermal escape process from the QDs. As we mentioned above, a trend of the PL maximum versus PL intensity at 80 K is inverted compared to the room-temperature data. The two-fold rise of PL intensity corresponds to a shift of the PL peak to higher energies from 1.05 up to 1.09 eV (Fig. 4.9(a)).

4.1.3. Cladding layer composition investigation - experimental results

The cladding layer composition study was performed for four different concentrations of In in the $In_xGa_{1-x}As$ layer. In Fig. 4.12 are shown two maps of the PL intensity measured on samples 1360 (x=0.15) and 1361 (x=0.1) at the energy of the principle PL maxima, 1.020 and 1.044 eV, respectively. White contrast on the maps represents higher PL intensity. Besides individual dark regions, which were caused by the sample holders in the MBE system, we observe on both samples a gradual up to five fold reduction of the PL intensity from the wafer center toward the periphery. These samples were parts of larger 50 mm diameter wafers.
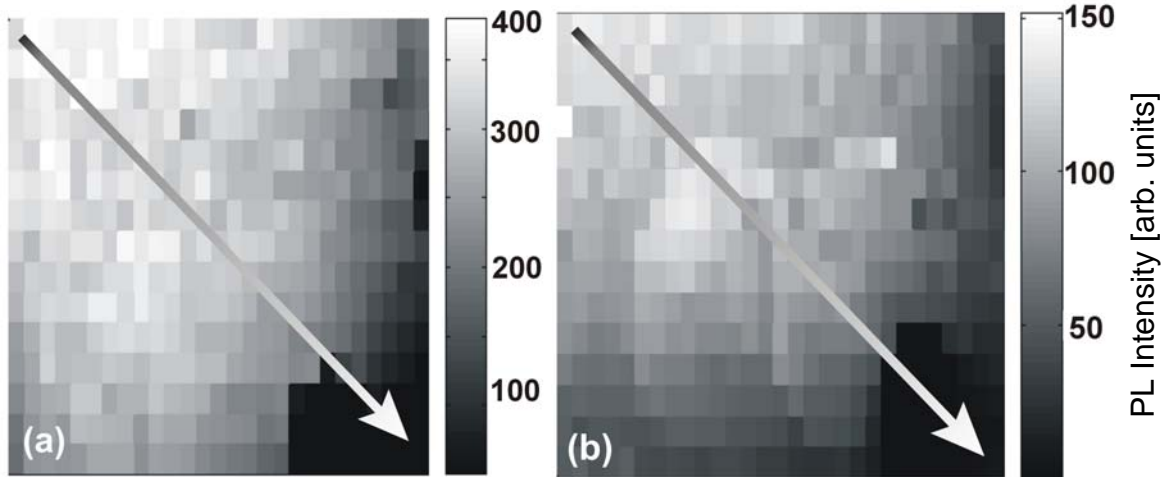
Figure 4.12 PL intensity mapping at room temperature performed at 1.02 eV on sample #1360 (a) and at 1.044 eV on sample #1361 (b) Shading bars represent the PL intensity variation in both samples. Arrows indicate orientation of the maximum PL intensity gradient from the water center to the periphery

Arrows drawn on the maps exhibit line-scans of the data points with the most significant PL variation, where the following spectroscopic and temperature study was performed.

In Figure 4.13 room-temperature PL spectra are presented measured along these line-scans in both samples, which show quite different features. Specifically, in sample #1360 a principal PL maximum maintains the spectral position at 1.020 eV within the band of 10 meV, while reducing the PL intensity by more than a factor of two. In contrast, sample 1361 exhibits a gradual "blue" energy shift of the maximum starting at the wafer's center at 1.044 eV and approaching 1.110 eV at the periphery, which matches a threefold degradation of the PL intensity. These observations are statistically confirmed

by measuring the PL spectra across the entire sample area as illustrated in Figure 4.14 for a set of 115 data points measured in the scanning mode.
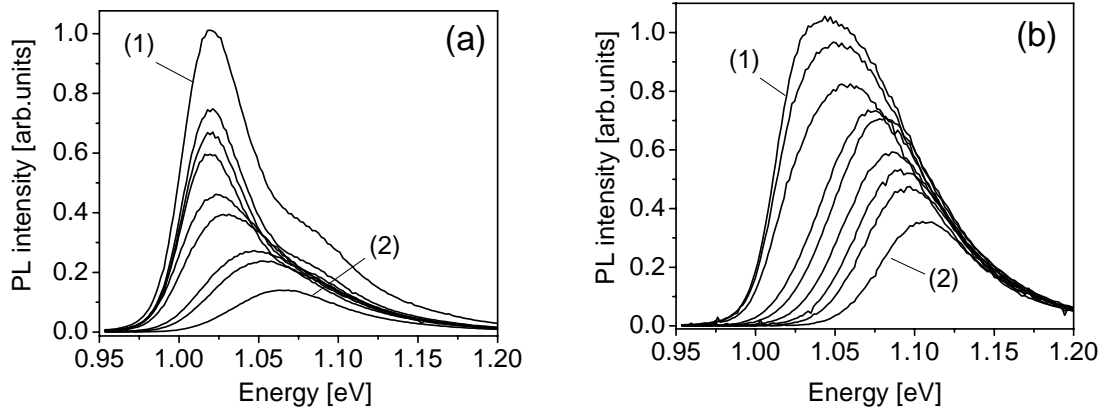
Figure 4.13 PL spectra at room temperature measured at different spots along the arrows in Fig. 4.12 on samples 1360 (a) and 1361 (b). Curve (1) corresponds to the central area of the samples; curve (2) corresponds to the periphery

It was noticed that the luminescence in sample #1360 has, at room temperature, the highest intensity averaged across the wafer compared to samples 1361 and 1363; 3.2 times and 1.2 times, respectively. Sample #1360 shows also the narrowest half width of the PL maximum of 37–42 meV (Fig. 4.13) compared to 73–79 in #1361. It exhibits an additional peak at 1.08 eV, which was previously observed on high-quality QD samples and attributed to the luminescence through the excited states of the holes in QD [112, 113]. These facts indicate that the electronic quality of the QD structure is superior in sample #1360 with an x=0.15 composition of the cap layer. It is worth noticing that sample #1360 also partially shows features of sample #1361 at the low PL intensity periphery region. This is illustrated in Fig. 4.14 as data points with a "blue" shift of the maximum accompanied by PL degradation. These data points in both samples have

identical slope in the PL maximum versus PL intensity dependence (see the dashed lines in Figure 4.14).
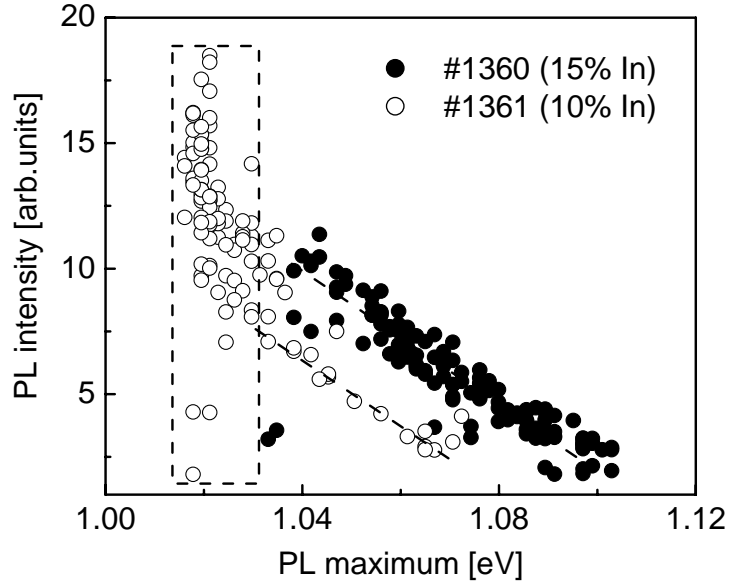
Figure 4.14 PL intensity vs. PL maximum dependencies measured at room temperature

on 155 points across the entire wafer as shown in Fig. 4.12

We can interpret the spectroscopic PL mapping results on the InAs/InGsAs QDs grown with different composition of the cap InGaAs layer, as two separate physical mechanisms realized in various samples. In sample #1361, the size of the dots decreases gradually from the center of the wafer toward the sample periphery. This is exhibited as a "blue" shift of the PL maximum. This effect leads at the wafer periphery to shallower QD localized states (i.e., smallest electron and hole binding energy), poorer carrier localization and, as a consequence, a higher probability of carrier thermal ionization, which reduces their room-temperature PL intensity. It is possible also, that in the smaller quantum dots, carrier wave functions penetrate more into the barriers surrounding the dot

and overlap more with nonradiative point defects. In this case, the intensity of the PL for small QDs should decrease faster with increasing temperature. Regarding sample #1360, the maximum position of the 1.02 eV PL band is maintained, and the drop of the PL intensity can be related to an inhomogeneous distribution of nonradiative centers, competing with QD luminescent transitions. We notice again that the first mechanism is also evident in this sample in areas with low PL intensity. To confirm and explore each of the mechanisms in more detail, we performed scanning luminescence at 80 K along the same line-scans as in Fig. 4.12. In sample #1360, we again observe a constant PL peak position, which is now shifted to the higher energy by 80 meV due to the band-gap increase. For sample #1361, the PL peak position shifts at 80 K to higher energy by 110 meV. At the same time, a trend of the PL maximum versus PL intensity at 80 K is inverted compared to the room-temperature data, i.e., higher intensities correspond to higher PL peak energy (Fig 4.15).
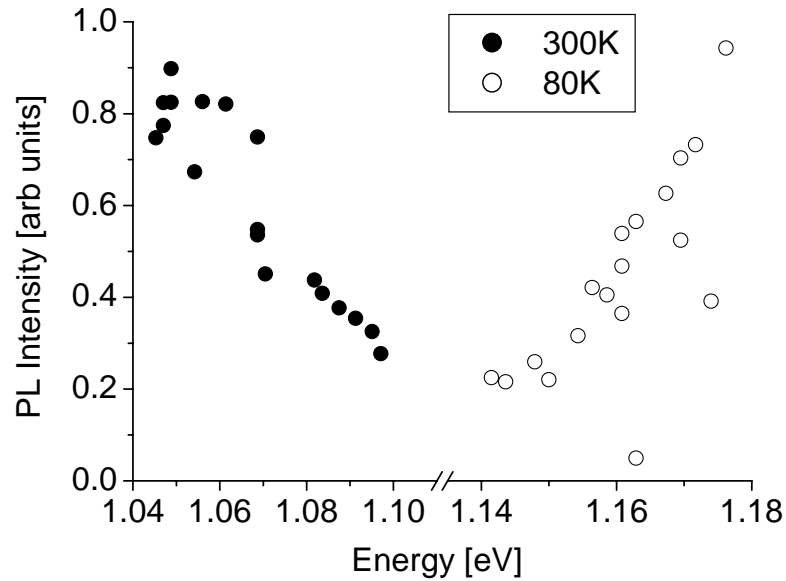
Figure 4.15 Distribution of PL intensity maxima at 80K and 300K for the sample #1361.

Note the PL intensity increase for 80K with the rising peak maxima energy,

and opposite decrease of PL with peak maxima increase for 300K

This experiment confirms the model of the QD size distribution in sample #1361. In fact, the high-energy PL bands correspond to the smallest size QDs, where the electron–hole wave functions strongly overlap and, due to this, the matrix element for optical recombination transitions is relatively large. The opposite is valid for low-energy PL bands and large QD size. At 80 K, when the thermal ionization of the QD levels is negligible, this factor governs the high PL intensity of the small-size dots. At elevated temperatures PL of the small QDs is quenched, first due to thermal ionization of trapped carriers followed by PL quenching of the large QD emission. We extracted activation energies of the PL temperature quenching from 80 to 300 K in both samples from both the high and low PL intensity regions. These values fall in the range of 260–280 meV in

all samples, which is larger than the electron–hole binding energy in the QD, which typically ranges from 50 to 100 meV [112, 113]. This large thermal activation energy was attributed to nonradiative recombination centers. Earlier it was shown that increasing the In content in the $In_xGa_{1-x}As$ capping layer changes the energy of the QD ground state, which was revealed by the PL peak shifts from 1.03 to 0.95 eV without changing its full width at half maximum (FWHM) [124]. In our experiment the PL peak also shifts to lower energy with increasing the parameter x both in high PL intensity area (from 1.04 to 1.01 eV) and in low PL intensity area (from 1.10 to 1.01 eV) in all structures. But we have also seen the change of the FWHM for the ground state PL line as a function of the parameter x.

4.1.4. Spatial PL inhomogeneity of full size QD wafers – experimental results

PL intensity maps of the 50 mm diameter InAs/InGaAs wafer are shown in Figures 4.16 through 4.19. They were measured on samples with $In_xGa_{1-x}As$ composition in capping layer equal to x = 0.10, 0.15, 0.20 and 0.25 and at the energy of the principal PL maximum, which are 1.008, 1.010, 1.035 and 1.06 eV, respectively.
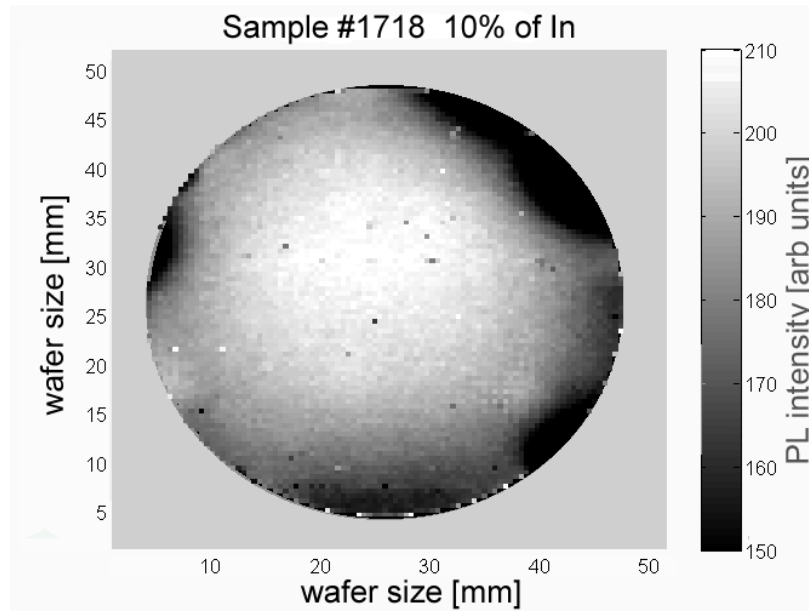
Figure 4.16 PL intensity mapping at room temperature performed at 1.008 eV on QD

structure #1718 with In/Ga composition x = 0.10, Mapping step 0.2 mm
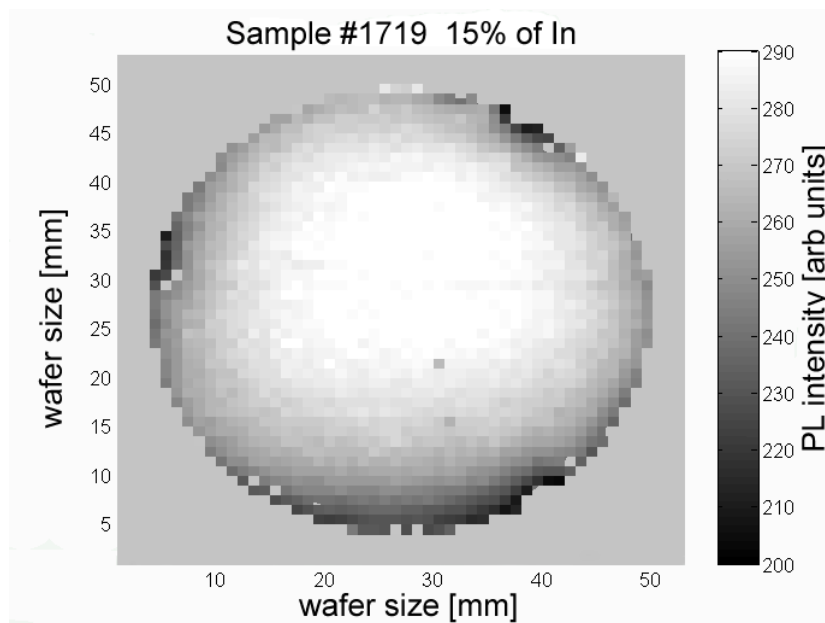
Figure 4.17 PL intensity mapping at room temperature performed at 1.010 eV on QD

structure #1719 with In/Ga composition x = 0.15, Mapping step 0.5 mm
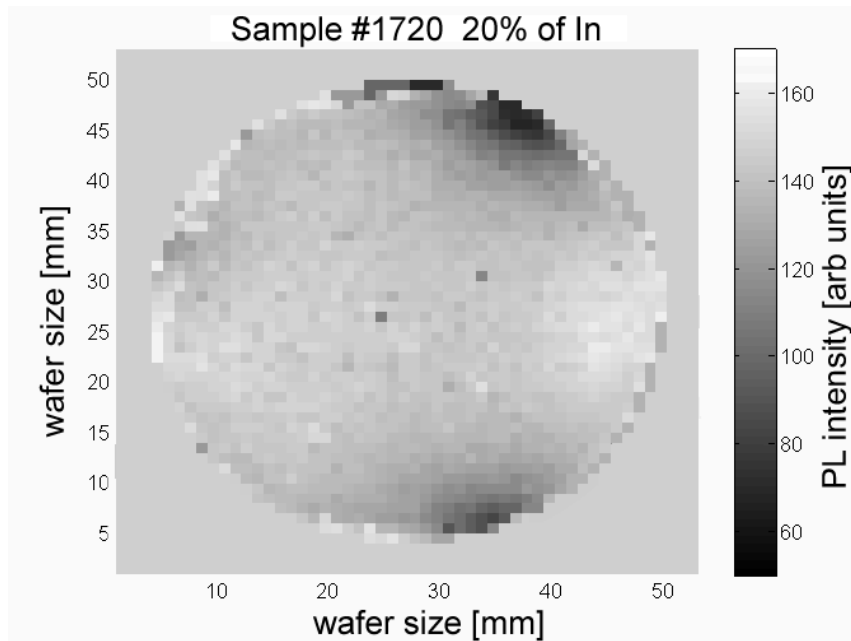
Figure 4.18 PL intensity mapping at room temperature performed at 1.035 eV on QD

structure #1720 with In/Ga composition x = 0.20, Mapping step 0.5 mm
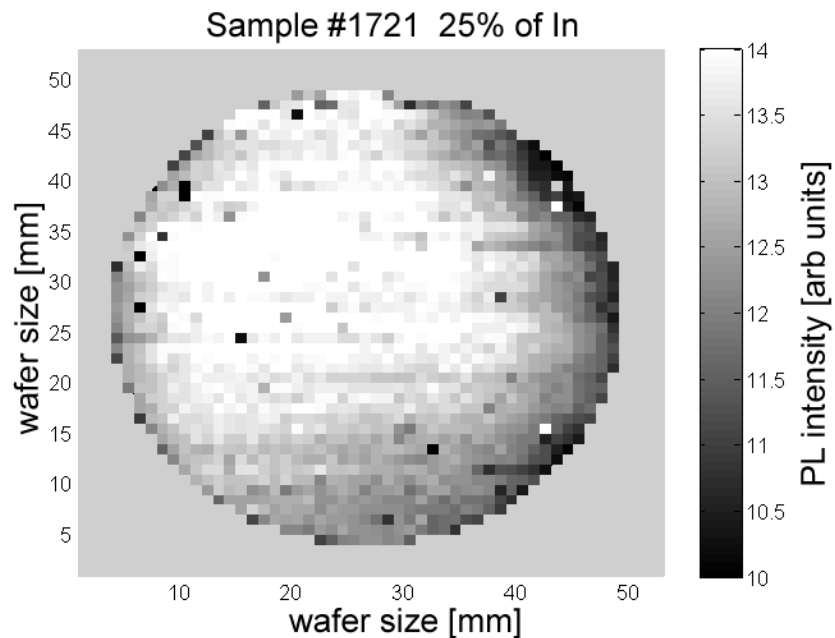
Figure 4.19 PL intensity mapping at room temperature performed at 1.06 eV on QD

structure #1721 with In/Ga composition x = 0.25, Mapping step 0.5 mm

We observe on all samples a gradual reduction of the PL intensity from the wafer center towards the periphery. This effect was confirmed by correcting the intensity maps on the shift of the PL maximum from point to point (intensity change is not connected with spectral shift). It was expected that the PL intensity of the QD structure with $In_xGa_{1-x}As$ composition in capping layer of $x = 0.15$ (#1719) was much higher in comparison with the $x = 0.25$ (#1721) structure. The average PL peak intensities over the whole sample area for all four investigated QD structures are shown in Fig. 4.20.
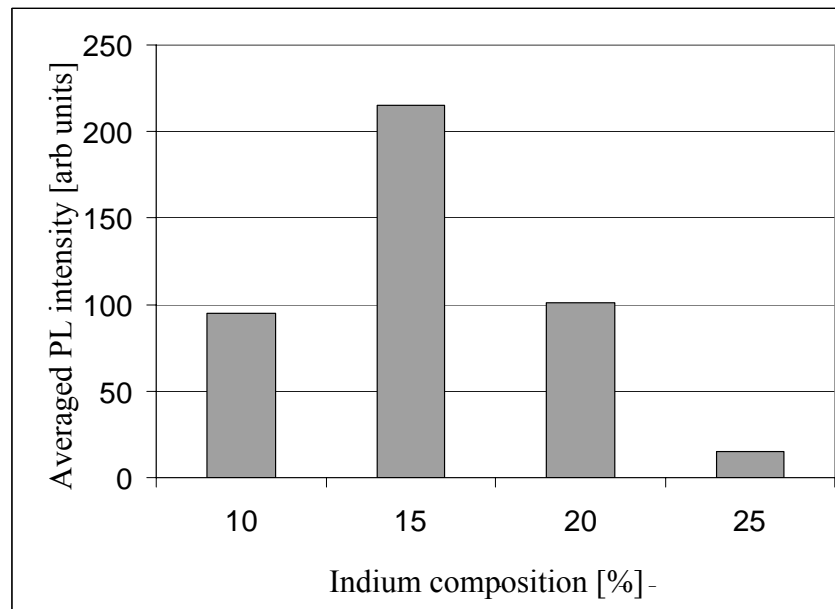
Figure 4.20   The average PL peak intensities for all four investigated QD structures
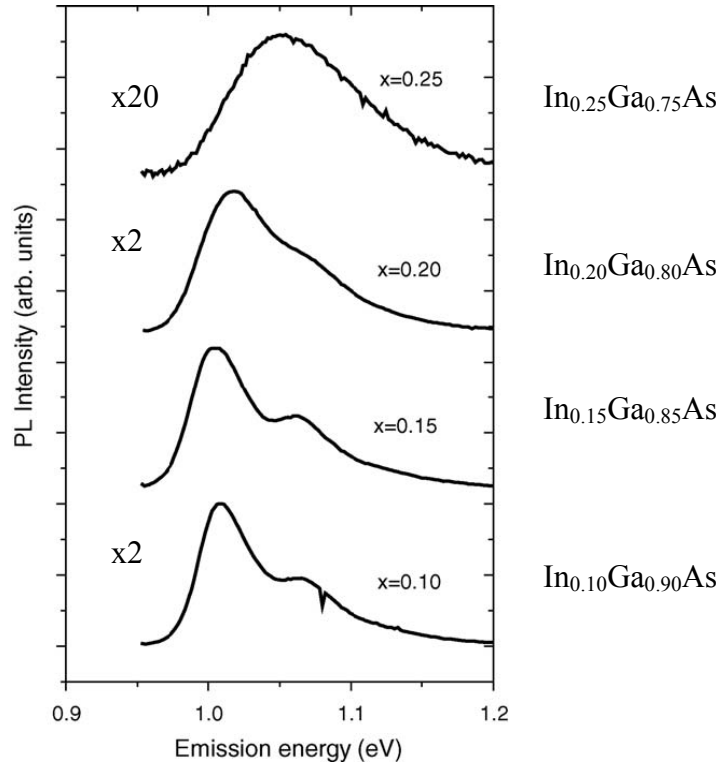
Figure 4.21 Typical normalized PL spectra corresponding to the spots with highest PL

intensities on four investigated $In_xGa_{(1-x)}As$ QD structures with variable In

composition in the capping layer

In Figure 4.21 we present normalized PL spectra for all four investigated QD samples. The structures with x = 0.10 and 0.15 are characterized by a double-band PL spectra with the half-width of the first principal maximum of 30–36 meV. These half-width values are typical for ground state (GS) emission of high quality QD structures [69, 125].The PL spectrum exhibits an additional peak at 1.06 eV, which was previously observed on high-quality QD samples and attributed to the luminescence through the excited states in the QD [112, 113]. With an increase of In composition from x = 0.10 to 0.15 the PL peak shifts into the low energy spectral range from 1.015 up to 1.007 eV. Then for QD structures with $In_xGa_{1-x}As$ composition equal to x = 0.20 and 0.25 the

direction of the PL peak shift changes and the PL peaks shift into the higher energy spectral range up to 1.030 and 1.054 eV, respectively.

With an increase of In/Ga composition in the capping layer (x = 0.20 and 0.25) the shape of the PL spectrum changes as well and the PL intensity falls off (Figs. 4.20 and 4.21). The half-width of the PL band increases up to 80 meV which indicates higher QD size dispersion for the structure with x = 0.25 (Fig. 4.21). We conclude that the electronic quality of the QD structure is superior in the sample with x = 0.15 composition of the capping layer.

Room temperature PL spectra for sample x=0.15 (#1719) measured at different intensity points are shown in Figure 40.The Principal PL maximum exhibits a gradual ''blue'' energy shift of the maximum starting at the wafers center at 1.007 eV and approaching 1.037 eV at the periphery, which matches a two-fold degradation of the PL intensity.
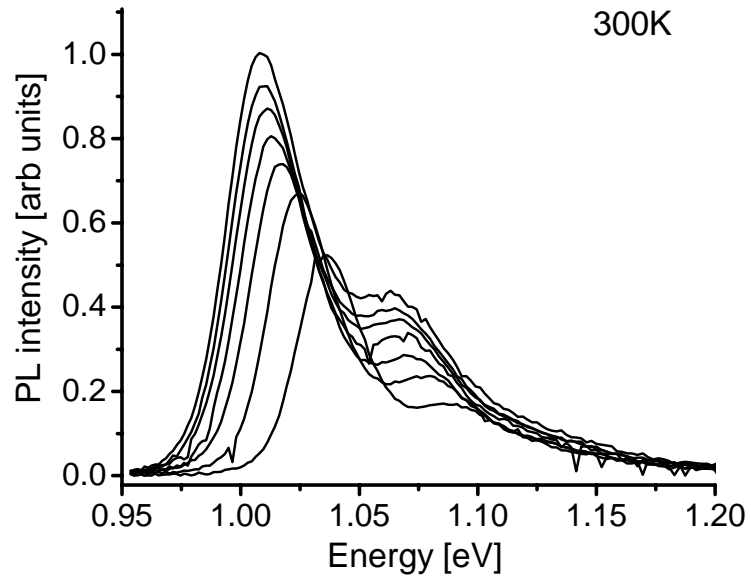
Figure 4.22   PL spectra at room temperature measured at different intensity spots (# 1719

In content x = 15%)

4.1.5. Spatial PL inhomogeneity of full size QD wafers – discussion

As we have shown earlier [section 4.1.3] the scanning PL results on the InAs/InGaAs QD structures indicate two separate physical mechanisms of PL intensity inhomogeneity. The first mechanism is not accompanied by a PL spectrum shift. In this case a drop of the PL intensity can be related to an inhomogeneous distribution of the QD density across the wafer and (or) of the density of nonradiative centers, competing with QD luminescent transitions. The second mechanism of the PL intensity change is accompanied by a PL spectrum shift and deals with the QD size variation along the QD structure.

We interpret the spectroscopic PL mapping on the InAs/InGaAs QD's 50mm samples grown with different composition of the capping InGaAs layer as a result of the dot size decreasing from the center of the wafer toward the sample periphery in a similar way to the samples from section 4.1.3. This is exhibited as a ''blue'' shift of the PL maximum. This effect leads at the wafer periphery to shallower QD localized states (i.e. smallest electron and hole binding energy), poorer carrier localization and, as a consequence, a higher probability of carrier thermal ionization, which reduces their room temperature PL intensity. It is possible that in the smaller quantum dots, carrier wave functions penetrate more into the barriers surrounding the dot and overlap more with non-radiative point defects. In this case, the intensity of the PL for smaller QDs should decrease faster with increasing temperature.

Room temperature PL intensity variation across the wafer can be described by the dependence:

$$I_{PL} \approx \exp\frac{-h\nu_{max}^{GS}}{kT} \tag{14}$$

Where I_{PL} is the PL intensity, $h\nu_{max}^{GS}$ is the energy of the ground state, k is Boltzmann constant and T is temperature. This is demonstrated by the fitting line in Fig. 4.23.
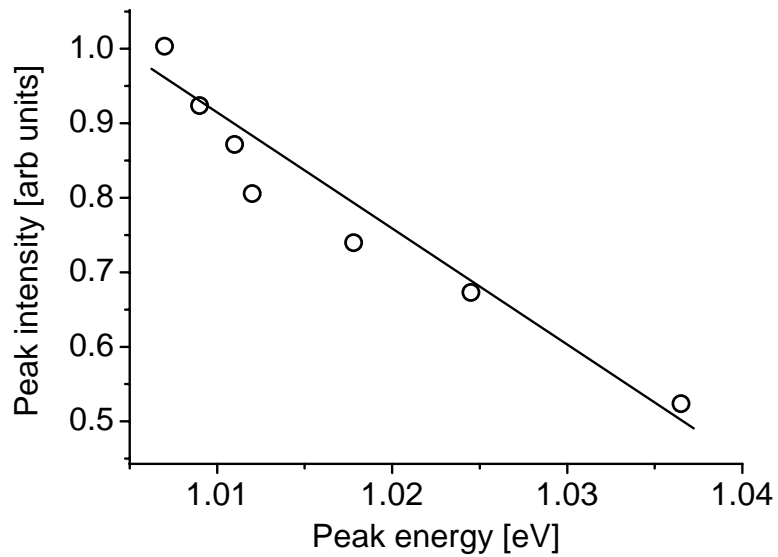
Figure 4.23 PL maxima peak position vs. its intensity (#1719 In content x = 15%)

Earlier it was shown that increasing the In content in the $In_xGa_{1-x}As$ capping layer (from 0.10 up to 0.30) changes the energy of the QD ground state, which was revealed as the PL peak shift from 1.03 to 0.95 eV without variation of the band half-width [124]. The last effect was explained [124] as the result of stress decreasing on the InAs/InGaAs interface. In our experiment for QD structures with x = 0.10 and 0.15 the PL peak shifts by the same way in the low energy spectral side. But for QD structures with x = 0.20 and 0.25 the PL peak shifts in the opposite direction. This difference in the PL spectral behavior may be related to the difference in investigated QD structures. In all our QD structures below the wetting layer there is an $In_{0.15}Ga_{0.85}As$ buffer layer. In Ref. [124] the InAs QD layers were grown directly on GaAs layers. Moreover, the thickness of capping $In_xGa_{1-x}As$ layers in [124] was decreased with the parameter x increasing with the aim to prevent approaching of the critical thickness and the start of the stress relaxation process

in QD structures [126]. In investigated QD structures the reason for PL peak position shifts into the ''blue'' side with a variation of $In_xGa_{1-x}As$ composition (x = 0.15, 0.20 and 0.25) can be related to partial InAs QD decomposition at higher elastic stress conditions and to partial elastic stress relaxation in QD structures with x > 0.15 [127]. In the investigated QD structures the thickness of the $In_xGa_{1-x}As$ capping layers was the same in all structures and equal to 7 nm—the height of the QDs. This $In_xGa_{1-x}As$ thickness for QD structures with x > 0.15 is more than critical for the nucleation of misfit dislocations at the InGaAs/GaAs interface [126]. Actually this may be the reason of partial stress relaxation in QD structures for x > 0.15 with the appearance of dislocation and non-radiative recombination centers. The later assumption can be confirmed by a decrease in the PL intensity of the QD structures with the parameter x equal to 0.20 and 0.25 presented in Fig. 4.18 and 4.19. Note we made the assumption above that the density of QDs along the line that we measured the spectra on the wafer does not change essentially and the main reason for the PL intensity change is the QD size distribution. Actually, as was shown in Ref. [128] for the AFM investigation of the same type of uncapped InAs QDs grown on the $In_{0.15}Ga_{0.85}As$ buffer layer, the density of QDs across the wafer changes not more than 50%. It is really not an essential variation in comparison with the observed two- to four-fold magnitude variation in the PL intensity signal at room temperature.

4.2. PL spectroscopy of CdSe/ZnS quantum dots for bioapplications

4.2.1. Photo-induced enhancement of the PL intensity – introduction

The stability and efficiency of QD luminescence is a critical aspect for the technology. Under intense laser or electron beam illumination, a strong degradation of the luminescence intensity was observed and attributed to the photo-ionization of nano-crystals and subsequent trapping of the ejected electrons in the surrounding semiconductor matrix [87]. Therefore, even in capped QDs with wide-gap semiconductors as the barrier or those embedded into a ZnS matrix, photo-degradation occurs. On the other hand, it was documented previously that the luminescence and photocurrent intensity are increased under light illumination in the bulk CdS and CdSe crystals [71, 129]. This was identified as light-induced defect reactions caused by donor–acceptor pair dissociation, assigned to a photo-chemical process. A similar effect of photo-induced PL enhancement was noted in the glassy close-packed films of CdSe QDs covered with a ZnS film [87]; however, the process was not studied in detail. A reversible PL intensity photo-enhancement ('photobrightening') was also observed at low temperatures in CuI and CuBr nano-crystals embedded into a glass or polymer matrix and attributed to photo-generated carrier trapping and their release when the temperature was increased [130, 131]. The experimental study of the PL photo-enhancement effect in pure and bio-conjugated CdSe/ZnS core-shell quantum dots was performed. While we specifically focus on the pure QDs, the light-induced PL enhancement is also observed in bio-conjugated samples.

4.2.2. Photo-induced enhancement of the PL intensity – experimental results

PL spectroscopy was performed between 80 K and room temperature using a 50 mW HeCd laser line at 325 nm and a 200 mW Ar+ laser line at 488 nm as the excitation source. Laser power density varied by use of calibrated neutral density filters and was focused down to a 100 μm spot. For low intensity measurements the laser beam was unfocused with an approximately 1.5 mm laser spot diameter at the sample surface. Commercially available CdSe/ZnS polymer coated quantum dots from Quantum Dot Corp. [11] were used in this experiment. A sample of the Qdot 655 Goat F(ab')$_2$ anti-Mouse IgG conjugate in a form of a mm-size spot was dried on a polished surface of a crystalline silicon substrate to achieve a low level of scattered light. One dried spot contained 2 μl of QD bio-conjugate diluted with a phosphate buffer (PBS) in a 1:50 volume ratio. Bio-conjugated samples contained Qdot 655 F(ab')$_2$ complex fragments conjugated to OC125 detector antibodies that recognize the CA125 anti-gene molecule, used in the early stage detection of ovarian cancer. Some experiments were done on the QD−F(ab')$_2$−OC125 bioconjugate structure before attachment to the CA125 anti-gene molecule. The PL spectrum of the CdSe/ZnS quantum dots in the range of 0.73–3.54 eV (350–1700 nm) exhibits only one prominent luminescent band with the maximum at 1.89 eV (655 nm) and half-width of 90 meV at room temperature (Figure 4.24).
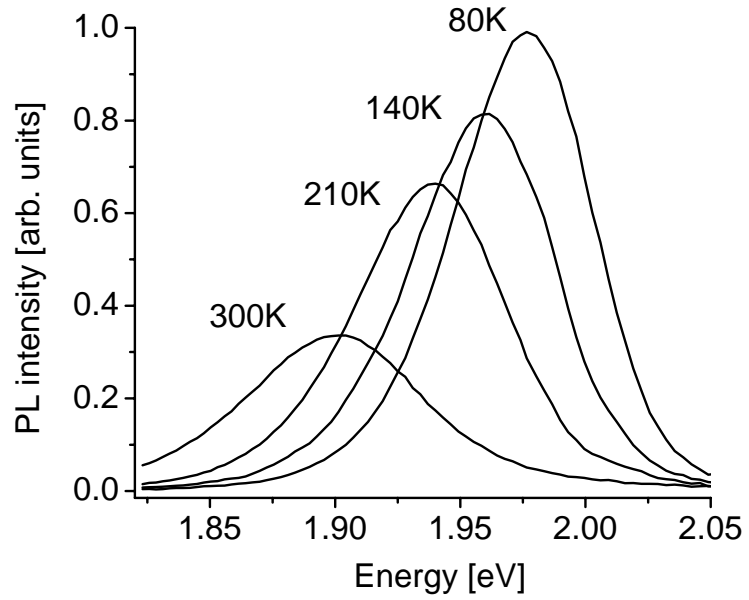
Figure 4.24 PL spectra of CdSe/ZnS QDs measured at different temperatures: 80 K, 140
K, 210 K and 300 K. Note the blue shift as the sample temperature
decreases

When the temperature is decreased, the PL maximum shows a narrowing and 'blue' shift following the temperature band-gap variation of the bulk CdSe, which is described in Figure 4.25 by a solid line using the Varshni equation [132].

$$E_g(T) = E_g(0) - \frac{\alpha T^2}{(T + \beta)} \tag{15}$$
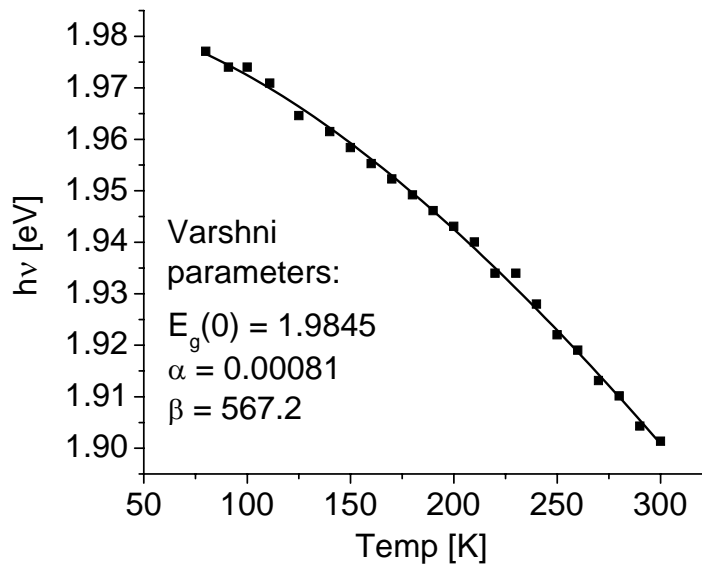
Figure 4.25 PL maximum versus temperature variation (points) and fitting with the Varshni equation (solid line) using parameters: Eg(0) = 1.9845 eV, α = 0.00081, β = 567.2

We concentrate here on the transient characteristic of the luminescence which is exhibited as a variation of the PL intensity versus sample exposure with the excitation laser. To explore the transient, the kinetic curves of the PL intensity versus exposure time, I(t), are measured at different power densities of the 325 nm HeCd laser excitation. In Figure 4.26, we present luminescence kinetics of the QDs diluted in the 1:50 ratio in PBS measured at the maximum of the PL spectrum of 655 nm.
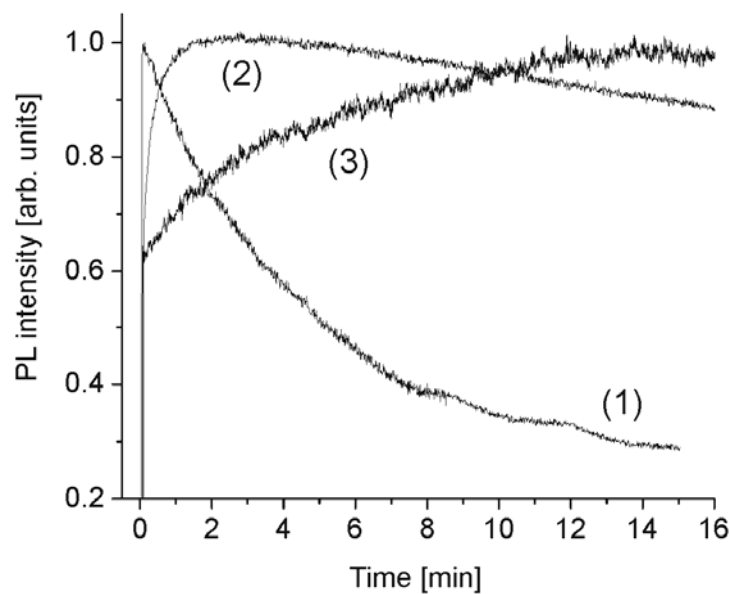
Figure 4.26 PL intensity variation of the 655 nm luminescence band at room temperature for different laser power densities (W-cm^{-2}): (1) −500; (2) −20, (3) −0.2. The PL intensity is normalized using a multiplication factor of 25 in curve (2) and 2500 in curve (3)

At the highest laser power density of 500 W cm^{-2} (laser spot focused down to 100 μm), we observe a strong photo-quenching, when the luminescence intensity degrades by a factor of 3 from its maximum value within 15 min (curve 1). At lower excitation power, it is recognized that this photo-quenching follows an initial PL increase, hereafter photo-enhancement, as shown on curve (2). When the laser power density is reduced further, the enhancement kinetic starts to dominate quenching, and with laser power of a few W cm^{-2} it is possible to clearly separate the enhancement part as illustrated by curve (3). We explore in this study the enhancement kinetic only, which is strongly motivated as a potential means to improve the quantum efficiency of the bioconjugated QDs. The following observations were depicted on the basis of the transient PL study. (1) PL

photo-enhancement amplitude can be quite substantial, spanning the range from 10% up to fivefold with respect to the initial luminescence intensity. (2) The enhancement effect is observed both at 325 nm (HeCd) and 488 nm (Ar+) laser excitation. The enhancement rate is increased (time constant reduced) at higher excitation power density as illustrated in Figure 4.26. (3) If the sample subjected to UV exposure was held in the dark for a definite time, the enhancement effect can either be recovered, which is assigned to reversible enhancement (RE) and the kinetics can be repeated again, or the effect can exhibit the non-reversible enhancement (NRE) and show no recovery at room temperature for at least overnight sample storage. Typically RE and NRE occur simultaneously. Both RE and NRE kinetics are thermally activated, meaning that they are substantially slowed down when the temperature decreases. Specifically, the RE time constant (τ_{RE}) yields tens of minutes at 300 K and its transient kinetic is no longer observed below 240 K. The PL spectrum measured at room temperature before and after the enhancement completed shows no noticeable variation of the peak position and the half-width. Cycling the light-induced PL enhancement and dark recovery leads to a cycle-by-cycle permanent increase of the PL intensity as illustrated in Figure 4.27.
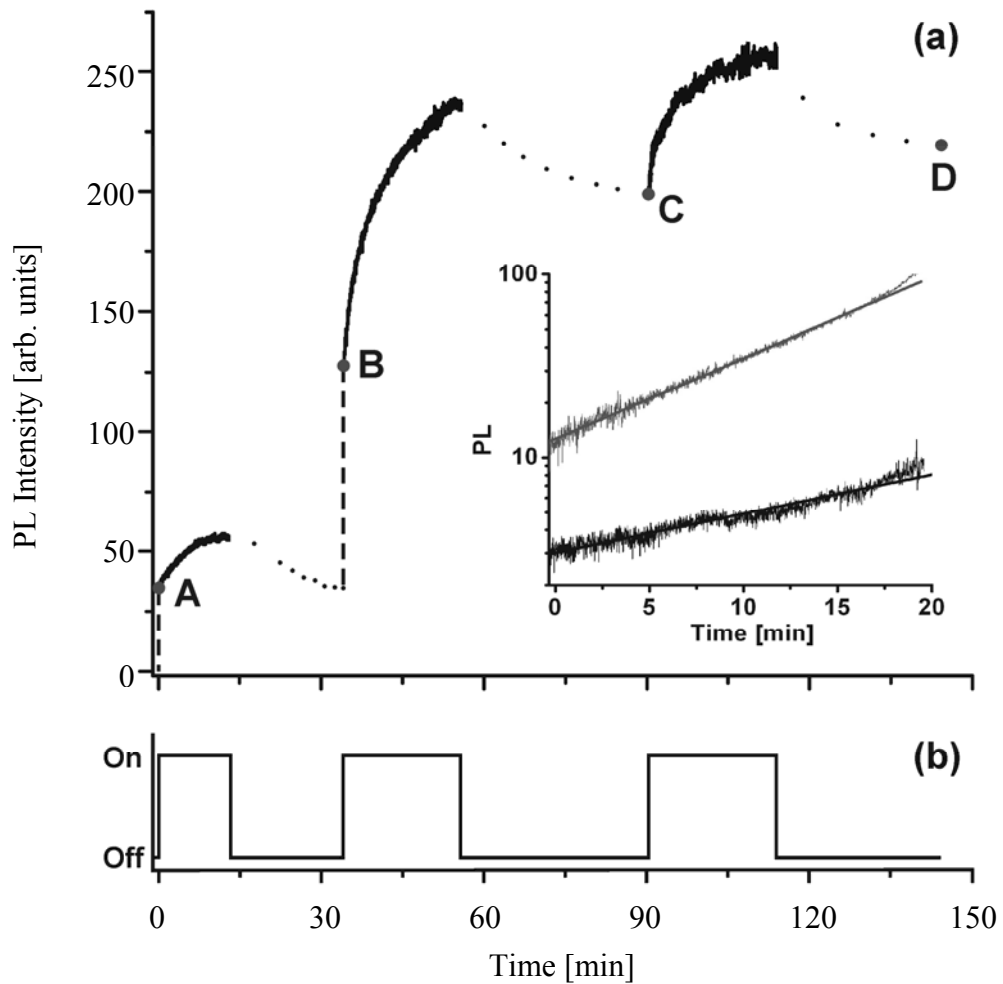
Figure 4.27 (a) Cycling kinetics of light-induced PL enhancement and dark recovery at room temperature; (b) time dependence of sample illumination, using 325 nm HeCd laser. Points A, B, C and D illustrate gradual increase of the PL intensity at the beginning of the consecutive enhancement curve. The inset shows two consecutive kinetics revealing time constants of (1) 9.4 min and (2) 20.6 min

This suggests that both RE and NRE occur in parallel. We emphasize the significant features of both processes. The NRE amplitude is exponentially increased with illumination time yielding the time constant of approximately 180 s at room temperature. This is indicated by points A, B, C and D in Figure 4.27. We observed that a time constant of the RE process is gradually increased from one cycle to the consecutive cycle. Generally, it is complicated to describe RE kinetics with a single exponent at room temperature due to a superposition with the NRE process. A single exponential curve is observed either at the very first PL enhancement when complete recovery occurs, or after multiple enhancement–recovery–enhancement cycles when the NRE process is completed. The recovery time constant is close to 30 min. It does not change between various cycles and increases at lower temperatures.

The QD samples can be classified into two different groups according to the PL transient features. Group 1 samples show negligible RE kinetics and the entire transient is controlled by the NRE process. Group 2 samples exhibit both RE and NRE kinetics possessing comparable amplitudes. We were unable to realize samples where RE dominates over NRE. This sample selection allowed separating the input of both processes in temperature-dependent luminescence. Additional insight and complementary data on the photo-enhancement effect yield the PL intensity temperature dependences, I(T). They were measured using three different sample states: (Fig. 4.27 point A) the initial state, prior to any PL enhancement, (Fig. 4.27 point B) the RE state, when the reversible process is saturated while the NRE is negligible and (Fig. 4.27 point C) the NRE state, when the non-reversible effect is completed. To assess the (Fig. 4.27 point A) state, the sample was cooled down to 80 K in the dark. The spectral PL maximum was

acquired within 60 s at a low laser excitation of 20 mW cm^{-2}. After this, the excitation light was turned off until a consecutive higher temperature point was stabilized and the PL spectrum sweep was performed again. We intentionally increased the dark holding time between individual temperatures to ensure that the RE process, which may start during the PL measurement, was diminished. These precautions allowed for minimization of the PL enhancement effect. State (Fig. 4.27 point B) was achieved on group 2 samples after the very first room-temperature PL enhancement is saturated using a fast sample cooling down to 80 K with UV light on. In this case, the relaxation is terminated and the RE effect is not erased. Finally, state (Fig. 4.27 point C) was measured in group 1 samples after long-term ~30 min illumination at room temperature to saturate the NRE processes.
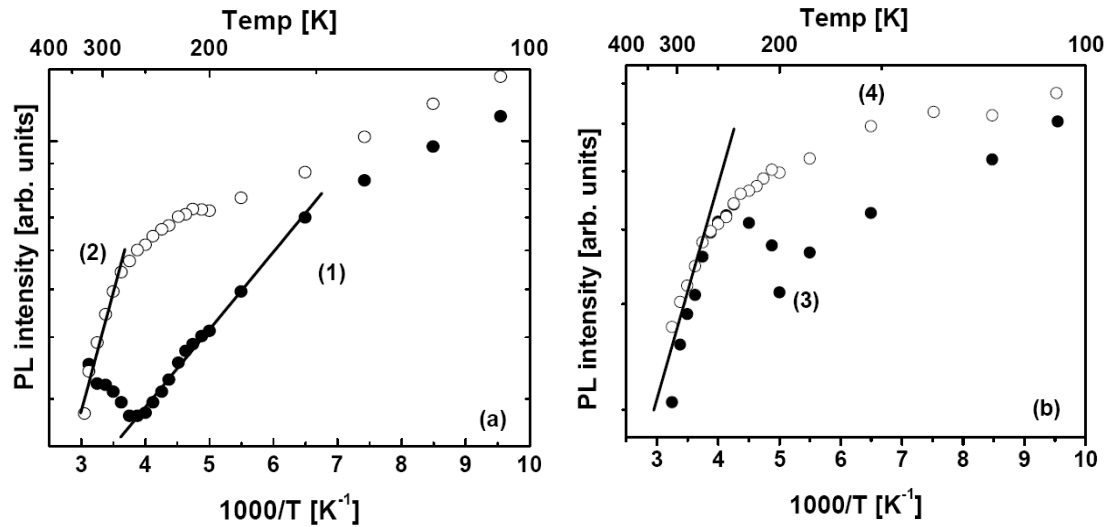
Figure 4.28 The PL temperature dependence before and after (a) the NRE process and (b) the RE process. Curves (1) and (3) correspond to the initial state measured on two different groups of samples. Curve (2) corresponds to the NRE state, and curve (4) to the RE state. Solid lines show linear fit to extract the activation energy of the T-quenching

99

The dependence I(T) before and after completing the NRE is presented in figure 4.28(a) by curves 1 and 2, respectively. At the initial (Fig. 4.27 point A) state, the PL intensity decreases or quenches when the temperature increases from 80 to 300 K. This is attributed to a thermally activated release of photo-generated carriers from the CdSe quantum dot levels over the potential barrier and recombination at nonradiative defects in the ZnS, polymer or at interfaces. The Arrhenius plot, log(I) versus 1/T, reveals the activation energy of PL quenching in the (Fig. 4.27 point A) state ε_A = 33 meV. It is important that above 250 K we observe the PL increase which is attributed to the NRE process. After NRE occurred (curve 2 Fig 4.28(a)), the PL increased over the entire temperature range from 80 to 300 K; however, the largest changes are observed at temperatures of the steepest quenching in state A, between 180 and 250 K. By completing the NRE (Fig. 4.27 point C state), the sharp PL quenching range is shifted to higher temperatures while the activation energy values range from ε_C = 75 to 90 meV (different values in different samples). We may conclude that the photo-stimulated NRE process leads to a noticeable increase of the potential barrier for confined carriers to escape the quantum dot.

In Figure 4.28(b), we compare I(T) dependences before and after RE occurred. Comparing with NRE curves in Figure 4.28(a), we noted that the region of PL increase region is shifted towards lower temperatures and a minimum of the PL intensity is observed now at 200 K. In this case, however, the PL increase is not related to the RE process, which occurs at higher temperatures. Above 250 K, the PL is quenched again with the activation energy of 45 meV corresponding to the (Fig. 4.27 point B) state of the

sample. After RE occurred, the PL enhancement is mostly expressed in the range of T-quenching, similar to the NRE case.

4.2.3. Photo-induced enhancement of the PL intensity - discussion

When thermally released from the QD levels, photo-generated carriers can annihilate at other recombination centers or can be captured by traps located at interfaces, in the barrier or surrounding polymer shell. When both electrons and holes are released, the competition of other recombination centers dramatically reduces the PL intensity exhibited as temperature quenching (Figure 4.28). The carrier trapping may lead to the appearance or neutralization of the local electric field or exhibit Auger recombination leading to PL reduction [87]. The trap recharging may cause an increase of the potential barrier height for carriers to be released from the QD levels, which would enhance the PL output. Concurrently, one would expect time-dependent processes for establishing equilibrium of rates between carrier generation, recombination and trapping. The PL transient may show a characteristic time much longer than the PL recombination time due to dynamic carrier trapping [133]. This is attributed to the fact that photo-generated carrier trapping reduces recombination flow at the QD levels. When majority traps are recharged at low temperatures, the PL intensity approaches a stationary level. This mechanism was proposed to explain PL photo-brightening in CuI quantum dots [131]. We note that the mechanism described strongly depends on the ratio of the recombination rate in the QDs (τ_{PL}^{-1}) and capture rate at traps (τ_{cap}^{-1}). If these rates are comparable, the PL intensity may show a substantial increase during the transient. However, in this case

the transient time is short, on the order of the recombination time in the QDs (τ_{PL}). In the opposite case when $\tau_{PL}^{-1} \gg \tau_{cap}^{-1}$, the PL transient is slow, but as a consequence the PL enhancement effect is negligibly small. This simple analysis allows ruling out the transient mechanism of the PL enhancement in our case. The following observations are critical and form a basis to interpret the effect and specify a mechanism of the photo-stimulated enhancement of the QD luminescence intensity.

- PL increase occurs after a direct absorption of the 488 nm laser light in the CdSe core rather than in the ZnS shell or the polymer, that are transparent at this wavelength. Similarly this is true for the 325 nm HeCd laser considering the negligible thickness of the ZnS and polymer transparency at this wavelength.

- Both processes of RE and NRE are activated in the range of the PL temperature quenching.

- The activation energy of the PL quenching is increased after the photo-enhancement process is completed, changing from 33 to 45 meV for RE and 33 to 75–90 meV for NRE.

These data allow us to formulate the following statements. The increase of the PL intensity is observed at the temperature range of the PL quenching while the quenching decreases after the PL enhancement. Both RE and NRE processes are accompanied by an escape of carrier(s) from the quantum dot levels. Therefore, the experimentally observed PL increase is caused by a reduction of the carrier flow over potential barriers to non-radiative centers. This reduced flow is a result of the increased potential barrier for photo-generated carriers to escape the dot and recombine non-radiatively. It is obvious that

defects and traps outside the well in ZnS layers or at interfaces play an important role in both RE and NRE processes due to the fact that carriers are released from the QD states. It is known that carrier trapping leads to recharging of the traps and can result in the compensation of the local electric field around the QDs. This may cause a PL increase opposite to the PL quenching under light or electron beam irradiation attributed to the Auger recombination that can be realized after carrier trapping [87]. Alternatively, the light exposure may stimulate photo-chemical reactions studied widely in II–VI compounds [134, 135]. Therefore, the activation energy of the PL enhancement can be attributed either to the potential barrier increase for carriers to escape the quantum well or, alternatively, to thermal activation of the photo-chemical reaction. The activation energy can be assessed from the kinetic curves measured at different temperatures. However, our attempts to perform this failed in accuracy due to the superposition of RE and NRE. On the other hand, we can estimate a change of the activation energy of the RE using the following analysis. According to the experiment (insert in Figure 4.27), the time constant of RE is increased by a factor of 2–6 in different samples after completing NRE. This allows an estimate of the variation of the activation energy independently. The time constant, τ, of a temperature-activated process is related to the activation energy (ε) and absolute temperature as follows:

$$\tau = \tau_0 \exp\left(\frac{\varepsilon}{k_B T}\right) \tag{16}$$

where k_B is the Boltzmann constant. An estimation of ε increase, $\Delta\varepsilon = \varepsilon_2 - \varepsilon_1$, can be performed from the ratio of time constants, τ_1/τ_2, of the photo-enhanced kinetics measured at two different states of the sample, as follows:

$$\frac{\tau_1}{\tau_2} = \exp\left(\frac{\varepsilon_1 - \varepsilon_2}{k_B T}\right) = \exp\left(\frac{\Delta\varepsilon}{k_B T}\right) \qquad (17)$$

This estimation yields a value of $\Delta\varepsilon$ = 17–45 meV, which is in a reasonable range

for the barrier variation from 33 meV to (75–90) meV accessed from the PL temperature

quenching curves measured at different sample states presented in figure 4.28. Thus, we

conclude that the activation energy of the RE process is determined by the height of the

barrier for carriers to escape the QD. We can briefly discuss the origin of processes

leading to the photo-stimulated increase of the QD's potential barrier as illustrated in
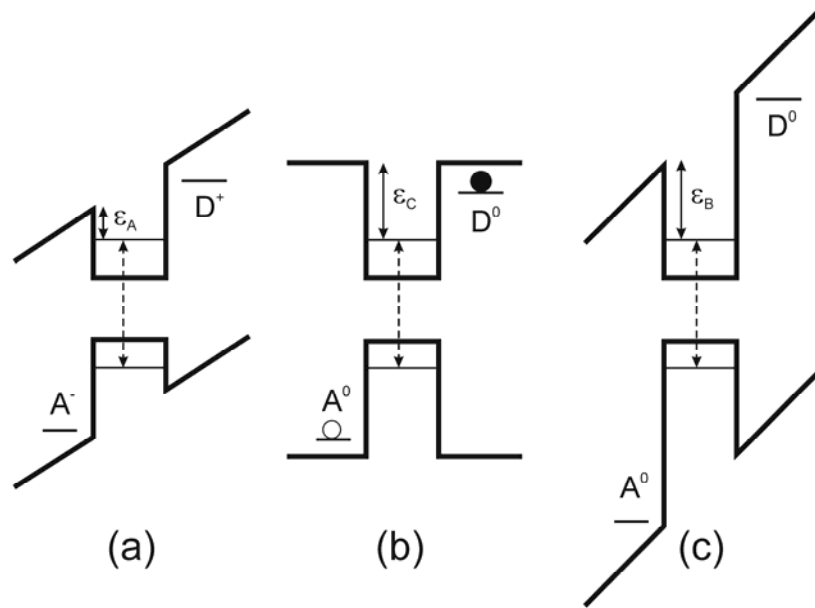
Figure 4.29.

Figure 4.29 Model of the light-induced PL enhancement illustrating different states of

the QD sample: (a) initial state at the beginning of PL kinetics. The potential

barrier ε_A is reduced by the electric field generated by charging the electron

trap (D+) and hole trap (A−) in the dark; (b) photo-enhanced state when the

luminescence increased due to the recharging of traps according to equation

(3); (c) final state after relaxation of the reversible enhancement process. It

is suggested that the non-reversible process is driven by photo-chemical

reactions. PL transitions are depicted by the dashed arrows

As was mentioned, the processes can be attributed to the recharging of the

interface trapping states and change of the local electric field at the QD, or alternatively,

to the atomic bond restructuring classified as photo-chemical processes in II–VI

compounds. The QD's surface charge can reduce the exciton PL intensity. This can be a

result of the exciton ionization in the external electric field as observed in the photo-

conductivity study of close-packed glassy solids of colloidal CdSe QDs [136]. In the

opposite case, the compensation (neutralization) of the surface charge would lead to the

PL increase due to the stabilization of the exciton, increasing its binding energy, and

reducing the PL thermal quenching (Figure 4.29(b)). We emphasize that if only one type

of photo-generated carrier is captured and the other left on the QD level, the Auger

mechanism would reduce the PL intensity as was predicted in [137] and observed

experimentally in [87]. Therefore, we postulate that both the electron and hole after being

released from the QD states must be captured by spatially separated and charged donor

(D+) and acceptor (A−) defects, correspondingly. This leads to the neutralization of these

defects and reduction of the surface charge (i.e. electric field), and as a consequence an

increase of the exciton PL intensity. The following reactions describe this process:

$$D^+ + e \Rightarrow D^0 \,; A^- + h \Rightarrow A^0. \tag{18}$$

This is illustrated in Figure 4.29 as the QD energy diagram when the trap-related

electric field is active ((a) and (c)) or compensated (b). It is conceivable that the RE

process is caused by a trap recharging which can be reversed due to a temperature-

activated release of carriers from the traps (Figure 4.29(c)). Similarly, the NRE effect may also be accounted for by carrier capture at deeper trapping states. In this case, the recovery could occur at higher temperatures. This, however, was not observed experimentally; heating the sample above 320 K leads to a strong PL degradation and eliminates following photo-enhancement. We suggest tentatively that NRE is linked to a photo-chemical reaction of the bond restructuring. Alternatively, the described RE process can also be attributed to a photo-chemical process of light-induced trap elimination followed by their temperature-activated recovery [138]. Experimentally, it was observed that when temperature is below 200 K luminescence degradation is noticeable, caused by the Auger process due to enhanced non-radiative recombination after capture of light-generated carriers by traps [87]. When the temperature increased above 200 K these traps are emptied, which results in a PL increase due to suppression of the Auger process (figure 4.28(b), curve 3). This is evident due to a 'dip' at 200 K in the T-dependence. It is important that the dip is completely removed from the T-dependence after RE was performed (curve 4). We can postulate that a reversible photochemical reaction occurs due to light absorption in QDs above 200 K, which leads to the trap elimination. By holding the sample at room temperature in the dark, recovery of the traps and the dip are seen again.

4.2.4. PL spectroscopy of bio-conjugated QD's

4.2.4.1. PL mapping of ELISA plates

The first step to perform Enzyme-Linked Immunosorbent Assay ELISA [115] experiments was to establish dilution curves for a given marker. In our case we started to dilute pure QDs to determine the limits of detection for our system. Stock solutions of purchased QDs (non conjugated) were diluted with the antibody diluting buffer (TRIS Buffered Saline from DAKO Corp.) [139] in the volume ratios in the range from 1:20 down to 1:2000. Figure 4.30 presents the initial concentration measurements. CdSe quantum dots are detectable in the dilution ratio of 1:2000 on the background of ELISA plates (Flat bottom immuno plate, VWR international) [140].
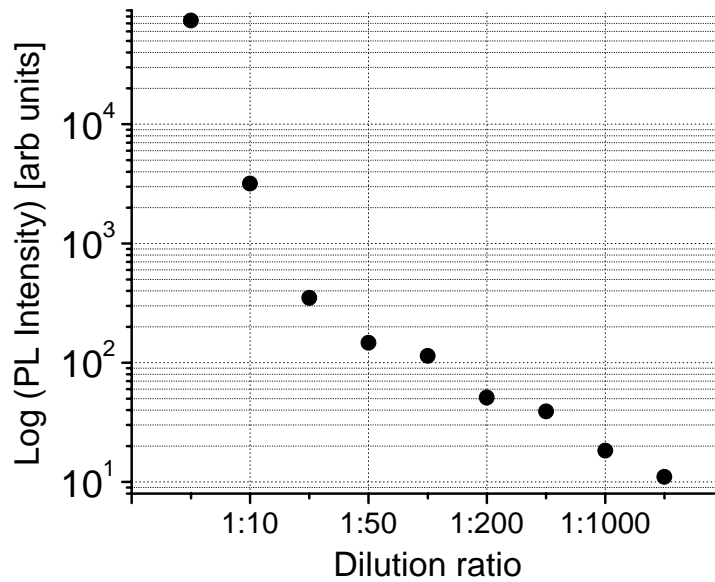
Figure 4.30 PL intensity vs. dilution ratio of QD 525 diluted in a Tris (DAKO) buffer
[139]

The PL mapping of whole ELISA wells with the full immuno reaction shown in Fig 4.31 was performed. Used wells had their surface covered with biotin (biotinolated) in order to attach capture antibodies for our detection scheme (see Fig 4.31(a)).
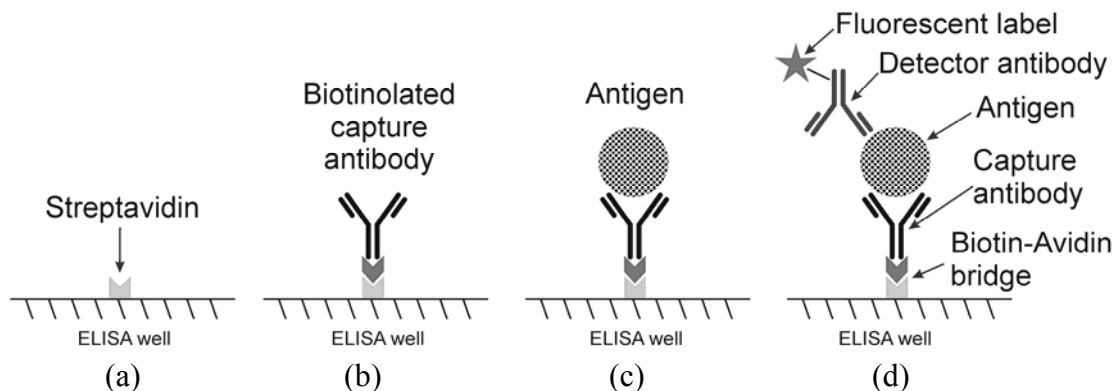
Figure 4.31 ELISA imunoreaction attachment "sandwich" diagram for streptavidin coated wells. This scheme was used to attach the QD (fluorescent label) to the biotin-avidin bridge as shown

After attaching capture antibodies from the liquid phase, wells were rinsed to remove any unbound capture antibodies (Fig 4.31 (b)). The next step was the addition of known amounts of antigen to prove that conjugation took place. If the conjugation reaction follows the assumed scheme the averaged PL intensity should reflect the different amounts of antigen (Fig 4.31 (c)). The last step was to add labeled (conjugated) quantum dots with the specific detector antibody in order to "see" the presence of bound antigen molecules.

300 U/ml	200 U/ml	100 U/ml	neg control
(a)	(b)	(c)	(d)
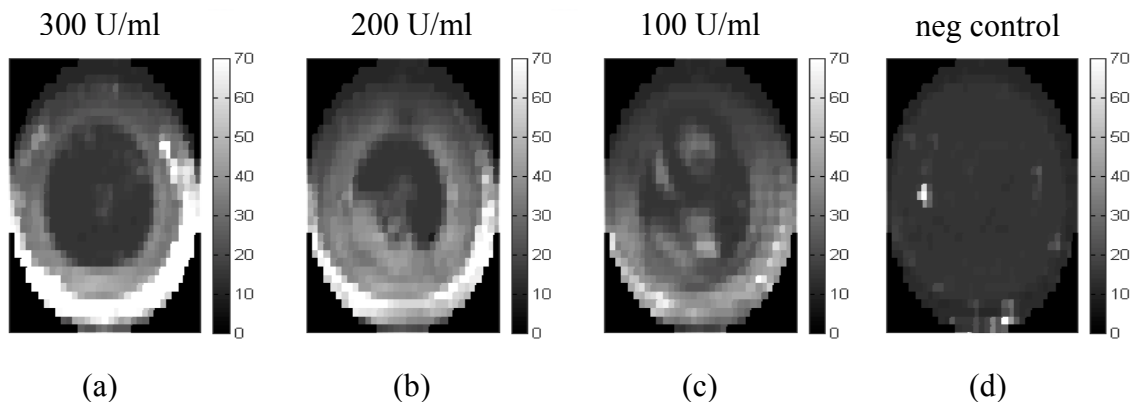
Figure 4.32 Map of four ELISA wells with different concentrations of antigen CA125. (a) 300, (b) 200 (c) 100 and (d) 0 Units/ml (the unit of measurement for this marker is femtomole per milligram of tumor). Map was collected at 655 nm (1.89 eV), for the OC125 (250 u/ml) − CA125 (antibody − antigen) complex labeled with QD655 quantum dots. Mapping step 0.2 mm

Figure 4.32(d) shows the ELISA plate and well with zero antigen content which is called the negative control. The purpose of this control is to prove that there are no residues of labeled detector antibodies left. The absence of antigen in the immuno reaction chain will prevent attaching tagged detector antibodies to the ELISA wells, what is reflected in the PL intensity map of Fig 4.32(d). The non uniformity of the PL intensity at the bottom of the wells may be contributed to wash and drying step artifacts that attribute greatly to the accuracy of this approach and has to be taken into account during averaging and background removal in order to obtain a useful signal (smallest noise/signal ratio).
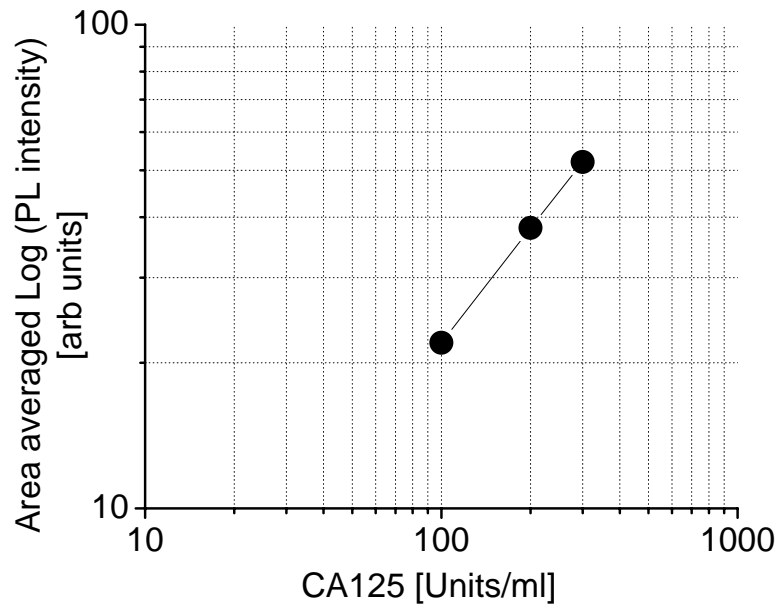
Figure 4.33 Averaged over the well bottom area PL intensity signal for OC-CA125

complex from maps shown in Figure 4.32

The averaged PL intensity dependence shows a linear dependence of the PL signal vs. antigen concentration. This linear part of the standard curve (curve that represents given marker signal PL in our case vs. its concentration) shows that we are above the limit of detection for this given marker, since we don't see the lower non linear part of this curve. We can still decrease this biomarker concentration for this ELISA. A classical standard ELISA curve representing the optical density or extinction coefficient versus concentration is shown in chapter 3 Fig 3.7. This curve consists of a linear region when the detection is most accurate and two saturation regions at very high and very low concentrations establishing limits of detection for a given ELISA.

This experiment was repeated with larger number of samples of different antigen concentration for many times without any success in improving the calibration curve for different antibody-antigen complexes used (IL10, PSA, M11 and CA125). Figure 4.34 shows an example of the ELISA map of 12 wells at 655 nm that no correlation between antigen concentration and PL intensity signal can be found. Unfortunately the wells that were meant to be negative controls show the highest PL intensity which allow some to draw a conclusion that the actual QD presence inside the wells has nothing or at least very little to do with the actual bioconjugation and only random QD residue is giving a signal. The search for spectral features of bioconjugation has to be carried on the samples with proven immuno reaction what leads us to another approach for the conjugation confirmation technique, employing a microarray which is described in next section.
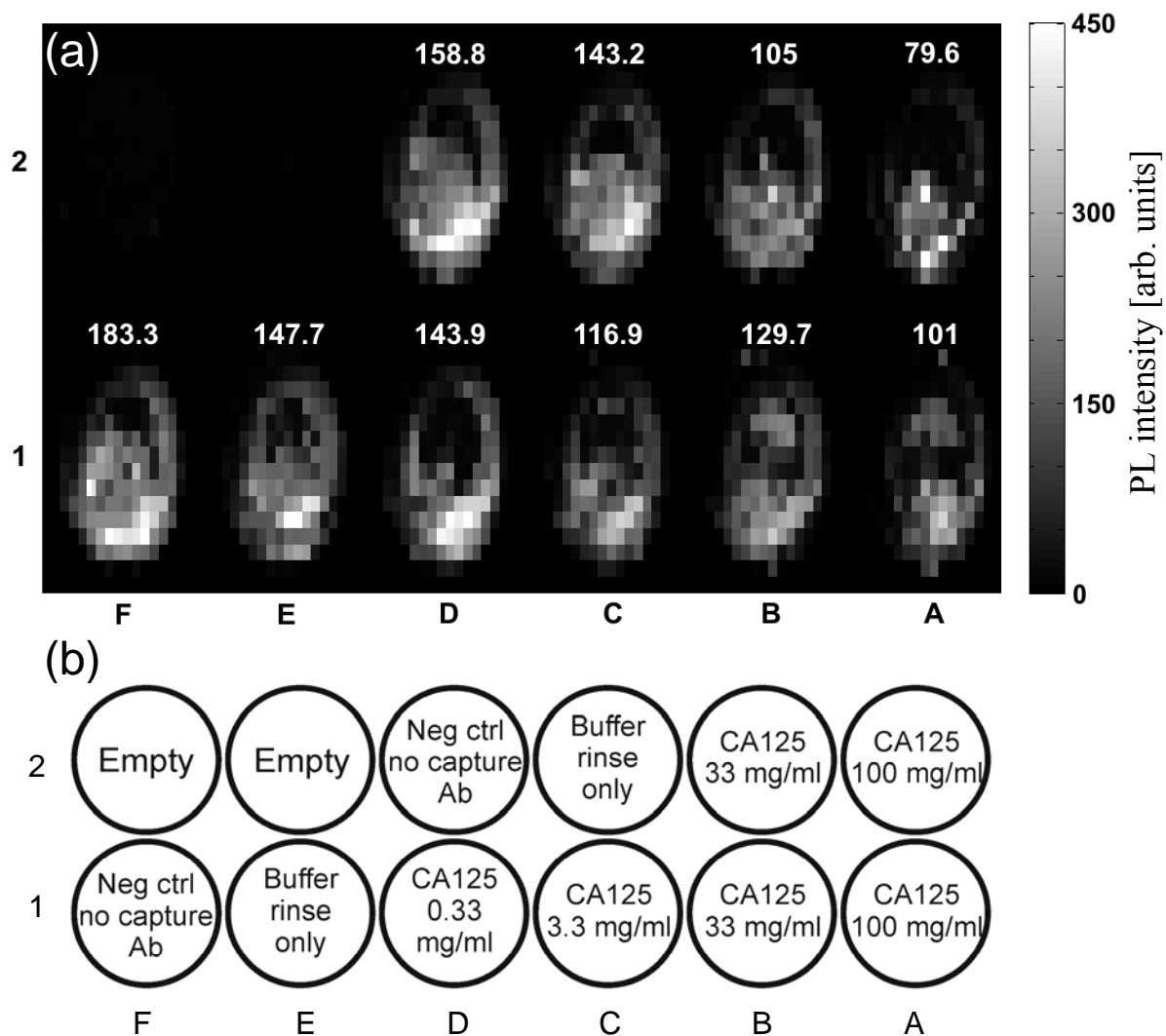
Figure 4.34 (a) Map of ELISA plate composition with different amounts of CA125 antigen (at 655 nm); numbers shown above each well at the map represents averaged PL intensity in each well, (b) description of the well content

4.2.4.2. Bioconjugation with micro array technique

The micro array technique that we have employed is very similar to the ELISA approach when it comes to the immuno reaction scheme. The major difference is the

substrate and the method of attaching the capture antibody. The antibody is printed on the functionalized substrate surface (with nitrocellulose or aldehydes) and it's confined to a spot of 100 - 200 μm in diameter. A major advantage of this approach is that it uses a very small amount of sample (up to a couple of μl) and the spots can be printed very densely allowing for many different reaction schemes to occur over relatively small areas. Wash steps in the same condition for the whole slide basically eliminate any wash artifacts that were present in previous ELISA's. Each spot is printed with the different needle making this process very efficient and fast for different antibodies and their concentrations. A single microscope glass slide can have up to a couple of hundred spots printed in the single pass of micro array printer.

For the micro array experiment we prepared samples by conjugation of nanocrystals to antibody specific to the selected marker − IL10 in this case, and the second one by use of streptavidin coated quantum dots and biotinylated detector antibody. The same biotin-avidin bridge was used this time to conjugate the QDs to the detector antibody Monoclonal capture (clone JES3-9D7) rat anti-human Interleukin-10 antibody, detector (clone JES3-12G8) rat anti-human Interleukin-10 antibody, and recombinant human Interleukin-10 were purchased form Serotec (Raleigh, NC) [141]. Microarray nitorcellulose coated glass slides were purchased from Whatman (Sanford, ME) [142] and a Quantum Dot 655 antibody conjugation kit was purchased from Invitrogen (Carlsbad, CA) [11]. The conjugation of detector rat anti-IL10 antibody to QD655 was performed according to the provided protocol [114]. Six arrays of capture rat anti-IL10 antibody at 0.5mg/ml (1:2 dilution in printing buffer (TeleChem International, Sunnyvale, CA)) [143] were printed on nitrocellulose coated glass slides. After spotting

the slides were placed in a box at a temperature of 4°C overnight. The next morning the slides were rinsed with PBS (Sigma-Aldrich, Germany) [144] and blocked with blocking buffer (Whatman; Sanford, ME) [142] for one hour. After rinsing again with PBS the slides were incubated for 2 hours with human IL-10 solutions in PBS at 500 ng/ml (2 arrays), 1000 pg/ml (2 arrays) and 100 pg/ml (2 arrays) and then rinsed again with PBS. Half of the arrays were incubated with detector rat anti-IL10 antibody conjugated to QD655 (20nM) and the remaining half with biotinylated rat anti-IL10 antibody for 1 hour with gentle rocking. Following incubation, the slides were rinsed with PBS and three arrays, previously incubated with biotinylated detector antibody, were incubated for 30 min with streptavidin QD655 (Invitrogen; Carlsbad, CA) [11], diluted (1:50, 20nM) with Tris–Buffered Saline (Dako; Carpinteria, CA) [139]. Slides were first rinsed with PBS then water and centrifuged dry at 2500 rpm for 3 minutes. The slides were then imaged under a fluorescent microscope (Nikon Eclipse E800) [145] equipped with Qdot655 filters and qualified using custom designed software which utilizes computerized dynamic analysis system (CDAS) for classifying microarrays to measure the features on spots: such as area and intensity profiles [146, 147].
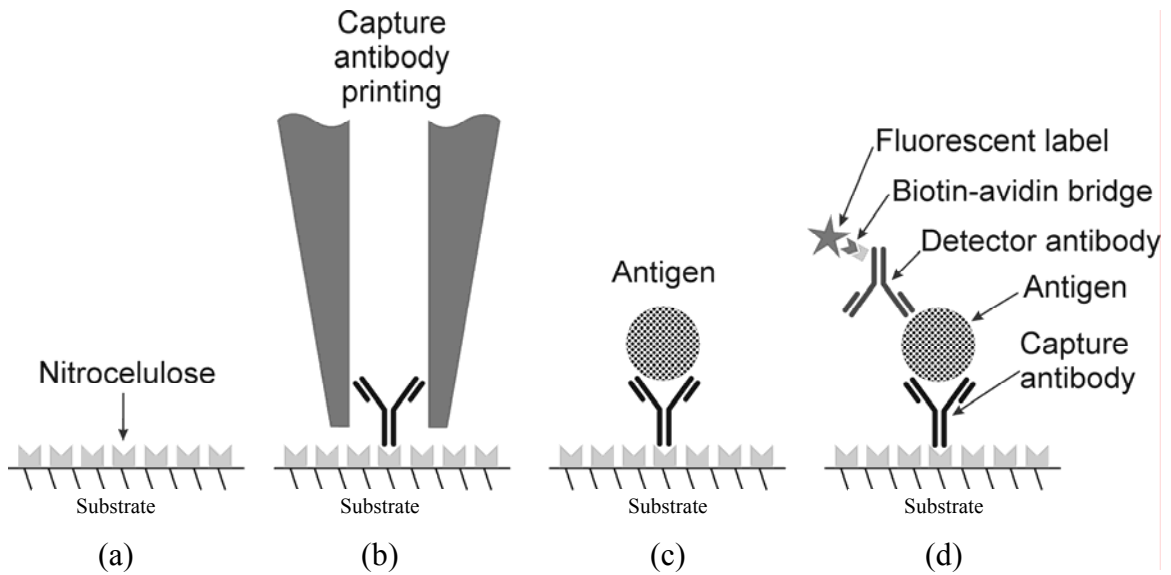
Figure 4.35 Micro array immuno reaction "sandwich" diagram for nitrocellulose coated substrate
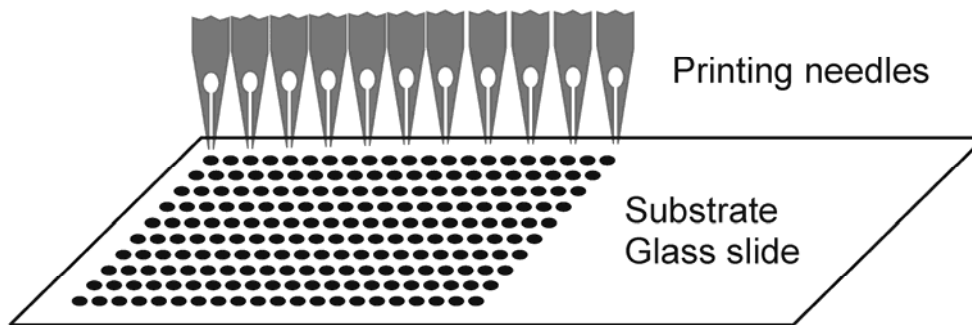
Figure 4.36 A glass substrate can hold up to couple hundred spots of different antibodies or their concentrations. The spots are printed as shown schematically

These samples were read by a fluorescence confocal microscope. A mercury lamp was used as the excitation source and a set of band pass filters and a dichroic mirror served as the means to determine the excitation and emission wavelength parameters. For

the QD 655 samples an excitation low pass filter with the cut off wavelength of 460 nm was used and the band pass emission filter of 650 nm with the 20 nm band width. The example of a fluorescent image is shown in Figure 4.37.
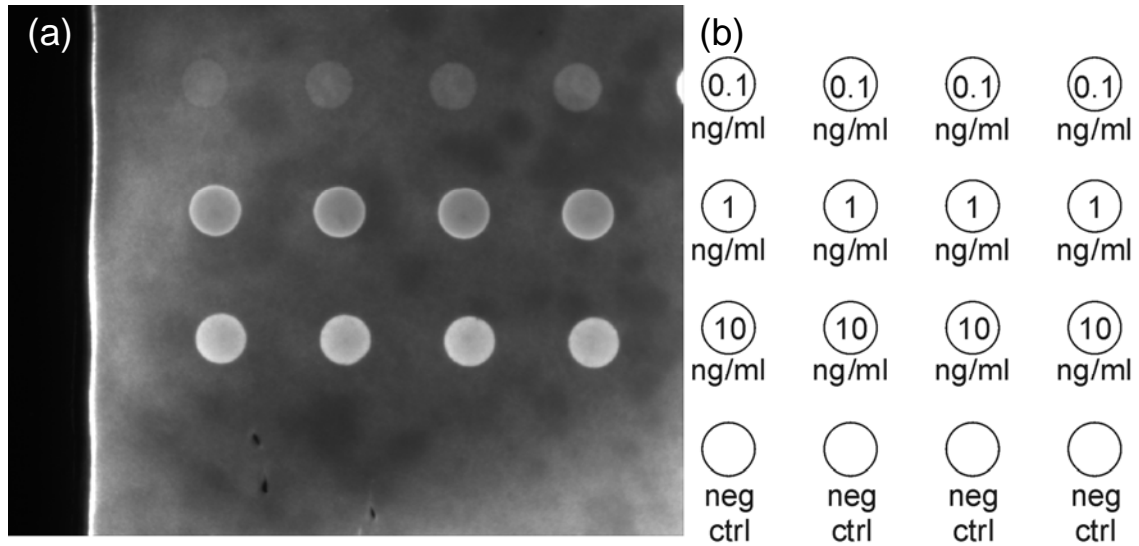
Figure 4.37 Example of fluorescent microscope image (mag. 2.5x) of the small part of an array printed from micro array printer (QD655 + IL10 complex) with 100 μm spot diameter (a), spots description (b)

We have also performed a protein microarray assay with streptavidin coated QD and biotinylated detector antibody to detect human IL10 over the range of concentrations from 500 ng/ml to 500 fg/ml. Utilizing the "sandwich" assay technique (Fig 4.35) we have used a nitrocellulose coated glass substrate, rat anti-human IL10 (IgG1, JES3-9D7) capture antibody, biotinylated rat anti-human IL10 (IgG2a, JES3-12G8) detector antibody, recombinant human IL10 and streptavidin coated QD655 as a label (Fig 4.35 (d)).
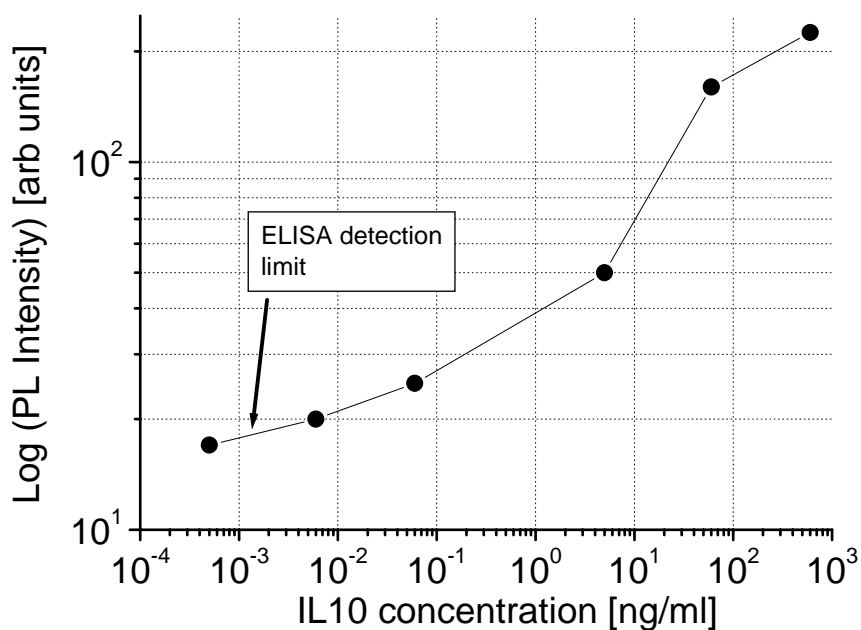
Figure 4.38   Calibration curve of the IL10 antigen concentration detected with the QD

665 label and the micro array technique

The recorded PL intensities for the micro array slide showed much more repeatable calibration with over 4 orders of magnitude of the useful linear range. (see Fig 3.7 for the corresponding ELISA concentration curve in chapter 3). The same experiments were repeated on a Si substrate for the PL spectroscopic measurements. The Si substrate was used as a very low background for UV excitation of our samples (see section 3.2).

4.2.4.3. Spectral shift of QD luminescence caused by bio-conjugation

With the proven and repeatable bioconjugation of quantum dots we performed detailed spectroscopic maps of dried sample spots on a Si surface with larger spot sizes than micro array diameter, around 2 mm. The drying process itself introduced some non homogeneity, (Figure 4.39) but this time we investigated the spectroscopic signatures of bioconjugation and the overall sample PL intensity was of secondary importance.
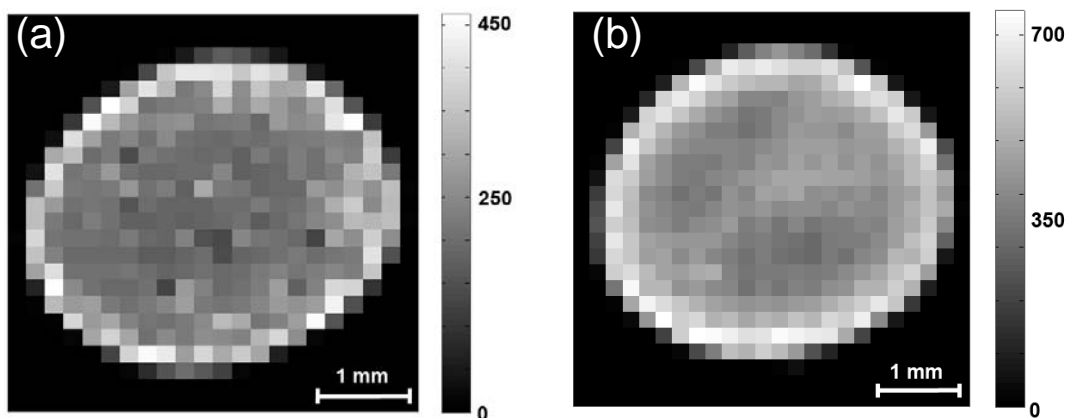
Figure 4.39 PL intensity maps of two drops/spots on a Si substrate – (a) conjugated and (b) non-conjugated. Spectra measured at each point of respective map (QD655 + anti-Interleukin10)

These maps have spectra measured at every single spot, the spatial resolution is 0.2 mm for 2 mm diameter spots which yields approximately 80 spectra per spot. The conjugated spot which contains the QD655 + IL10 complex proven to be conjugated in the previous section while the non conjugated spot is just a drop of pure quantum dot solution as it was purchased from the manufacturer.
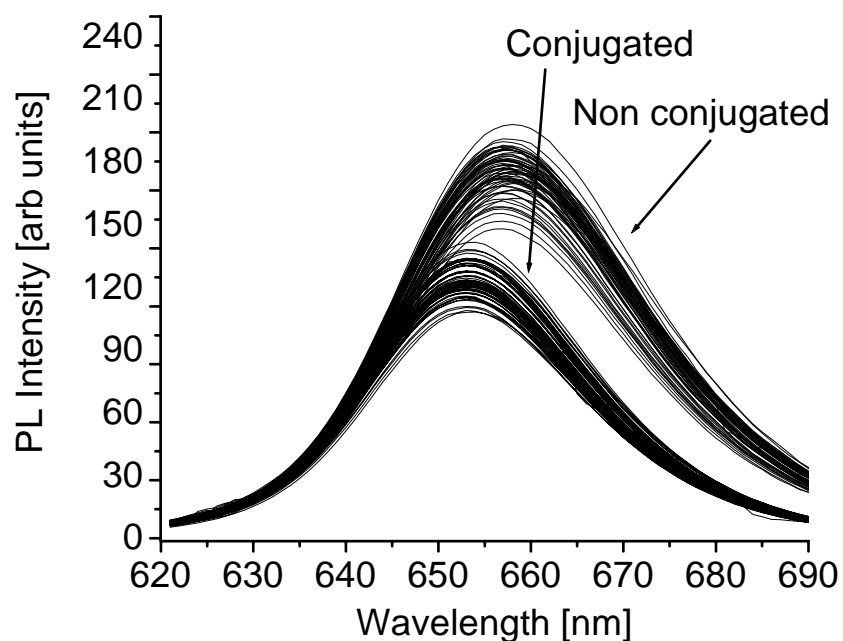
Figure 4.40   Spectra measured on every map spot presented in Fig 4.39

Normalized spectra from Figure 4.40 are shown in Figure 4.41, it is clearly seen that the conjugated complex have their spectra shifted on average by 4 nm (Figure 4.42) in comparison to non conjugated ones. The shift is towards a shorter wavelength "blue" shift for conjugated quantum dots. Its existence was confirmed with repetition of the conjugation scheme with identical parameters and the "blue" shift was observed in all repeated experiments. We believe the surrounding molecules that are attached to the QD are responsible for this result, although more experiments need to be done to investigate the mechanisms involved.
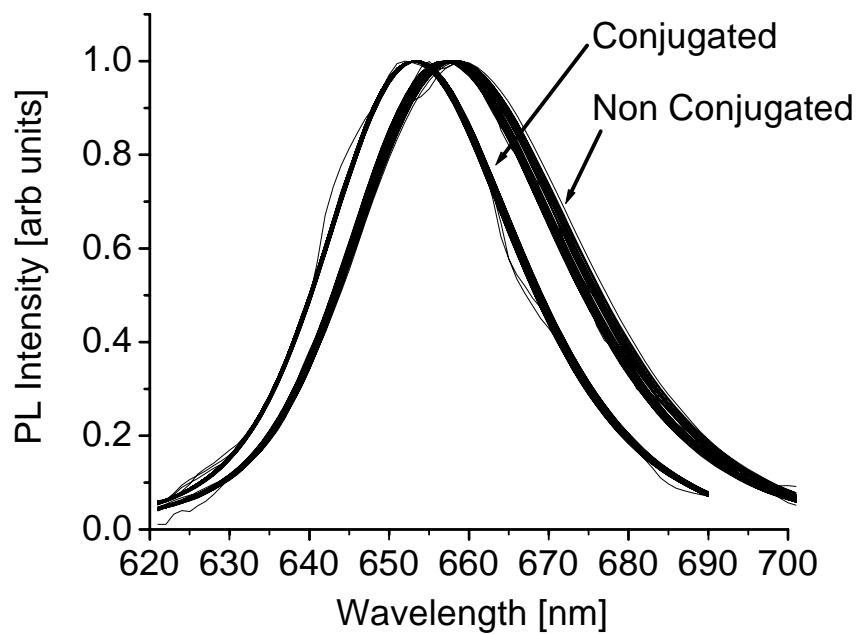
Figure 4.41 Normalized spectra measured on every map spot presented in Fig 4.39 (single spectra are plotted on top of each other to show shift for the whole group − width of each curve is caused by single spectra spread for given sample)
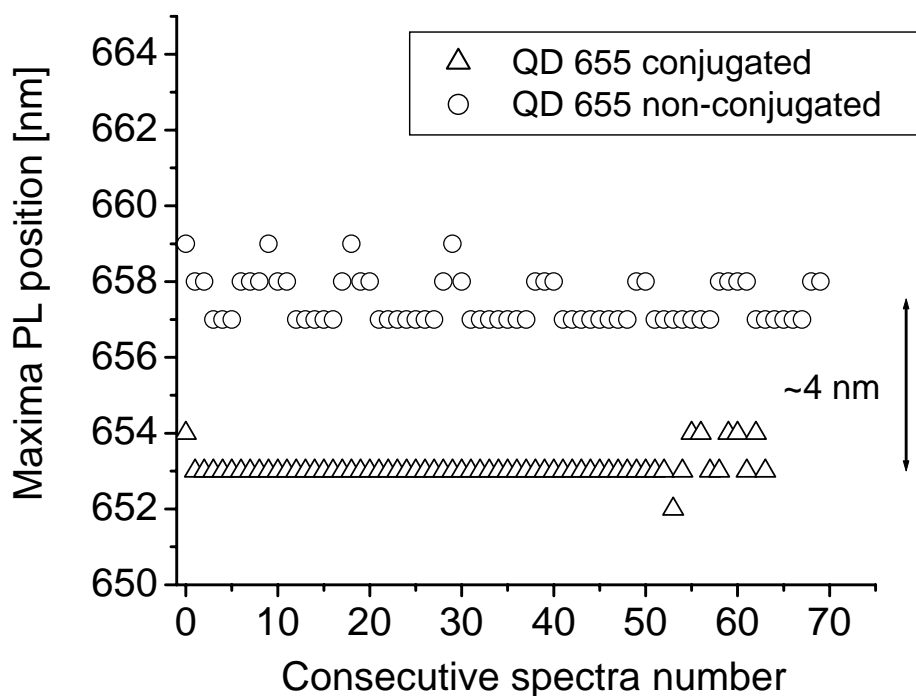
Figure 4.42 Peak position for all spectra measured over conjugated and nonconjugated spots. The average peak separation "shift" is 4 nm for QD655+IL10 complex vs. pure QD655

The shift was also observed for other QD sizes (different emission wavelength maxima) namely 605 (4 nm in diameter) and 705 (7 nm in diameter) [148]. Experiments were carried out in a similar manner as for the 655 QDs. The spots were dried out on a Si surface and mapped with 0.2 mm spatial resolution. Spectra were recorded at each spot and their maxima position and relative shift vs. non conjugated QDs is presented in Figure 4.43.
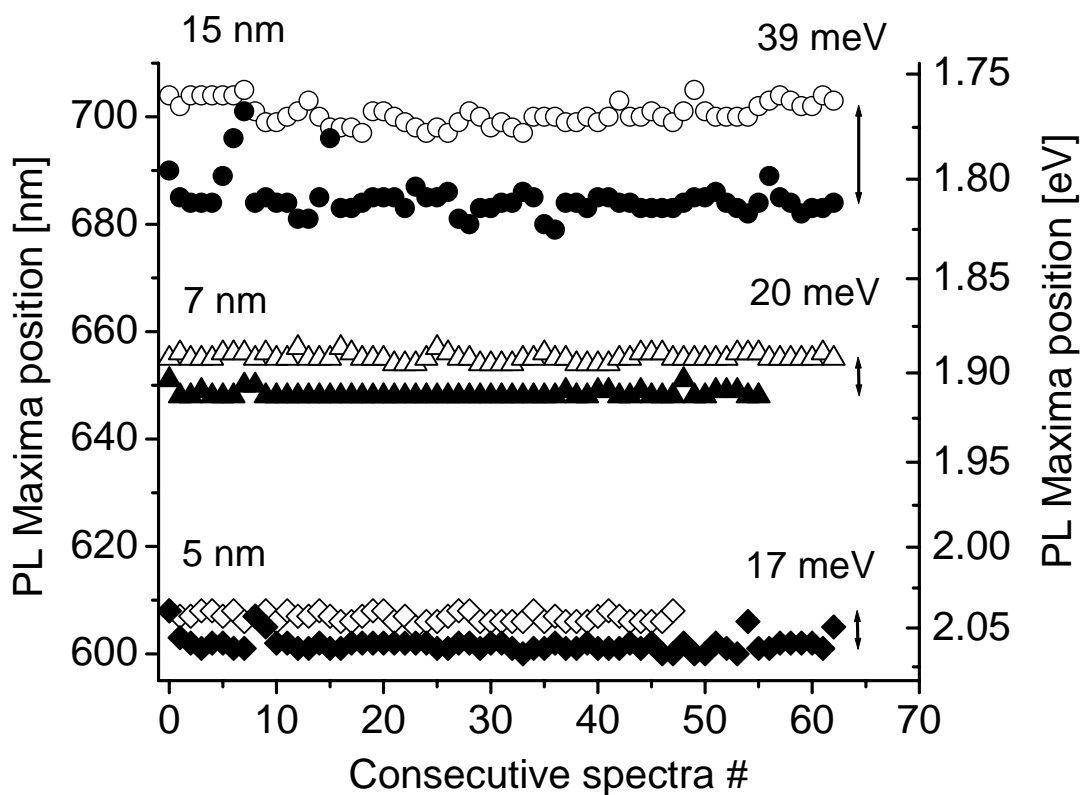
Figure 4.43 Relative shift of nonconjugated QD's vs. conjugated to IL10 antibody for

605, 655 and 705 QD's

The spectral shift is different for QDs of different sizes; it is larger for quantum dots of big diameter (see Figure 4.43). The PL intensity kinetics under UV light was also measured for these samples, which was quite similar for non-conjugated and conjugated QD samples.

The spectral shift observed on bio-conjugated QDs with antigens may be attributed to the existence of an external local electric field that is imposed by the surrounding biomolecules (Stark effect). Bio-conjugation occurs in most cases by covalently bound bio-molecules attached to the polymer coating layer [148] or through ionic interaction with a linkage molecule [93]. The electric field of the polarized covalent bio-molecule or charged linkage molecule can be strong enough due to close proximity to the QD core of a few nanometers. The electric field has a strong effect on the lower lying hole states of the exciton which has been shown by Klimov and Jankovics [149, 150] and it affects to less extent the electron states. Such a feature of the Stark effect on QD states has strong implications on the optical properties and influences the electron-hole binding energy in the exciton through levels splitting via the Stark effect. For a quantum dot with the single non degenerate state the Stark effect will result only in an energy level shift. Any change in the overall electric field will shift the exciton levels of the dot for optical transitions either though band splitting (shifting) or decreasing the barrier of the confining potential. For different potential barrier heights discrete energy levels are also different. The Stark effect was studied in CdSe/ZnS core shell quantum dots embedded into quartz matrix under external electric field [151]. The authors documented a "blue" PL shift of 60 meV of the principal PL peak under external negative bias providing electric field 300 kV/m. This spectral shift is close to what was experimentally observed in our study. It is also interesting that the authors of Ref [151] also observed that the internal electric field actually decreases with increasing QD size [86]. In our experiment we observed the opposite effect as presented in Fig. 4.43, which can be explained by the enlarged surface area of the larger size quantum dots that allow more bio molecules to

come into contact resulting in a stronger total electric field imposed on the QD levels. The labeling factor for our experiments (the amount of biomolecules attached to a single QD) is close to 3 and can be increased in larger QDs as was illustrated in Fig 2.9.

4.3.   Summary

In conclusion to the first part of this research, we observed in this study that InAs/InGaAs QD structures suffer from an inhomogeneity of QD parameters. Scanning PL spectroscopy revealed two distinctive mechanisms for such an inhomogeneity. The first is a variation of the QD size across the wafer and the second is attributed to an uneven spatial distribution of nonradiative defects. Both cases can be carefully tailored by a selection of the QD structural parameters and growth regimes.

For the biomedical applications of quantum dots we have two major observations. First is the PL output increase of CdSe quantum dots called photo-stimulated enhancement. Both reversible and non-reversible PL enhancement are observed and documented. The kinetic curves and temperature dependences suggest that the enhancement effect is attributed to a light-induced increase of the potential barrier for electron–hole escape from the QD levels. This increase can be affected by the conjugation of the QDs with bio-molecules and can be used to improve the accuracy and sensitivity of the QD luminescence tags. So far, however, this has not been confirmed.

Second is that application of QD-probes significantly increased assay sensitivity, particularly for IL-10 concentration in normal plasma (not detectable with standard ELISA assays). Additional potential increase in the sensitivity is possible due to a

spectral shift that has been attributed to a change in electronic QD structure due to bioconjugation, changing or filtering the spectral range of signal collection only for conjugated quantum dots will further increase the signal to noise ratio. Conclusions from this research and further experiments are described and proposed in the next chapter.

5.   Conclusions and Recommendations

As the result of this PhD research project, the mechanisms behind the spatial inhomogeneity of InAs/InGaAs QD's have been established, a photo-enhancement phenomena was observed on CdSe QD's and a possible explanation provided, and finally the existence of a spectral shift in bioconjugated QD is discovered and statistically confirmed as a means to detect bioconjugation.

It was revealed that the optimal temperature range for InAs QD growth in In-GaAs/GaAs laser structures is 490 - 510°C. InAs/InGaAs QD structures suffer from an inhomogeneity of QD parameters. Scanning PL spectroscopy revealed two distinctive mechanisms for such an inhomogeneity. The first is a variation of the QD size across the wafer and the second is attributed to an uneven spatial distribution of nonradiative defects. Both cases can be carefully tailored by a selection of the QD structure parameters and growth regimes.

Capping layer composition studies show that there is optimal In content for these layers in InAs/InGaAs systems. For the capping layer of $In_xGa_{1-x}As$ it was shown that with a change of the parameter x from 0.10 to 0.25 the ground state PL peak maximum shifts from 1.010 to 1.054 eV. The reason for this PL peak position shift has been attributed to partial InAs QD decomposition at higher elastic stress conditions and to partial stress relaxation in QD structures with x > 0.15. The photoluminescence at 20 K

and scanning PL spectroscopy at 80 and 300 K of the ground and multiple excited states in InAs/InGaAs QDs have been investigated along with the influence of the excited state energy trends versus average ground state energy variations (or QD sizes) in the QD ensemble.

In the course of this study, the mechanism of optical instability in CdSe/Zns quantum dots and a model of a possible explanation was proposed. Photo-stimulated enhancement of the CdSe/ZnS quantum dot luminescence intensity was observed, classified and explained. Both reversible and non-reversible PL enhancements have been documented. The kinetic curves and temperature dependences suggest that the enhancement effect can be attributed to a light-induced increase of the potential barrier for electron–hole escape from the QD levels. This increase can be affected by the conjugation of the QDs with bio-molecules and can be used to improve the accuracy and sensitivity of QD luminescence tags.

Finally, it was discovered and statistically confirmed that bioconjugation can be spectroscopically identified by the existence of the spectral shift in a principal luminescence band. A blue shift was observed for different sizes of quantum dots and different types of biomolecules attached to them suggesting that this feature may be utilized as a bioconjugation marker, although the absolute value of the shift, in connection with bioconjugation, is not fully understood.

5.1. Recommendation for further research

Further experiments to confirm the proposed photo enhancement model are advised for other QD structures; i.e. with a different shell layer. Different relative barrier heights or other passivation conditions may provide additional information about the observed increase in PL intensity. It is also suggested to study other sizes of quantum dots for photo enhancement since weaker localized excitons in larger QD may not always be trapped by nearby traps giving additional insights into the validity of proposed model.

It is suggested that the further investigation of bioconjugation on the optical properties of quantum dots as fluorescent labels will take into account time resolved PL properties (intensity, maxima position). The influence of the surrounding environment on the sample should also be investigated, i.e. the influence of nitrogen/oxygen and even the pressure since part of the presented measurements were carried out in an evacuated cryostat showing some influence of pressure. The bioconjugation should be performed on a larger set of detector molecules in order to develop a full array of spectral features proving or disproving successful bioconjugation. The bioconjugation should also be checked for the usefulness of the created biomarker after successful quantum dot attachment that is detected via spectroscopic means; the presence of QD may hinder the biological activity of detecting biomolecule which may not be directly connected with the characteristic PL features but must be taken into account.

The results of this work were published in the following journals:

1. M. Dybiec, L. Borkovska, S. Ostapenko, T.V. Torchynska, J. L. Casas Espinola, A. Stintz, K. J. Malloy (2006). "Photoluminescence scanning on InAs/InGaAs quantum dot structures." Applied Surface Science.

2. M. Dybiec, S. Ostapenko, T. V. Torchynska and E. Velasquez Losada (2004). "Scanning photoluminescence spectroscopy in InAs/InGaAs quantum-dot structures." Applied Physics Letters 84(25): 5165-5167.

3. M. Dybiec, S. Ostapenko, T. V. Torchynska, E. Velásquez Losada, P. G. Eliseev, A. Stintz, and K. J. Malloy (2005). "Photoluminescence mapping on InAs/InGaAs quantum dot structures." Physica Status Solidi. (c) 2(8): 2951–2954.

4. N E Korsunska, M. Dybiec, L Zhukov, S Ostapenko and T Zhukov (2005). "Reversible and non-reversible photo-enchanced luminescence in CdSe/ZnS quantum dots." Semiconductor Science and Technology 20(8): 876-881.

5. T. V. Torchynska, M. Dybiec and S. Ostapenko (2005). "Ground and excited state energy trend in InAs/InGaAs quantum dots monitored by scanning photoluminescence spectroscopy." Pysical Review B 72: 195341.

References

1. Feynman, R.P., *There's Plenty of Room at the Bottom.* Engineering and Science, 1960.

2. Goodsell, D.S., *Bionanotechnology: lessons from nature*. 2004, New Jersey: Wiley-Liss, Inc.

3. Rocksby, H.P., *The Colour of Selenium Ruby Glasses.* J. Soc. Glass Tech., 1932. 16: p. 171.

4. Asryan, L.V. and R.A. Suris, *Theory and threshold characteristics of quantum dot lasers: Effect of Quantum Dot parameters dispersion.* International Journal of High Speed Electronics and Systems, 2002. 12(1): p. 111-176.

5. Arakawa, Y. and H. Sakaki, *Multidimensional quantum well laser and temperature dependence of its treshold current.* Applied Physics Letters, 1982. 40: p. 939-941.

6. Dingle, R. and C.H. Henry, *Quantum effects in heterostructure lasers*. 1976: U. S. Patent 3982207.

7. Gerion, D., F. Pinaud, S.C. Williams, W.J. Parak, D. Zanchet, S. Weiss, and A.P. Alivisatos, *Synthesis and Properties of Biocompatible Water-Soluble Silica-Coated CdSe/ZnS semiconductor quantum dots.* Journal of Physical Chemistry B, 2001. 105: p. 8861-8871.

8. Warren, C., W. Chan, and S. Nie, *Quantum dot bioconjugates for ultrasensitive nonisotopic detection.* Science, 1998. 281: p. 2016-2018.

9. Bruchez, M., M. Moronne, P. Gin, S. Weiss, and A.P. Alivisatos, *Semiconductor Nanocrystals as Fluorescent Biological Labels.* Science, 1998. 281: p. 2013-2016.

10. Leatherdale, C.A., W.K. Woo, F.V. Mikulec, and M.G. Bawendi, *On the Absorption Cross Section of CdSe Nanocrystal Quantum Dots.* J. Phys. Chem. B, 2002. 106: p. 7619-7622.

11. http://www.invitrogen.com.

12. Michalet, X., F.F. Pinaud, L.A. Bentolila, J.M. Tsay, S. Doose, J.J. Li, G. Sundaresan, A.M. Wu, S.S. Gambhir, and S. Weiss, *Quantum dots for live cells, in vivo imaging, and diagnostics.* Science, 2005. 307(5709): p. 538-544.

13. Dabbousi, B.O., J. Rodriquez-Viejo, F.V. Mikulec, J.R. Heine, H. Mattoussi, R. Ober, K.F. Jensen, and M.G. Bawendi, *(CdSe)ZnS Core-Shell Quantum Dots: Synthesis and Characterization of a Size Series of Higly Luminescent Nanocrystallites.* Journal of Physical Chemistry B, 1997(101): p. 9463-9475.

14. Kaul, Z., T. Yaguchi, S.C. Kaul, T. Hirano, R. Wadhwa, and K. Taira, *Mortalin imaging in normal and cancer cells with quantum dot immunoconjugates.* Cell research, 2003. 13(6): p. 503-507.

15. Santra, S., D. Dutta, G.A. Walter, and B.M. Moudgil, *Fluorescent Nanoparticle Probes for Cancer Imaging.* Technology in Cancer Research and Treatment, 2005. 4(6): p. 593-602.

16. Graybeal, J.D., *Molecular spectroscopy*. 1993: Mcgraw-Hill College.

17. Leon, R., S. Fafard, D. Leonard, J.L. Merz, and P.M. Petroff, *Visible luminescence from semiconductor quantum dots in large ensembles.* Applied Physics Letters, 1995. 67(4): p. 521-523.

18. Wu, Y.-h., K. Arai, and T. Yao, *Temperature dependence of the photoluminescence of ZnSe/ZnS quantum-dot structures.* Physical Review B, 1996. 53(16): p. R10485.

19. Jacak, L., P. Hawrylak, and A. Wojs, *Quantum Dots*, ed. Springer-Verlag. 1998.

20. Zhukov, A.E., A.Y. Egorov, A.R. Kovsh, V.M. Ustinov, N.N. Ledentsov, M.V. Maksimov, A.F. Tsatsul'nikov, S.V. Zaitsev, N.Y. Gordeev, P.S. Kop'ev, Z.I. Alferov, and D. Bimberg, *Injection heterolaser based on an array of vertically aligned InGaAs quantum dots in a AlGaAs matrix.* Semiconductors, 1996. 31(4): p. 411 - 414.

21. Lester, L.F., A. Stintz, H. Li, T.C. Newell, E.A. Pease, B.A. Fuchs, and K.J. Malloy, *Optical Characteristics of 1.24 μm InAs Quantum-Dot Laser Diodes.* IEEE Photonics Technology Letters, 1999. 11(8): p. 931-933.

22. Rossi, F., *Semiconductor macroatoms: basic physics and quantum-device applications*. 2005, London: Imperial College Press.

23. Green, M.A. *Recent developments and future prospects for third generation and other advanced cells*. in *WCPEC-4*. 2006. Hawaii.

24. Ekimov, A.I., A.L. Efros, and A.A. Onushchenko, *Quantum size effect in semiconductor microcrystals.* Sol. State Comm`, 1985. 56: p. 921-924.

25. Keldysh, L.V., Fiz. Tverd. Tela, 1962. 4: p. 2236.

26. Borovitskaya, E. and M.S. Shur, *Quantum Dots.* Selected topics in electronics and systems vol. 25. 2002.

27. Dyakonov, M. and M.S. Shur, *Consequences of Space Dependence of Effective Mass in Heterostuctures.* Journal of applied physics, 1998. 84: p. 3725-3730.

28. Borovitskaya, E. and M.S. Shur, *Consequences of space dependence of effective mass in quantum wires.* Solid State Electronics, 2000. 44: p. 1293-1296.

29. Borovitskaya, E. and M.S. Shur, *Consequences of space dependence of effective mass in quantum dots.* Solid State Electronics, 2000. 44: p. 1609-1612.

30. Williamson, A.J., *Energy states in quantum dots.* International Journal of High Speed Electronics and Systems, 2002. 12(1): p. 15-43.

31. Efros, A.L., M. Rosen, M. Kuno, M. Nirmal, D.J. Norris, and M. Bawendi, *Band-edge exciton in quantum dots of semiconductors with a degenerate valence band: Dark and bright exciton states.* Physical Review B, 1996. 54(7): p. 4843-4856.

32. Darnhofer, T. and U. Rossler, *Effects of band structure and spin in quantum dots.* Physical Review B, 1993. 47: p. 16020.

33. Wang, L.W., A.J. Williamson, A. Zunger, H. Jiang, and J. Singh, *Comparison of the k p and direct diagonalization approaches to the electronic structure of InAs/GaAs quantum dots.* Applied Physics Letters, 2000. 76(3): p. 339.

34. Buczko, R. and F. Bassani, *Bound and resonant electron states in quantum dots: The optical spectrum.* Physical Review B, 1996. 54(4): p. 2667.

35. Efros, A.L., *Luminescence polarization of CdSe microcrystals.* Physical Review B, 1992. 46(12): p. 7448-7458.

36. Grundmann, M., O. Stier, and D. Bimberg, *InAs/GaAs pyramidal quantum dots: strain distribution, optical phonons and electronic structure.* Physical Review B, 1995. 52: p. 11969-11981.

37. Prieto, J.E., E. Korutcheva, and I. Markov, eds. *Formation and Self-Assembly of coherent quantum dots: some thermodynamic aspects.* Quantum Dots: Research Developments, ed. P.A. Ling. Vol. 251. 2005, Nova Science: New York.

38.   Goldstein, L., F. Glas, J.Y. Marzin, M.N. Charasse, and G.L. Roux, *Growth by molecular beam epitaxy and characterization of InAs/GaAs strained-layer supperlattices.* Applied Physics Letters, 1985. 47(10): p. 1099-1101.

39.   Fafard, S., *Near-surface InAs/GaAs quantum dots with sharp electronic shells.* Applied Physics Letters, 2000. 76: p. 2707.

40.   Widmann, F., B. Daudin, G. Feuillet, Y. Samson, J.L. Rouvière, and N. Pelekanos, *Growth kinetics and optical properties of self-organized GaN quantum dots.* Journal of applied physics, 1998. 83(12): p. 7618-7624.

41.   Zundel, M.K., N.Y. Jin-Phillipp, F. Phillipp, K. Eberl, T. Riedl, E. Fehrenbacher, and A. Hangleiter, *Red-light-emitting injection laser based on InP/GaInP self-assembled quantum dots.* Applied Physics Letters, 1998. 73(13): p. 1784-1786.

42.   Zundel, M.K., P. Specht, K. Eberl, N.Y. Jin-Phillipp, and F. Phillipp, *Structural and optical properties of vertically aligned InP quantum dots.* Applied Physics Letters, 1997. 71(20): p. 2972-2974.

43.   Asaoka, K., Y. Ohno, S. Kishimoto, and T. Mitzutani, *Microscopic photoluminescence study of InAs single quantum dots grown on (100) GaAs.* Japanese Journal of Applied Physics, 1999. 38: p. 546-549.

44.   Bauer, E., *Phaenomenologische Theorie der Kristallabscheidung an Oberflaechen.I.* Zeitschrift für Kristallographie, 1958. 110: p. 372-394.

45.   Bauer, E., *Phaenomenologische Theorie der Kristallabscheidung an Oberflaechen. II.* Zeitschrift für Kristallographie, 1958. 110: p. 395-431.

46.   Stranski, I.N. and L.V. Krastanow, Akad. Wiss. Lit. Mainz Math. Natur. Kl. IIb, 1939. 146: p. 797.

47.   Turing, A.M., *The Chemical Basis of Morphogenesis.* Philosophical Transactions of the Royal Society of London. Series B, Biological Sciences, 1952. 237(641): p. 37-72.

48.   Temmyo, J., R. Notzel, and T. Tamamura, *Semiconductor nanostructures formed by the Turing instability.* Applied Physics Letters, 1997. 71(8): p. 1086.

49.   Daudin, B., F. Widmann, G. Feuillet, Y. Samson, M. Arlery, and J.L. Rouvière, *Stranski-Krastanov growth mode during the molecular beam epitaxy of highly strained GaN.* Physical Review B, 1997. 56(12): p. R7069.

50.   Rouvière, J.L., J. Simon, N. Pelekanos, B. Daudin, and G. Feuillet, *Preferential nucleation of GaN quantum dots at the edge of AlN threading dislocations.* Applied Physics Letters, 1999. 85(17): p. 2632-2634.

51. Dimitriev, V., K. Irvine, A. Zubrilov, D. Tsvetkov, V. Nikolaev, M. Jakobson, D. Nelson, and A. Sitnikova, *Gallium Nitride and Related Materials*. MRS, ed. R.D. Dupuis, et al. 1996, Pittsburgh, PA.

52. Tanaka, S., S. Iwai, and Y. Aoyagi, *Self-assembling GaN quantum dots on $Al_xGa_{1-x}N$ surfaces using a surfactant.* Applied Physics Letters, 1996. 69(26): p. 4096-4098.

53. Tanaka, S., H. Hirayama, S. Iwai, and Y. Aoyagi. in *MRS Symposium Proc.* 1997. (449), 135.

54. Ramvall, P., S. Tanaka, S. Nomura, P. Riblet, and Y. Aoyagi, *Confinement induced decrease of the exciton-longitudinal optical phonon coupling in GaN quantum dots.* Applied Physics Letters, 1999. 75(13): p. 1935-1937.

55. Goodwin, T.J., V.J. Leppert, and S.H. Risbud, *Synthesis of gallium nitride quantum dots through reactive laser ablation.* Applied Physics Letters, 1997. 70(23): p. 3122-3124.

56. Preschilla, A.N., S. Major, I. Samajdar, and R.S. Srinivasa, *Nanocrystalline gallium nitride thin films.* Applied Physics Letters, 2000. 77(12): p. 1861-1863.

57. Janik, J.F. and R.L. Wells, *Gallium Imide, $\{Ga(NH)_{3/2}\}_n$, a New Polymeric Precursor for Gallium Nitride Powders.* Chemistry of Materials, 1996. 8(12): p. 2708-2711.

58. Coffer, J.L., M.A. Johnson, L. Zhang, R.L. Wells, and J.F. Janik, *Influence of Precursor Route on the Photoluminescence of Bulk Nanocrystalline Gallium Nitride.* Chemistry of Materials, 1997. 9(12): p. 2671-2673.

59. Leonard, D., M. Krishnamurthy, C.M. Reaves, S.P. Denbaars, and P.M. Petroff, *Direct formation of quantum-sized dots from uniform coherent islands of InGaAs on GaAs surfaces.* Applied Physics Letters, 1993. 63(23): p. 3203-3205.

60. Altieri, P., M. Gurioli, S. Sanguinetti, E. Grilli, M. Guzzi, P. Frigeri, and S. Franchi, *Competition in the carrier capture between InGaAs/AlGaAs quantum dots and deep point defects.* Eur. Phys. J. B, 2002. 28: p. 157-161.

61. Tsatsul'nikov, A.F., A.Y. Egorov, P.S. Kop'ev, A.R. Kovsh, N.N. Ledentsov, M.V. Maximov, A.A. Suvorova, V.M. Ustinov, B.V. Volovik, A.E. Zhukov, M. Grundmann, D. Bimberg, and Z.I. Alferov, *Optical properties of InAlAs quantum dots in an AlGaAs matrix.* Applied Surface Science, 1998. 123/124: p. 381-384.

62. Carlsson, N., W. Seifert, A. Petersson, P. Castrillo, M.E. Pistol, and L. Samuelson, *Study of the two-dimensional–three-dimensional growth mode transition in metalorganic vapor phase epitaxy of GaInP/InP quantum-sized structures.* Applied Physics Letters, 1994. 65(24): p. 3093-3095.

63. Fafard, S., Z. Wasilewski, J. McCaffrey, S. Raymond, and S. Charbonneau, *InAs self-assembled quantum dots on InP by molecular beam epitaxy.* Applied Physics Letters, 1995. 68(7): p. 991-993.

64. Ustinov, V.M., E.R. Weber, S. Ruvimov, Z. Liliental-Weber, A.E. Zhukov, A.Y. Egorov, A.R. Kovsh, A.F. Tsatsul'nikov, and P.S. Kop'ev, *Effect of matrix on InAs self-organized quantum dots on InP substrate.* Applied Physics Letters, 1998. 72(2): p. 362-364.

65. Ponchet, A., A.L. Corre, H. L'Haridon, B. Lambert, and S. Salaun, *Relationship between self-organization and size of InAs islands on InP(001) grown by gas-source molecular beam epitaxy.* Applied Physics Letters, 1995. 67(13): p. 1850-1852.

66. Gong, Q., R. Nötzel, P.J.v. Veldhoven, T.J. Eijkemans, and J.H. Wolter, *Wavelength tuning of InAs quantum dots grown on InP (100) by chemical-beam epitaxy.* Applied Physics Letters, 2003. 84(2): p. 275-277.

67. Junno, B., T. Junno, M.S. Miller, and L. Samuelson, *A reflection high-energy electron diffraction and atomic force microscopy study of the chemical beam epitaxial growth of InAs and InP islands on (001) GaP.* Applied Physics Letters, 1998. 72(8): p. 954-956.

68. Leon, R., C. Lobo, T.P. Chin, J.M. Woodall, S. Fafard, S. Ruvimov, Z. Liliental-Weber, and M.A.S. Kalceff, *Self-forming InAs/GaP quantum dots by direct island growth.* Applied Physics Letters, 1998. 72(11): p. 1356-1358.

69. Bimberg, D., M. Grundmann, and N.N. Ledentsov, *Quantum Dot Heterostructures.* 1998, New York: Wiley.

70. Sugawara, M., H. Ebe, N. Hatori, M. Ishida, Y. Arakawa, T. Akiyama, K. Otsubo, and Y. Nakata, *Theory of optical signal amplification and processing by quantum-dot semiconductor optical amplifiers.* Physical Review B, 2004. 69: p. 235332.

71. Korsunskaya, N.E., I.V. Markevich, and M.K. Sheinkman, *Photochemical Reactions at Low Temperatures in CdS Single Crystals.* Physica Status Solidi, 1966. 13(25): p. 25-36.

72. Bergstresser, T.K. and M.L. Cohen, *Electronic structure and optical properties of hexagonal CdSe, CdS and ZnS.* Physical Review, 1967. 164(3): p. 164.

73.   Murray, C.B., D.J. Norris, and M.G. Bawendi, *Synthesis and characterization of nearly monodisperse CdE (E = S, Se, Te) Semiconductor Nanocrystallites.* Journal of the American Chemical Society, 1993. 115: p. 8706-8715.

74.   Woggon, U., W. Petri, A. Dinger, S. Petillon, M. Hetterich, M. Grün, K.P. O'Donnell, H. Kalt, and C. Klingshirn, *Electronic states and optical gain in strained CdS/ZnS quantum structures.* Physical Review B, 1997. 55(3): p. 1364.

75.   Karczewski, G., S. Mackowski, M. Kutrowski, T. Wojtowicz, and J. Kossut, *Photoluminescence study of CdTe/ZnTe self-assembled quantum dots.* Applied Physics Letters, 1999. 74(20): p. 3011.

76.   Daruka, I.n. and A.-L.s. Baraba, *Equilibrium phase diagrams for dislocation free self-assembled quantum dots.* Applied Physics Letters, 1998. 72(17): p. 2102-2104.

77.   Hines, M.A. and P. Guyot-Sionnest, *Bright UV-Blue Luminescent Colloidal ZnSe Nanocrystals.* Physical Chemistry B, 1998. 102(19): p. 3655.

78.   Nikesh, V.V. and S. Mahamuni, *Highly photoluminescent ZnSe/ZnS quantum dots.* Semiconductor Science and Technology, 2001. 16: p. 687–690.

79.   Trindade, T., P. O'Brien, and X.-m. Zhang, *Synthesis of CdS and CdSe Nanocrystallites Using a Novel Single-Molecule Precursors Approach.* Chemistry of Materials, 1997. 9(2): p. 523-530.

80.   Santra, S., H. Yang, P.H. Holloway, J.T. Stanley, and R.A. Mericle, *Synthesis of Water-Dispersible Fluorescent, Radio-Opaque, and Paramagnetic CdS:Mn/ZnS Quantum Dots: A Multifunctional Probe for Bioimaging.* Journal of American Chemical Society, 2004. 127(6): p. 1656-1657.

81.   Radi, P.A., A.G. Brito-Madurro, J.M. Madurro, and N.O. Dantas, *Characterization and Properties of CdO Nanocrystals Incorporated in Polyacrylamide.* Brazilian Journal of Physics, 2006. 36(2a): p. 412-414.

82.   Banin, U., M. Bruchez, A.P. Alivisatos, T. Ha, S. Weiss, and D.S. Chemla, *Evidence for a thermal contribution to emission intermittency in single CdSe/CdS core/shell nanocrystals.* Journal of chemical physics, 1999. 110(2): p. 1195-1201.

83.   Shimizu, K.T., R.G. Neuhauser, C.A. Leatherdale, S.A. Empedocles, W.K. Woo, and M.G. Bawendi, *Blinking statistics in single semiconductor nanocrystal quantum dots.* Physical Review B, 2001. 63(20): p. 205316.

84.   Dantas, N.O., A.F.G. Monte, W.A. Cardoso, A.G. Brito-Madurro, J.M. Madurro, and P.C. Morais, *Growth and characterisation of ZnO quantum dots in polyacrylamide.* Microelectronics journal, 2005. 36(3-6): p. 234-236.

85. Dong, W. and C. Zhu, *Optical properties of surface-modified CdO nanoparticles.* Optical Materials, 2003. 22(3): p. 227-233.

86. Norris, D.J., A.L. Efros, M. Rosen, and M.G. Bawendi, *Size dependence of exciton fine structures in CdSe quantum dots.* Physical Review B, 1996. 53(24): p. 16347-16354.

87. Rodriguez-Viejo, J., H. Mattoussi, J.R. Heine, M.K. Kuno, J. Michel, M.G. Bawendi, and K.F. Jensen, *Evidence of photo- and electrodarkening of (CdSe)ZnS quantum dot composites.* Journal of applied physics, 2000. 87(12): p. 8526-8534.

88. Kershaw, S., M. Burt, M. Harrison, A. Rogach, H. Weller, and A. Eychmüller, *Colloidal CdTe/HgTe quantum dots with high photoluminescence quantum efficiency at room temperature.* Applied Physics Letters, 1999. 75(12): p. 1694-1696.

89. Jun, Y.-w., C.-S. Choi, and J. Cheon, *Size and shape controlled ZnTe nanocrystals with quantum confinement effect.* Chemical Communication, 2001. 1: p. 101-102.

90. Mews, A., A.V. Kadavanich, U. Banin, and A.P. Alivisatos, *Structural and spectroscopic investigations of CdS/HgS/CdS quantum-dot quantum wells.* Physical Review B, 1996. 53(20): p. R13242.

91. Kobayashi, M., S. Nakamura, K. Kitamura, H. Umeya, A. Jia, A. Yoshikawa, M. Shimotomai, and Y. Kato, *Luminescence properties of CdS quantum dots on ZnSe.* Journal of Vacuum Science and Technology B, 1999. 17(5): p. 2005-2008.

92. Manna, L., D.J. Milliron, A. Meisel, E.C. Scher, and P. Alivisatos, *Controlled growth of tetrapod-branched inorganic nanocrystals.* Nature Materials, 2003. 2: p. 382-385.

93. Han, M., X. Gao, J.Z. Su, and S. Nie, *Quantum-dot-tagged microbeads for multiplexed optical coding of biomolecules.* Nature Biotechnology, 2001. 19: p. 631.

94. Dubertret, B., P. Skourides, D.J. Norris, V. Noireaux, A.H. Brivanlou, and A. Libchaber, *In Vivo Imaging of Quantum Dots Encapsulated in Phospholipid Micelles.* Science, 2002. 298: p. 1759.

95. Walker, G.W., V.C. Sundar, C.M. Rudzinski, A.W. Wun, M.G. Bawendi, and D.G. Nocera, *Quantum-dot optical temperature probes.* Applied Physics Letters, 2003. 83(17): p. 3555-3557.

96.   Downing, G.J., *Biomarkers and surrogate endpoints: preferred definitions and conceptual framework.* Clinical Pharmacology & Therapeutics, 2001. 69: p. 89-95.

97.   Jaiswal, J.K. and S.M. Simon, *Potentials and pitfalls of fluorescent quantum dots for biological imaging.* Trends in Cell Biology, 2004. 14(9): p. 497-504.

98.   Gorelik, E., D.P. Landsittel, A.M. Marrangoni, F. Modugno, L. Velikokhatnaya, M.T. Winans, W.L. Bigbee, R.B. Herberman, and A.E. Lokshin, *Multiplexed Immunobead-Based Cytokine Profiling for Early Detection of Ovarian Cancer.* Cancer Epidemiology, Biomarkers & Prevention, 2005. 14(4): p. 981.

99.   Moore, K.W., W. Malefyt, R. Coffman, and A. O'Garra, *Interleukin-10 and the interleukin-10 receptor.* Annu. Rev. Immunol., 2001. 19: p. 683.

100.   Fiorentino, D., M. Bond, and T. Mosmann, *Two types of mouse T helper cell. IV. Th2 clones secrete a factor that inhibits cytokine production by Th1 clones.* J. Exp. Med., 1989. 170: p. 2081.

101.   Neubig, R., M. Spedding, T. Kenakin, and A. Christopoulos, *International Union of Pharmacology Committee on Receptor Nomenclature and Drug Classification. XXXVIII. Update on Terms and Symbols in Quantitative Pharmacology.* Pharmacological Reviews, 2003. 55(4): p. 597.

102.   Pauler, D.K., U. Menon, M. McIntosh, H.L. Symecko, S.J. Skates, and I.J. Jacobs, *Factors Influencing Serum CA125II Levels in Healthy Postmenopausal Women.* Cancer Epidemiology, Biomarkers & Prevention, 2001. 10(5): p. 489-493.

103.   Bast, R.C., D. Badgwell, Z. Lu, R. Marquez, D. Rosen, J. Liu, K.A. Baggerly, E.N. Atkinson, S. Skates, Z. Zhang, A. Lokshin, U. Menon, I. Jacobs, and K. Lu, *New tumor markers: CA125 and beyond.* International Journal of Gynecological Cancer, 2005. 15(s3): p. 274-281.

104.   Fures, R., D. Bukovic, B. Hodek, B. Klaric, R. Herman, and G. Grubisic, *Preoperative tumor marker CA125 levels in relation to epithelial ovarian cancer stage.* Coll. Anthropol, 1999. 1: p. 189-194.

105.   *http://en.wikipedia.org/wiki/Serine_protease.*

106.   Ries L, Eisner M, and Kosary C, SEER Cancer Statistics Review, 2004: p. 1975-2001.

107.   *http://www.hpr.se/antibody_info.php?antibody_id=829.* The Human Protein Atlas.

108. *National Cancer Institute online resources*. 2004; Available from: http://www.cancer.gov/cancertopics/factsheet/Detection/PSA.

109. Gravallese, E.M., *Osteopontin: a bridge between bone and the immune system.* J. Clin. Invest, 2003. 112: p. 147-149.

110. Rittling, S.R. and D.T. Denhardt, *Osteopontin Function in Pathology: Lessons from Osteopontin-Deficient Mice.* Experimental Nephrology, 1999. 7(2): p. 103-113.

111. Bailey, R.E. and S. Nie, *Alloyed Semiconductor Quantum Dots: Tuning the Optical Properties without Changing the Particle Size.* Journal of the American Chemical Society, 2003. 125(23): p. 7100-7106.

112. Torchynska, T.V., J.L.C. Espinola, P.G. Eliseev, A. Stintz, K.J. Malloy, and R.P. Sierra, *Localized excitons in InAs self-assembled quantum dots embedded in InGaAs/GaAs multi-quantum wells.* Physica Status Solidi A, 2003. 195(1): p. 209-213.

113. Torchynska, T.V., J.L.C. Espinola, E.V. Losada, P.G. Eliseev, A. Stintz, K.J. Malloy, and R.P. Sierra, *Thermal ionisation of ground and multiply excited states in InAs quantum dots embedded into InGaAs/GaAs MQW.* Surface science, 2003. 532-535: p. 848-851.

114. *http://probes.invitrogen.com/media/pis/mp19010.pdf*.

115. Crowther, J.R., *The ELISA guidebook*. Methods in Molecular Biology. Vol. 149. 1984, Totowa: Humana Press Inc.

116. *http://www.chemicon.com*.

117. Schena, M., *Protein Microarrays*. 2005, Sudbury: Jones and Bartlett Publisers.

118. Liotta LA, Espina V, Mehta AI, Calvert V, Rosenblatt K, and Geho D, *Protein microarrays: meeting analytical challenges for clinical applications.* Cancer Cell, 2003. 3(4): p. 317-25.

119. Kusnezow W, Jacob A, Walijew A, Diehl F, and Hoheisel JD, *Antibody microarrays: an evaluation of production parameters.* Proteomics, 2003. 3(3): p. 254-64.

120. G. Park, O. B. Shchekin, D. L. Huffaker, and D.G. Deppe, *Lasing from InGaAs/GaAs quantum dots with extended wavelength and well-defined harmonic-oscillator energy levels.* Applied Physics Letters, 1998. 73(23): p. 3351-3353.

121. Eliseev, P.G., D.P. Popescu, T.V. Torchynska, A. Stintz, and K.J. Malloy. *Shell model of semiconductor quantum dots*. in *SPIE*. 2004. San Jose. (5349), 46-53.

122. Asryan, L.V. and R.A. Suris, *Inhomogeneous line broadening and the threshold current density of a semiconductor quantum dot laser.* Semiconductor Science and Technology, 1996. 11: p. 554-567.

123. Pryor, C., *Eight-band calculations of strained InAs/GaAs quantum dots compared with one-, four-, and six-band approximations.* Physical Review B, 1998. 57(12): p. 7190.

124. Ustinov, V.M., N.A. Maleev, A.E. Zhukov, A.R. Kovsh, A.Y. Egorov, A.V. Lunev, B.V. Volovik, I.L. Krestnikov, Y.G. Musikhin, N.A. Bert, P.S. Kop'ev, and Z.I. Alferov, *InAs/InGaAs quantum dot structures on GaAs substrates emitting at 1.3 μm.* Applied Physics Letters, 1999. 74(19): p. 2815-2817.

125. Grundmann, M., *Nano-Optoelectronics*. 2002: Springer; 1 edition (August 15, 2002).

126. Herman, M.A. and H. Sitter, *Molecular Beam Epitaxy: Fundamentals and Current Status*. Springer Series in Materials Science. Vol. 7. 1996: Springer-Verlag; 2nd edition (August 1996).

127. Dybiec, M., S. Ostapenko, T.V. Torchynska, E.V. Lozada, P.G. Eliseev, A. Stintz, and K.J. Malloy, *Photoluminescence mapping on InAs/InGaAs quantum dot structures.* Physica Status Solidi (c), 2005. 2(8): p. 2951-2954.

128. Stintz, A., G.T. Liu, A.L. Gray, R. Spillers, S.M. Delgado, and K.J. Malloy, *Characterization of InAs quantum dots in strained $In_xGa_{1-x}As$ quantum wells.* Journal of Vacuum Science and Technology B, 2000. 18: p. 1496-1501.

129. Garyagdyev A, Ya Gorodetskii I, Korsunskaya N E, Markevich I V, Nuryagdyev O, and Sheinkman M K, Sov. Phys. Semicond., 1987. 21: p. 249.

130. Oda, M., M.Y. Shen, M. Saito, and T. Goto, *Photobrightening of CuBr nanocrystals in PMMA.* Journal of Luminescence, 2000. 87-89: p. 469-471.

131. Masumoto, Y., K. Kawabata, and T. Kawazoe, *Quantum size effect and persistent hole burning of CuI nanocrystals.* Physical Review B, 1995. 52(11): p. 7834–7837.

132. Varshni, Y.P., *Temperature dependence of the energy gap in semiconductors.* Physica, 1967. 34(1): p. 149-154.

133. Bube, R.H., *Photoconductivity of Solids*. 1978: Krieger Publishing Company (January 1978).

134. Sheinkman, M.K., N.E. Korsunskaya, L.V. Markevich, and T.V. Torchynskaya, *The Recharge-enhanced transformations of donor-acceptor pairs and clusters in CdS.* Journal of Physics and Chemistry of Solids, 1982. 43(5): p. 475-479.

135. Korsunskaya, N.E., I.V. Markevich, and E.P. Shulga, *The influence of carrier trapping on defect reaction activation energy in semiconductors (pseudo-effect of recombination enhanced diffusion).* Journal of Physics and Chemistry of Solids, 1992. 53(3): p. 469-474.

136. Leatherdale, C.A., C.R. Kagan, N.Y. Morgan, S.A. Empedocles, M.A. Kastner, and M.G. Bawendi, *Photoconductivity in CdSe quantum dot solids.* Physical Review B, 2000. 62(4): p. 2669.

137. Chepic, D.I., A.L. Efros, A.I. Ekimov, M.G. Ivanov, V.A. Kharchenko, I.A. Kudriavtsev, and T.V. Yazeva, *Auger ionization of semiconductor quantum drops in a glass matrix.* Journal of Luminescence, 1990. 47(3): p. 113-127.

138. Korsunskaya, N.E., I.V. Markevich, T.V. Torchynskaya, and M.K. Sheinkman, *Photosensitivity degradation mechanism in CdS:Cu single crystals.* Physica Status Solidi A, 1980. 60(2): p. 565-572.

139. *http://www.dakousa.com/*.

140. *http://vwrlabshop.com*. MicroWell* 96-Well Plates, Sterile, NUNC, Flat bottom, VWR catalog #62409-120.

141. *http://www.serotec.com/asp/index.html*.

142. *http://www.whatman.com/*.

143. *www.arrayit.com*.

144. *http://www.sigmaaldrich.com/Local/SA_Splash.html*.

145. *http://www.nikonconfocal.com/*.

146. Qin, L., L. Rueda, A. Ali, and A. Ngom, *Spot detection and image segmentation in DNA microarray data.* Appl Bioinformatics, 2005. 4(1): p. 1-11.

147. Wang, X.H., R.S. Istepanian, and Y.H. Song, *Application of wavelet modulus maxima in microarray spots recognition.* IEEE Trans Nanobioscience, 2003. 2(4): p. 190-2.

148. Smith, A.M., S. Dave, S. Nie, L. True, and X. Gao, *Multicolor quantum dots for molecular diagnostics of cancer.* Expert Review of Molecular Diagnostics, 2006. 6(2): p. 231-244.

149. Klimov, V.I., *Optical Nonlinearities and Ultrafast Carrier Dynamics in Semiconductor Nanocrystals.* Journal of Physical Chemistry B, 200. 104(26): p. 6112-6123.

150. Jankovic, A., R. Ferreira, and G. Bastard, *Non-perturbative optical response of a "fluctuating" single quantum dot.* Physica E, 2004. 21(2-4): p. 252-256.

151. Empedocles, S.A. and M.G. Bawendi, *Quantum-Confined Stark Effect in Single CdSe Nanocrystallite Quantum Dots.* Science, 1997. 278.

Bibliography

M. A. Herman, H. Sitter, *Molecular Beam Epitaxy: Fundamentals and Current Status* (Springer Series in Materials Science, Vol. 7), (1996) Springer-Verlag; 2nd edition (August 1996), ISBN: 0387605940.

Marius Grundmann, *Nano-Optoelectronics*, (2002) Springer; 1 edition (August 15, 2002), ISBN: 3540433945.

E. Borovitskaya, Michael Shur, *Quantum Dots (Selected Topics in Electronics and Systems, Vol. 25)*, World Scientific Publishing Company; 1st edition (June 15, 2002), ISBN: 9810249187.

Lucjan Jacak, Pawel Hawrylak, Arkadius Wojs, *Quantum Dots*, Springer (March 1998), ISBN: 3540636536.

Ling, Peter A, *Quantum dots: research developments*, Horizons in world physics; v. 251, New York Nova Science Publishers (2005), ISBN 1594544069.

Fausto Rossi, *Semiconductor Macroatoms: Basic Physics And Quantum-device Applications*, Imperial College Press (December 1, 2005), ISBN: 1860946089.

Eoin O'Reilly, *Quantum theory of solids*, (2002), Taylor & Francis Group, ISBN: 074840628X.

David S. Goodsell, *Bio-nanotechnology Lessons from Nature* (2004) Wiley-Liss, ISBN: 047141719X.

Dieter Bimberg, Marius Grundman, Nikolai N. Ledentsov, *Quantum Dot Heterostructures*, John Wiley & Sons, (March 19, 1999), ISBN: 0471973882.

Richard H. Bube, *Photoconductivity of Solids*, Krieger Publishing Company (January 1978), ISBN: 0471114847.

John R. Crowther, *ELISA guide book*, Totowa, NJ: Humana Press, (2001), ISBN: 0896037282.

Vladimir V. Mitin, Viatcheslav A. Kochelap, Michael A. Stroscio, *Quantum Heterostructures*, Cambridge University Press (1999), ISBN 0 521 63177 7.

About the Author

Maciej Dybiec received his bachelor degree in Mechatronics at International Faculty of Engineering of Technical University of Lodz (Poland). His bachelor diploma work was dedicated to investigation of diamond coatings for biomedical applications.

In January 2000, Maciej joined the Master's program in Biomedical Enginneering department of Technical University of Lodz doing most of his thesis research on the scholarship at Forschungszentrum Für Mikrostrukturtechnik at University of Wuppertal (Germany). He successfully defended his thesis "Plasma electron density measurements by the microwave resonance cavity technique" in September 2002.

In January of 2003 he joined research group of Prof. Sergei Ostapenko at University of South Florida to study the photoluminescence properties of quantum dots as a Ph.D. candidate. His Ph.D. work was accomplished in September 2006 and in October 2006 Maciej defended his dissertation.

Now he works for Semiconductor Diagnostics, Inc. in the research and development department located in Tampa, FL.